Paleoclimate Model-Data Comparisons of Hydroclimate over North America with a Focus on Megadroughts

Sloan Coats

Submitted in partial fulfillment of the

requirements for the degree of

Doctor of Philosophy

in the Graduate School of Arts and Sciences

COLUMBIA UNIVERSITY

2015

Abstract

Paleoclimate Model-Data Comparisons of Hydroclimate over North America with a Focus on Megadroughts

Sloan Coats

For the first time in the history of the Intergovernmental Panel on Climate Change, the Paleoclimate and Coupled Model Intercomparison Projects Phases 3 and 5 produced an ensemble of forced transient simulations of the last millennium. This wealth of model output, when combined with a growing collection of high spatial and temporal resolution paleoclimate estimates of past climate variability, represents an important and unprecedented source of information on climate variability over decades to centuries. This dissertation thus combines paleoclimate evidence with climate modeling to define a physical and statistical paradigm through which to analyze these combined sources of information and subsequently to characterize the features of the North American climate system that cannot be sufficiently understood using instrumental data alone. This includes features that have long timescales of variability or that are rare, and by consequence have few degrees of freedom over the short instrumental interval (1850 C.E. to Present), as well as interannual dynamical relationships that, while potentially well characterized by observations, are non-stationary. An integrative approach to analyzing these features or relationships serves two fundamental purposes: 1) It provides a more comprehensive characterization of past climate variability, albeit with the caveat of model bias, to clarify understanding of the dynamics that produce these features or relationships in the real world; and 2) it assesses whether coupled general circulation models (CGCMs) are able to simulate these features or relationships, which is necessary to

determine that state-of-the-art CGCMs can accurately constrain the risk of future climate change. The focus herein will be on multidecadal hydroclimate change, or megadroughts, in the paleoclimate record of the American Southwest to better inform our understanding of the risk of future hydroclimate change over the region. Two fundamental understandings are derived from this work. Firstly, CGCMs are successful at simulating discrete periods of multidecadal hydroclimate change that are characteristic in length, magnitude, and frequency of occurrence of megadroughts in the paleoclimate record. The simulated megadroughts are not tied in any coherent way to exogenous forcing, however, suggesting that CGCMs simulate large-magnitude internal variability on multidecadal timescales. Secondly, the dynamical characteristics of CGCMs are important in determining the atmosphere-ocean variability that drives multidecadal hydroclimate change. The dynamical characteristics of relevance include teleconnection realism and stationarity, the magnitude of ocean variability, and the relative magnitudes of different modes of atmosphere-ocean and purely atmospheric variability. Additionally, a new understanding of real-world megadrought dynamics is derived herein, with the characteristics of some CGGMs providing a better representation of these dynamics.

Contents

List of Figures

Acknowledgements

This work would not have been possible without a large group of generous and dedicated individuals. These include advisors like Jason Smerdon, Richard Seager and Ben Cook as well as coauthors like Fidel González-Ruoco, Dan Griffin, Kevin Anchukaitis and Ed Cook. Ed deserves particular thanks for producing the reconstructions that are the basis of this work and for being so generous with that data. Additionally, none of this would have been possible without computational support, including the downloading and processing of the CMIP5 data, from Haibo Liu and Naomi Henderson.

Jason, Richard and Ben were fantastic advisors. They put a huge amount of effort into this work and I am truly grateful for them being so generous with their time. Jason, in particular, graduate school was a grind and on both a scientific and personal level I would not have made it through this experience without his help. He will have many (very lucky) students in the future and I look forward to seeing what they accomplish. I have such a wonderful, loving and caring family and extended family and friends back home. Mom, Dad, Carrie, Hilary, Harry, Karen, Jake, Daanika, Teo, Jesse, Heather, Lee and Halie—thank you for all of your support. My parents in particular are the two most caring people in the world and I am incredibly lucky to be their son. Julius, I have never had such a dedicated and generous friend and I would not have made it through graduate school without his help. And Helen, who is far too nice to me, deserves many thanks for her unequivocal love and support.

Dedication

Ty, there is no doubt that you would have done something incredible over the last four years. A dissertation, maybe, but probably something more interesting and important. In any case, I would love to have shared this dissertation with you. Though I miss you, you are and will continue to be an inspiration.

Grandpa Doc, as I child I viewed you as a hero (and I still do!) and science as heroic. I would never have gone down this path without your influence and I am so glad that I did.

Chapter 1

Introduction

1.1 What are paleoclimate model-data comparisons and what is their value over the Common Era?

A fundamental limitation of our understanding of the climate system is the short length of the instrumental interval — the period for which there are direct observations of the land, atmosphere and ocean. Records of hydroclimate, in particular, tend to be spatially sparse, temporally incomplete and short. To demonstrate this, Figure 1.1 shows the number of rain gauge stations, the predominant method by which hydroclimate conditions are observed, in both temperate and tropical locations as a function of time. In 1850 there were essentially no direct observations of precipitation anywhere on the globe. More complex — and likely more scientifically interesting and useful — hydroclimate variables like soil moisture have even shorter and more incomplete observational records. Together this means that the observed record of hydroclimate is at most 150 years in length.

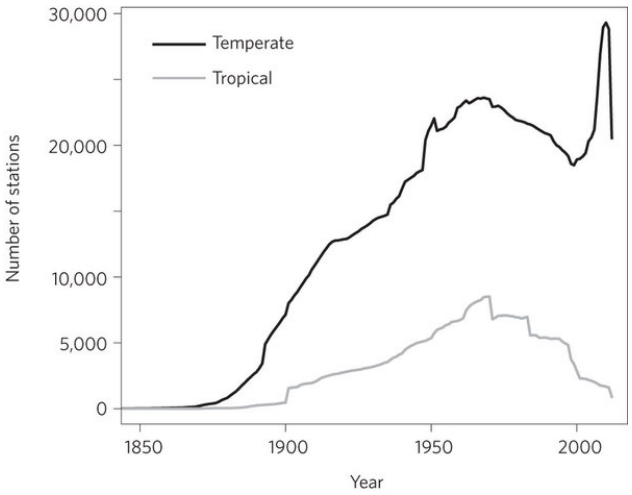

Figure 1.1: Number of rain gauge stations in temperate and tropical locations. Tropical stations are between the Equator and 25° latitude, and temperate stations are between 25° and 60° latitude in both the Northern and the Southern Hemispheres. The two lines in the plot are separate data sets, rather than cumulative numbers. Taken from Wohl et al. (2012).

150 years is too short to constrain many aspects of the climate system that are important both societally and scientifically. For instance, decadal-to-multidecadal timescale modes of atmosphere-ocean variability such as the Pacific Decadal Oscillation (PDO — Mantua & Hare, 2002) and the Atlantic Multidecadal Oscillation (AMO — Enfield et al., 2001) have global temperature and hydroclimate impacts. In some regions the magnitude of these impacts can rival those of interannual (and therefore perhaps better understood) modes of variability like the El Niño-Southern Oscillation (ENSO); see for instance Kushnir et al. (2010) for the impact of the AMO on North American (NA) hydroclimate. The instrumental interval, however, is too short to effectively characterize the PDO and AMO. In particular, the AMO is estimated to have a dominant periodicity of approximately 65 years (Schlesinger & Ramankutty, 1994). The 150-year instrumental interval would thus provide only two degrees of freedom by which to characterize the AMO and its impacts.

The paleoclimate record of the Common Era (C.E.) is an important target for extending the record of climate variability beyond the instrumental interval. Critically, the paleoclimate record of the C.E. has similar temporal and spatial resolution to climate observations. It can thus provide longer records of important aspects of the climate system like the AMO. Nevertheless, the paleoclimate record is inherently more uncertain than observa-

tions, as corals, tree rings, speleothems and other proxies provide only indirect measurements of the climate system. Most importantly, however, the C.E. paleoclimate record does not provide a comprehensive view of the atmosphere and ocean. It thus is of limited use in understanding climate dynamics, for instance not just defining the past state of the AMO but understanding the origin of that variability.

Over the last ten years, advances in computation have allowed for the simulation of climate on timescales longer than the instrumental interval. These Coupled General Circulation Model (CGCM) simulations can provide another constraint on our understanding of the climate system. Unlike the C.E. paleoclimate record, CGCMs provide a comprehensive view of the atmosphere and ocean and can thus be used to derive a fundamental understanding of climate dynamics. This view is compromised, however, by the fact that CGCMs are an imperfect representation of the actual climate system. This leads to biases that at best must be accounted for when analyzing CGCM output and at worst can severely compromise the ability of CGCMs to provide insight into certain climatic processes.

Paleoclimate model-data comparisons seek to partially overcome the limitations of these individual data sources by performing combined analyses of the C.E. paleoclimate record, instrumental data and long climate integrations from CGCMs. They have become an important tool for studying climate features that have long timescales of variability or that are rare, and by consequence have few degrees of freedom over the short instrumental interval, as well as interannual dynamical relationships that, while potentially well characterized by observations, are non-stationary. Specific studies include assessments of the impact of volcanic eruptions on surface temperature (Anchukaitis et al., 2012) and the temperature sensitivity to natural forcing over the last millennium (Fernández-Donado et al., 2013), as well as the use of paleoclimate data to distinguish among disparate future climate projections (Schmidt et al., 2013). To date, however, paleoclimate-model data comparisons have rarely been used in studies of hydroclimate, particularly on the regional spatial scales that tend to be socio-economically important. The purpose of this thesis, therefore, is to

develop paleoclimate model-data comparison frameworks to better constrain the dynamics of hydroclimate change over the American Southwest (roughly from the northern border of California to the southern border of the United States, and from the high plains to the Pacific coast; hereinafter ASW).

1.2 Why study hydroclimate over the ASW?

Before outlining the specific understandings that we will target with paleoclimate model-data comparisons of hydroclimate over the ASW, it is important to motivate the need to study hydroclimate change in this region. The ASW accounts for more than 20% of the United States population — a proportion that is growing — and greater than half of domestic food crop production. The ASW grows this food despite a fickle and unpredictable water supply that relies heavily on large-scale irrigation infrastructure that is static in space and time (Tanaka et al., 2006). Historically, water management systems in the ASW have been designed under the assumption that natural systems fluctuate within an unchanging envelope of variability (stationarity — Milly et al., 2008) and any responses to hydroclimate change have been dominated by reactive technical solutions (Pahl-Wostl et al., 2007). It has become clear, however, that anthropogenic and natural climate change can fundamentally alter the hydrologic cycle, both the baseline and the extremes. Consequently, increasing the adaptability, flexibility, and resiliency of resource management systems in the ASW is imperative. Such efforts will necessarily include changes to both the demand and supply side of water management. Changes to the latter, which will be dictated by the ASW's aging water supply systems even with full adoption and implementation of adaptable management practices, will require knowledge of the spatial and temporal characteristics of future hydroclimate five to fifty years in advance.

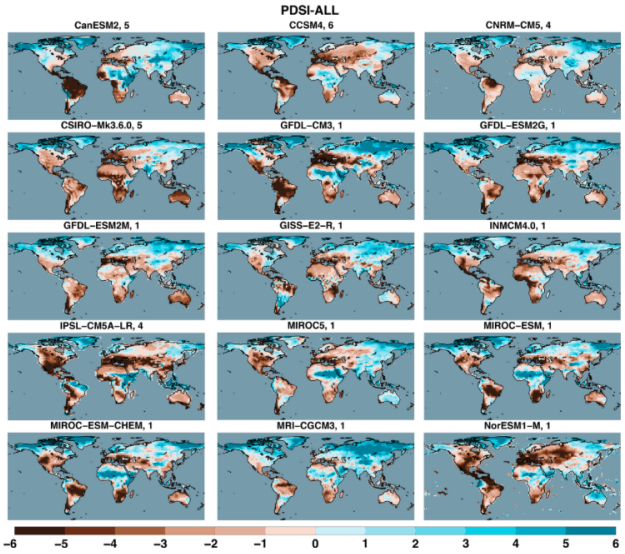

Figure 1.2: Global Palmer Drought Severity Index (PDSI — Palmer, 1965), a common metric of hydroclimate variability that is thoroughly outlined in the Methods section, averaged from 2080–2099 for the RCP8.5 future emissions scenario. PDSI values approximately represent the standardized departure from mean hydroclimate conditions during the instrumental interval, with negative PDSI indicating dry conditions. The models and number of ensemble members is listed in each panel title; for models with multiple ensemble members, the maps represent the ensemble average. Taken from Cook et al. (2014a).

Such information can best be provided by CGCM simulations. Figure 1.2 shows global hydroclimate projections for the end of the current century from the CMIP5 multi-model ensemble (Cook et al., 2014a), which can be interpreted as the change relative to a 20th century baseline. These projections use the RCP8.5 future emissions scenario and while this represents the worst case for future emissions, it is consistent with the current lack of international action to limit greenhouse gas emissions (e.g. Seager et al., 2013). In each case the plotted variable is the Palmer Drought Severity Index (PDSI — Palmer, 1965), an offline model of soil moisture balance that is a standard metric of hydroclimate conditions. The CGCMs consistently indicate that the ASW will dry over the coming century. Nevertheless, there are intermodel differences in the hydroclimate projections for this region, particularly with regard to the severity of drying. The ISPL and MIROC models, for instance, simulate much more severe drying than the MRI and GFDL models.

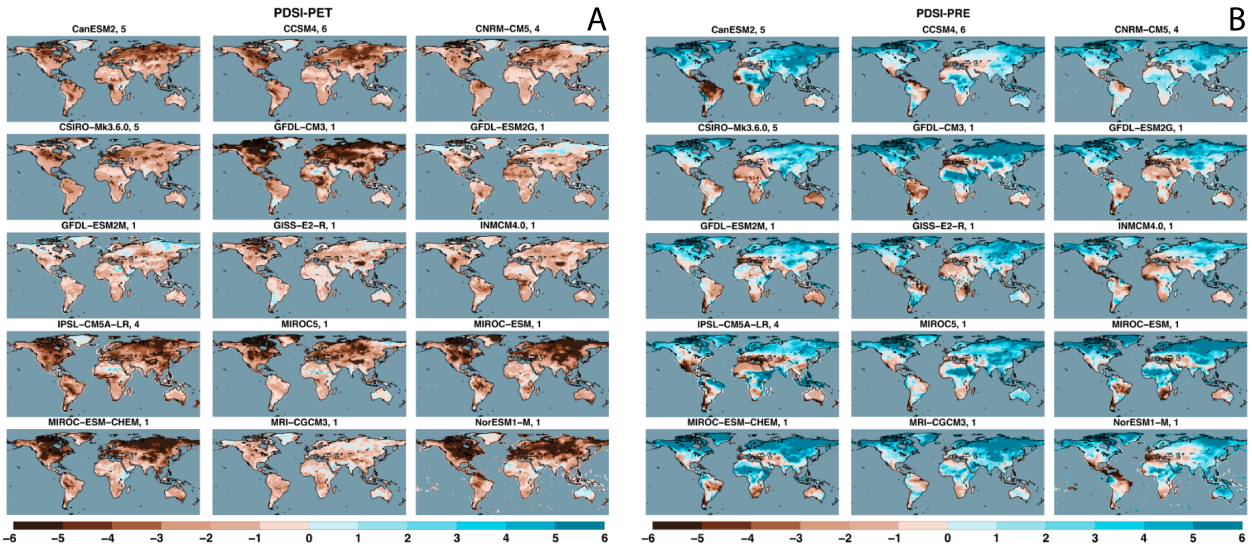

Figure 1.3: Global PDSI averaged from 2080–2099 for the RCP8.5 future emissions scenario. Panel A shows PDSI values calculated with precipitation detrended over the period 2000–2099 and the 21st-century mean set equal to the mean of the last two decades of the 20th-century to isolate the impact of changes in evaporative demand on PDSI. Panel B shows the same but for detrended evaporative demand. The model and number of ensemble members is listed in each panel title; for models with multiple ensemble members, the maps represent the ensemble average. Taken from Cook et al. (2014a).

ASW drying can be split into a contribution from changes in precipitation as opposed to changes in evaporative demand. To do so, the PDSI is recalculated with either the precipitation or evaporative demand detrended over the period 2000–2099 and the 21st-century mean set equal to the mean of the last two decades of the 20th-century. In the former case this would isolate the impact of changes in evaporative demand on PDSI (vice versa for the latter). Figure 1.3 plots the recalculated PDSI. While the CGCMs disagree on the impact of changes in evaporative demand globally, they are in generally good agreement over the ASW (Panel A of Figure 1.3). Panel B of Figure 1.3, however, indicates that the spatial pattern and magnitude of future precipitation changes over the ASW are less certain. When taken together, Figures 1.2 and 1.3 suggest that the ASW will dry over the coming century. The severity of this projected drying, however, is uncertain — particularly the contribution to drying from changes in precipitation. To constrain this uncertainty, the fidelity of each CGCM can be used to distinguish among disparate hydroclimate projections. Unfortunately, we have only limited information on the error and bias structures of CGCMs, particularly

on long timescales (Figures 1.2 and 1.3 plot twenty-year averages at the end of the century). In lieu of better characterizations of CGCMs, there is statistical evidence that a "one model, one vote" approach is the best and most skillful option [Weigel et al. (2010); Knutti et al. (2010)].

Figures 1.2 and 1.3 represent hydroclimate conditions at the end of the century. For a high emissions scenario like RCP8.5, end-of-century precipitation and evaporative demand, relative to the recent past, will be dominated by the response to anthropogenic greenhouse gas forcing. Over the near-term decades, however, hydroclimate change will involve a smaller forced change and a relatively larger contribution from decadal-to-multidecadal internal variability. Hydroclimate projections and associated risk assessments, therefore, require that CGCMs capture *both* forced change and the amplitude and character of internal variability. Very little is known, however, about internal variability on decadal-to-multidecadal timescales (for the reasons outlined in Section 1.1). This includes the ratio of internal to forced variability, which has consequences for the predictability of future hydroclimate, particularly hydroclimate change related to anthropogenic greenhouse gas forcing.

The tropical Pacific ocean provides a stark example of these issues. A wealth of research has implicated tropical Pacific sea surface temperatures (SSTs), and specifically the ENSO, as the dominant driver of drought over the ASW. Schubert et al. (2004a,b), for instance, simulated the 1930s Dust Bowl, the most severe drought of the instrumental interval, as a response to tropical Atlantic and Pacific SST anomalies. Seager et al. (2005b) and Herweijer et al. (2006) subsequently reproduced all of the major droughts of the instrumental interval using an atmospheric general circulation model (AGCM) forced with observed SSTs. Any changes to the tropical Pacific boundary conditions, whether forced or due to internal variability, thus have the potential to impact future hydroclimate over the ASW. Nevertheless, little is known about the characteristics of the tropical Pacific on the decadal-to-multidecadal timescales, which are most relevant for near term climate change. In fact, multiple hypotheses for the origin of decadal-to-multidecadal shifts in the tropical

Pacific have been presented in the literature. Vecchi et al. (2006), for instance, use AGCMs to indicate that high forcing conditions should weaken the atmospheric Walker circulation producing warm, or El Niño-like conditions in the tropical Pacific. This is in contrast to Clement et al. (1996) who show that an ocean model with high forcing conditions simulates La Niña-like conditions via the thermostat mechanism. In support of this argument, the tropical Pacific has become La Niña-like over the latter half of the 21st century (Cane et al., 1997; Karnauskas et al., 2009). It is unclear, however, if this is a response to high forcing conditions from anthropogenic greenhouse gas emissions because internal variability in CGCMs can produce La Niña-like trends of this magnitude (Karnauskas et al., 2012). Potential changes to the variability, not the mean-state of ENSO, are even more poorly constrained (Vecchi et al., 2008; Stevenson et al., 2012), although CGCMs suggest that large changes are possible on multidecadal timescales (Wittenberg, 2009). Most importantly, the CMIP5 CGCMs are in disagreement on the future state of the tropical Pacific (IPCC AR5 — Sections 1.3.2.4.3, 11.3.3.1, 14.4.1 and 14.4.2), although the majority simulate a reduced tropical Pacific gradient, a result that may explain the disparities in hydroclimate projections for the ASW (Figures 1.2 and 1.3 and Seager & Vecchi (2010)).

Despite CGCM agreement on the sign of future changes in hydroclimate over the ASW, much remains to be understood about hydroclimate variability on decadal-to-multidecadal timescales. To improve the basis for accurate predictions of future hydroclimate over the ASW a paleoclimate-model data comparison framework is developed herein (e.g. Section 1.2). To begin, however, we must determine which climate features can inform our understanding of the future. Along these lines, Section 1.3 presents an outline of the C.E. paleoclimate record over the ASW, particularly as it pertains to decadal-to-multidecadal hydroclimate change.

1.3 How might the past inform the future?

Hydroclimate change on decadal-to-multidecadal timescales has been a consistent, though infrequent, feature of the C.E. over the ASW. These so-called megadroughts are unlike any drought observed over the instrumental interval, including the relatively persistent and severe 1930s Dust Bowl and 1950s droughts. While the severity of megadroughts is on par with observed droughts, they are estimated to have been up to a century in length (e.g. Stine, 1994). Megadroughts occurred predominantly during the Medieval Climate Anomaly (MCA), a period of global climate change between approximately 900–1300 C.E. (e.g. Jansen et al., 2007). Nevertheless, they have occurred as recently as the 16th century (Stahle et al., 2007). Understanding the causes of megadroughts is critical for assessing their likelihood of occurrence in the future. In particular, constraining the relative impact of internal versus forced variability on megadrought occurrence will help determine if their risk probabilities will be influenced by anthropogenic greenhouse gas forcing. Likewise, megadroughts represent hydroclimate change on the timescale and of the magnitude projected by CGCMs for the ASW. It is thus critical to determine whether CGCMs are capable of simulating megadrought events and for the correct dynamical reasons. Such evaluations will provide confidence that future projections of drought risk derived from CGCMs adequately incorporate decadal-to-multidecadal hydroclimate variability (e.g Ault et al., 2013, 2014).

It is important to note that megadroughts are a robust feature of the paleoclimate record. They were first identified in submerged tree stands in the Mono Lake Basin of California by Stine (1994) and then independently corroborated using the North American Drought Atlas (NADA — Cook et al., 2007; Herweijer et al., 2007), a tree-ring based reconstruction of hydroclimate variability over NA for the entirety of the C.E. Cook et al. (2010b) note that megadroughts are also a feature of the anthropological record, with Douglass (1935) suggesting that multidecadal drought led to the 12th century abandonment of Pueblo Bonito, a Pueblo settlement of approximately 900 individuals in modern day New Mexico.

Beyond their occurrence and character, however, little is known about megadroughts. In particular, research characterizing the dynamics of megadroughts is in its nascency. Seager et al. (2008a) simulated megadroughts during the MCA with an AGCM forced with SSTs estimated from a single tropical Pacific coral record (Cobb et al., 2003). These simulated megadroughts were analyzed by Burgman et al. (2010), who noted similarities between the global pattern of modeled MCA hydroclimate and the one estimated from paleoclimate proxies. Herweijer et al. (2007) further analyzed megadroughts in the paleoclimate record, employing tree-ring reconstructions from the NADA to compare modern droughts to the megadroughts of the MCA. They proposed that the well-documented ENSO-ASW teleconnection of the instrumental interval (e.g Seager et al., 2005b; Herweijer et al., 2006) was the likely forcing of persistent drought during the MCA, with the difference in drought persistence arising from the duration of drought-favorable SST conditions in the tropical Pacific Ocean. Similar work from Graham et al. (2007), using multi-proxy and modeling methods, also implicates the tropical Pacific along with Indian Ocean SSTs as the principal influences on MCA hydroclimate change. More recently, Feng et al. (2008) and Oglesby et al. (2012) have suggested that the tropical Atlantic played a role in forcing the MCA megadroughts, while Cook et al. (2013) have argued for the importance of dust aerosol forcing from dune mobilization (Forman et al., 2001; Hanson et al., 2010) on both the spatial character and persistence of droughts in NA during the MCA.

Despite the breadth of research, it is clear that a prominent hypothesis is that megadroughts are driven by persistent La Niña-like states in the tropical Pacific. This hypothesis relies in part on the strong control of the tropical Pacific on hydroclimate over the ASW during the instrumental interval. It also invokes the characteristic spatial patterns of megadroughts, which with the exception of the late 16th century event (Stahle et al., 2007) tend to be close to that of a canonical La Niña event (e.g. Herweijer et al., 2007). Perhaps most importantly, there is prominent paleoclimate evidence that suggests that the MCA, the period with the greatest incidence of these features, was characterized by multiple

centuries of persistently La Niña-like conditions.

The highest profile paleoclimate evidence for a persistently La Niña-like MCA comes from Mann et al. (2009). Therein a global dataset comprising multiple proxies is used in a multivariate linear regression framework to reconstruct spatial maps of surface temperature on a regular latitude-longitude grid. A comparison of the MCA temperature field (averaged from 950–1250 C.E.) to the Little Ice Age (LIA — 1400–1700 C.E.) reveals a La-Niña-like pattern of cool temperatures in the eastern tropical Pacific. While this work provides the best direct evidence for cold tropical Pacific conditions contemporaneous with the occurrence of megadroughts, climate field reconstructions (CFRs) like those applied in Mann et al. (2009) contain considerable uncertainties. Pseudoproxy experiments (PPEs — Smerdon, 2012), which use CGCMs as a test bed for CFRs, represent one method by which to constrain this uncertainty. A PPE involves extracting a portion of the spatiotemporally complete CGCM field in a way that mimics the available proxies and instrumental calibration data and then using this subset of CGCM output within a reconstruction framework. The derived reconstruction can then be compared to the inherent CGCM output to assess uncertainty resulting from the reconstruction framework, calibration data, spatial and temporal proxy sampling and the presence of noise within proxy and instrumental data (Smerdon, 2012). Recent work from Smerdon et al. (2011, 2015a) uses PPEs to suggests that all CFR methods produce spatially dependent reconstruction errors, including large mean biases, poor representation of variability in areas with sparse proxy sampling including many dynamically important regions, and biases in the ratio of spectral power at low to high-frequencies.

Of specific relevance to the hypothesis of a cold tropical Pacific Ocean during the MCA, the methodology and proxy network employed by Mann et al. (2009) was analyzed in Smerdon et al. (2015a) with respect to differences in the mean temperature field between the MCA and LIA. Neither the inherent CGCM output nor the PPE reconstructions contain large differences in the Niño3 index, a standard measure of ENSO, between the MCA and LIA. Nevertheless, PPEs can be used to determine if the reconstruction framework of Mann

et al. (2009) can erroneously produce the 0.21 °C difference in in the Niño3 index between the MCA and LIA (as shown in Mann et al., 2009). Randomly chosen and independent 300-year periods (the length of the MCA and LIA) were selected, repeated 1000 times, from both the inherent CGCM output and the associated PPEs. Figure 1.4 plots the fraction of the time that the squared difference in the mean Niño3 indices between the two randomly drawn periods is as large as the difference in Mann et al. (2009) (differences are squared to avoid the arbitrary distinction of which period is warmer or colder in this experiment). Only the IPSL model contains any paired periods in which the inherent CGCM output has a mean Niño3 temperature difference that is equal or greater than the MCA-LIA difference in the Mann et al. (2009) reconstruction. More remarkably, however, the CCSM and GISS PPEs both yield reconstructions that generate periods in which the differences in the Niño3 index are above the value of the Mann et al. (2009) MCA-LIA difference, even when the inherent CGCM output contains no such periods. This suggests that the Mann et al. (2009) reconstruction framework can produce a La Niña-like MCA erroneously and by consequence that this result is potentially not robust. More generally, these findings imply that the atmosphere-ocean state during the MCA and the association between megadroughts and the tropical Pacific Ocean deserves further study.

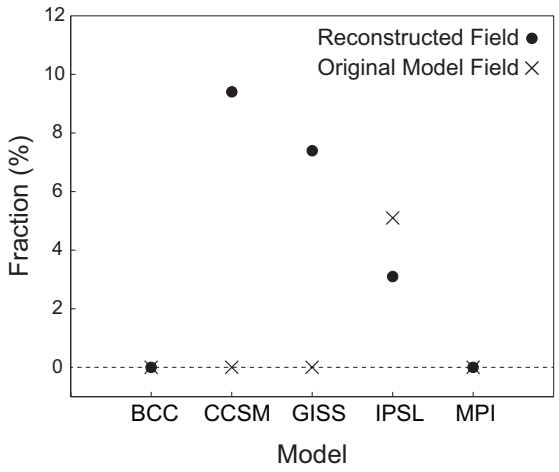

Figure 1.4: Fraction of 1000 randomly selected 300-year pairs with a squared difference in the mean Niño3 index ($^\circ C^2$) larger than the MCA and LIA squared difference in the Niño3 index from Mann et al. (2009). The circles are based on the Niño3 index taken from the PPEs from each model and the crosses are based on the true model Niño3 index. From Smerdon et al. (2015a).

1.4 What questions are addressed in this dissertation?

Herein we will use a paleoclimate-model data comparison framework to study megadroughts over the ASW. Specifically, whether or not state-of-the-art CGCMs simulate megadroughts, and if so, what are the dynamics that underlie these features (Chapters 3 and 5). A particular focus will be given to the impact of forcing, relative to internal variability in driving simulated megadroughts. Additionally, the model dynamics will be characterized to determine why forced or internal variability is important, as well as to better understand the atmosphere-ocean dynamics through which this variability is expressed (Chapter 4). Finally, the seasonality and spatial features of simulated megadroughts will be analyzed and compared to the paleoclimate record (Chapter 6). Together these studies will additionally be used to constrain uncertainty in real-world megadroughts dynamics, with Chapter 7 using the paleoclimate record to estimate the atmosphere-ocean state that produced these features.

The paleoclimate-model data comparison framework will employ the most recent versions of the NADA (Cook et al., 2007, 2014b) and other independent (Griffin et al., 2013) tree-ring based reconstructions of hydroclimate variability for the C.E. in combination with

forced transient simulations of the last millennium and 500-year pre-industrial control runs from the Paleoclimate Model Intercomparison Project Phase 3 (PMIP3 — Schmidt et al., 2011) of the Coupled Model Intercomparison Phase 5 (CMIP5 — Taylor et al., 2012) and other sources (González-Rouco et al., 2006). The motivating questions are:

1) How will ASW hydroclimate respond to increasing greenhouse gas concentrations over the next decade to century?

2) How will these forced changes combine with internal variability to determine the actual impacts of hydroclimate change?

3) Are CGCMs able to capture the full range of the internal and forced components of past hydroclimate change on decadal-to-multidecadal timescales?

4) Can these CGCMs potentially inform our understanding of past hydroclimate change on decadal-to-multidecadal timescales?

Chapter 2

Methods

2.1 Data

2.1.1 Paleoclimate

Reconstructed PDSI data in Chapters 3 and 5 are from the NADA version 2a, the full details of which can be found in Cook et al. (2007). The data are reconstructed on a 2.5° latitude by 2.5° longitude grid of summer [June, July, August (JJA)] average PDSI values for the United States, as well as southwestern Canada and northern Mexico (286 grid points in total). The summer PDSI is reconstructed from a network of 1854 annual tree-ring records using a nested point-by-point regression method to produce records of maximal length. Verification statistics indicate that all grid points for the chosen analysis period (at most back to 850 C.E.) and western NA region are highly statistically significant (decadal values of multiple determination, reduction of error, and coefficient of efficiency are greater than 0.7 for a 33-year verification interval over much of the ASW; Cook et al., 2010b). Chapters 6 and 7 use an updated version of the NADA version 2a, with improved spatial coverage and resolution, the full details of which can be found in Cook et al. (2014b). The data are reconstructed on a 0.5° latitude by 0.5° longitude grid of JJA-average PDSI values.

In Chapter 7 we use two additional tree-ring based PDSI reconstructions for other Northern Hemisphere (NH) regions. The first is the Old World Drought Atlas (OWDA — Cook, in review), also reconstructed on a 0.5° latitude by 0.5° longitude grid of JJA average PDSI values using 106 tree-ring chronologies from across Europe. Both the NADA and OWDA in Chapter 7 are used over the period 1000–2005 C.E. The second is the Monsoon Asia Drought Atlas (MADA — Cook et al., 2010a), reconstructed on a 2.5°latitude by 2.5° longitude grid of JJA average PDSI values using 327 tree-ring proxy records. The MADA will be employed over the period 1250–2005 C.E. for which there is sufficient sample depth over the spatial range (Anchukaitis et al., 2012). In Chapter 7 all three reconstructed PDSI datasets have been regridded to a common 2.5° latitude by 2.5° longitude grid.

To assess the seasonality of megadroughts in Chapter 6 we employ an additional tree-ring based reconstruction of hydroclimate variability from Griffin et al. (2013). Therein, Standardized Precipitation Index (SPI — McKee et al., 1993) values are reconstructed from a collection of more than 50 tree-ring chronologies with seasonal resolution. The data are reconstructed as a single timeseries for the North American Monsoon (NAM) 2 region (113.25°W–107.75°W, 30°N–35.25°N — Gochis et al., 2009), a subset of the larger ASW region. The reconstruction uses forward stepwise multiple linear regression independently for both the winter (cool — October to April) and summer (warm — June to August) seasons between the period 1539–2008 C.E. This involves separating the systematic dependence of latewood (the dark, dense component of tree rings with a greater warm-season signal) variability from the earlywood (light, less dense component with a greater cool-season signal) variability using linear regression, with the effect of this adjustment being an increase in the summer precipitation signal (Griffin et al., 2011). The relationships between the instrumental and reconstructed variables in Griffin et al. (2011) are highly significant, positive and stable.

2.1.2 Observed

Observed sea surface temperature (SST) data are from two sources. In Chapters 3 and 6 we use the Kaplan extended SST V2 product, which is a 5° latitude by 5° longitude gridded SST field for the period 1856–present (Kaplan et al., 1998). In Chapters 6 and 7 we additionally use the National Oceanic and Atmospheric Administration (NOAA) extended reconstructed SST dataset (Smith & Reynolds, 2003) covering the period 1854–present. These are both standard and comparable datasets that are well validated in the literature.

Observed hydroclimate data are from two sources. In Chapters 3 and 6 precipitation data comes from the the Global Precipitation Climatology Center (GPCC — Becker et al., 2013). In Chapter 6, PDSI data are from a global dataset for the period 1870–2012 C.E. (Dai et al., 2004). This dataset was derived on an even 2.5° latitude by 2.5° longitude grid using observed precipitation and temperature data as inputs. For the analyses herein, the JJA monthly PDSI values have been averaged to create a single PDSI anomaly for each year. Additionally, only the period after 1950 C.E. will be employed, as this is the period over which the full NA PDSI grid is available.

Chapter 4 additionally uses reanalysis SST and geopoentential height data from the National Oceanic and Atmospheric Administration NCEP-NCAR Climate Data Assimilations System 1 project (Kalnay et al., 1996). The monthly-resolved data span the period 1949–2012 C.E. on a 2.5° latitude by 2.5° longitude grid. The reanalysis product uses a frozen analysis/forecast system with data assimilation of past observations and is an established data set for assessment of interannual upper-air variability. Chapter 7 also employs reanalysis upper-air data, however, the analyses require a longer record than that provided by the NCEP-NCAR reanalysis. By consequence, the NOAA 20th century reanalysis (Compo et al., 2011) is used in Chapter 7.

2.1.3 Model

Chapter 3 uses output from the ECHO-G CGCM that combines the ECHAM4 and Hamburg Ocean Primitive Equation global (HOPE-G) atmospheric and ocean models, respectively (Legutke et al., 1999). The resolution of the atmosphere is T30 horizontal (3.75°) by 19 vertical levels, while the ocean resolution is 2.8° in the zonal direction (T42) with equatorial refinement in the meridional direction that varies from 2.8° latitude at the poles to 0.5° at the equator with 20 vertical levels. The model employs a time-invariant adjustment of heat and freshwater fluxes. We use model SSTs, 2-m surface air temperature (SAT), precipitation, evaporation, sea level pressure, and soil moisture. The ECHO-G soil moisture model component is a single-layer bucket model with reservoir capacity varying based on soil type (Legutke et al., 1999). For our purposes herein, the SAT, precipitation, and soil moisture are regridded from their native resolution to an even 2.5° latitude by 2.5° longitude grid.

We use two ECHO-G simulations. The first is a 1000-year control simulation (clipped to 989 years to match the length of the forced simulation used herein) that is run with constant external forcing set to mid-20th-century conditions. The second simulation is the ERIK2 forced transient run (González-Rouco et al., 2006) spanning 990 years (1000–1990 C.E.; note that subsequent analyses are over 989 years, 1000–1989 C.E., owing to the employed yearly averaging interval of October-September) and driven by an estimated suite of external forcing factors including radiative effects of volcanic aerosols, concentrations of atmospheric constituents, and solar irradiance (Zorita et al., 2005). The run was initialized with pre-20th-century conditions and spun up for 100 years to the historical forcing of 1000 C.E. (González-Rouco et al., 2006).

Internal variability of 2-m SAT, sea level pressure (SLP), and precipitation in the ECHO-G control run was evaluated by Min et al. (2005a), who demonstrate that the model is capable of producing overall observed variability for all three of these variables. In a companion paper, Min et al. (2005b) addressed the model treatment of interannual to decadal-

scale internal variability using the same control run. They found that ENSO in the ECHO-G model exhibits stronger than observed amplitude and is too frequent and regular, with an excessive spectral peak at 2 years and muted variability in the 3–9-year range. Importantly, the model produces reasonable ENSO spatial structures and teleconnections (Min et al., 2005b). Collectively, the ECHO-G simulations have been extensively analyzed (e.g. Von Storch et al., 2004; Zorita et al., 2003; Stevens et al., 2007; González-Rouco et al., 2009; Karnauskas et al., 2012). At the beginning of the project these simulations were the only available millennium-length forced and control runs using the same model, configuration and resolution. This, along with the well characterized and vetted performance of the model, made the ECHO-G simulations a comprehensive and consistent framework for an initial assessment of megadrought dynamics.

Chapters 5, 6 and 7 use model output from the CMIP5/PMIP3 archive. We employ six last-millennium (LM) transient simulations forced with reconstructed time-varying exogenous forcings from 850 to 1850 C.E. (Schmidt et al., 2011). These simulations have been appended to the first ensemble member of the CMIP5 historical runs that span the period 1850–2005 C.E. to produce a model record from 850 to 2005 C.E. Although these simulations are not continuous, both the historical and LM simulations have the same model configuration and resolution. Consequently, if the simulations have no drift, the discontinuity at 1850 C.E. should fall within the range of simulated climate variability. A large temperature drift in the MIROC LM simulation (Sueyoshi et al., 2013) likely violates this assumption, while a drift in the early centuries of the GISS LM simulation (Bothe et al., 2013) is likely to have less of an impact. While model drift undoubtedly impacts the hydroclimate variables assessed in this study, the effects are presumed to be moderate given the absence of drift in precipitation (Gupta et al., 2013). The 500-year control simulations with constant preindustrial forcing conditions (also from CMIP5) were additionally analyzed to aid in the interpretation of the LM model results. All model output has been regridded to a common 2.5° latitude by 2.5° longitude grid (this represents a coarsening of the model resolution for four out of the six

models). Chapter 4 uses the six forced and control simulations as well as eleven additional 500-year control runs that are also from the CMIP5. As a compliment to the fully-coupled runs in Chapter 4, we additionally use an uncoupled atmosphere-only ensemble comprising 10 sets of atmosphere model simulations with ensemble sizes between 1 and 10 from the Atmospheric Model Intercomparison Project (AMIP — a total of 32 simulations) also of the CMIP5. Each ensemble member consists of an atmospheric simulation forced with the same observed SST boundary conditions for the period 1979–2008 C.E. For all model simulations we use inherent model output such as surface temperature, precipitation, geopotential height, sea level pressure, surface pressure, land-sea mask and soil moisture, as well variables derived from inherent model outputs using standard definitions (surface net radiation and vapor pressure). The analyzed models and expanded model names are provided in Figure 2.1.

The CMIP5/PMIP3 was the first coupled model intercomparison project in which multiple last-millennium (LM), historical, control and future simulations using the same model configurations and resolutions were produced (Taylor et al. 2012). This development makes possible a wide range of model analyses and comparisons between paleoclimatic data and LM simulations with direct quantitative applicability to historical simulations and future projections. Importantly, the CMIP5/PMIP3 simulations are produced using state-of-the-art CGCMs and therefore embody our latest efforts to model the coupled components of the climate system. This includes future projections derived from these CGCMs, which are our current best guess at the future state of the climate system under different emissions scenarios. Together this makes the CMIP5/PMIP3 archive an important target for the study of megadroughts and more generally hydroclimate change over the ASW. Additionally, the CMIP5/PMIP3 model dynamics have been thoroughly vetted over NA (Sheffield et al., 2013a,b; Maloney et al., 2014; Seager et al., 2014b), including hydroclimate dynamics on up to decadal timescales (Sheffield et al., 2013b; Langford et al., 2014). This represents an ideal starting point for the analysis of megadrought dynamics in Chapters 4, 5 and 6.

Modeling Center	Institute ID	Model Name
Commonwealth Scientific and Industrial Research Organization (CSIRO) and Bureau of Meteorology (BOM), Australia	CSIRO-BOM	ACCESS1.3
Beijing Climate Center, China Meteorological Administration	BCC	BCC-CSM1.1
Canadian Centre for Climate Modelling Analysis	CCMA	CanEMS2, CanAM4
National Center for Atmospheric Research	NCAR	CCSM4
Center National de Recherches Météorologiques/Centre de Recherche et Formation Avancée Calcul Scientifique	CNRM-CERFACS	CNRM-CM5
Commonwealth Scientific and Industrial Research Organization in collaboration with Queensland Climate Change Centre of Excellence	CSIRO-QCCE	CSIRO-Mk3.6.0
First Institute of Oceanography, SOA, China	FIO	FIO-ESM
LASG, Institute of Atmospheric Physics, Chinese Academy of Sciences	LASG-IAP	FGOALS-gl
NOAA Geophysical Fluid Dynamics Laboratory	NOAA GFDL	GFDL-ESM2G, GFDL-ESM-2M, GFDL-HIRAM-C180
NASA Goddard Institute for Space Studies	NASA GISS	GISS-E2-R
Institute for Numerical Mathematics	INM	INM-CM4
Institute Pierre-Simon Laplace	IPSL	IPSL-CM5A-LR
Japan Agency for Marine-Earth Science and Technology, Atmosphere and Ocean Research Institute (The University of Tokyo), and National Institute for Environmental Studies	MIROC	MIROC-ESM
Max-Planck-Intitut für Meteorologie (Max Planck Institute for Meteorology)	MPI-M	MPI-ESM-LR, MPI-ESM-P
Meteorological Research Institute	MRI	MRI-AGCM2-2H, MRI-CGCM3
Norwegian Climate Centre	NCC	NorESM1-M

Figure 2.1: Information on the CMIP5/PMIP3 models.

2.2 Drought Variables

2.2.1 Soil Moisture

To assess modeled drought conditions in Chapter 3 we use soil moisture (normalized over the length of the simulation) from the ECHO-G forced and control model runs. We use annually-averaged soil moisture from the model, while the NADA PDSI used for comparison represents a JJA average. There were three principal motivations for using the annually-averaged soil moisture instead of the JJA average or the model-derived PDSI.

First, annual-mean soil moisture provides a wide enough temporal window for addressing megadroughts and their dynamical causes. In particular, droughts driven by winter precipitation in the ECHO-G model (as are common for the ASW) will not necessarily produce a strong hydroclimate signal in mean summer (JJA) soil moisture (the modeled soil moisture memory timescale is 4–5 months versus 12–18 months for the PDSI). Secondly, soil moisture is the model variable of most direct physical relevance to drought. Thirdly, the PDSI formulation has an unrealistic dependence on temperature that causes a strong drift toward negative values in the modeled during the 20th century, which is in neither the NADA PDSI nor the model soil moisture (not shown). The negative drift of PDSI is a consequence of the temperature dependence of the Thornthwaite (Thornthwaite, 1948) equation for potential evaporation used in the PDSI calculation and the excessive contemporary temperature trends in the model. Similar issues with the temperature dependence of PDSI have been raised in the literature (Sheffield et al., 2012; Burke & Brown, 2008; Milly & Dunne, 2011). Normalized soil moisture is thus chosen as it provides a comparable analog to the PDSI, which is intended to represent a locally normalized anomaly of moisture supply and demand (Dai et al., 1998, 2004).

Although the simple bucket soil moisture scheme in the ECHO-G model may be problematic, soil moisture captures the influence of temperature and precipitation variability and considers snow water storage and melt, water interception by vegetation during rain or snow-melt episodes (skin reservoir), and water infiltration and runoff (Dumenil, 1992). Nevertheless, it must be noted that more complicated soil vegetation atmosphere transfer (SVAT) schemes have the potential to alter results.

2.2.2 PDSI

In Chapters 5 and 6 we use PDSI derived from the models. The motivation for this choice is the range in the complexity and resolution of soil moisture schemes in the CMIP5 models. These inter-model differences make a direct comparison of inherent model soil moisture impossible. PDSI, however, is an offline estimate of soil moisture balance that can be

calculated consistently across the model simulations to provide a directly comparable metric of hydroclimate variability. It has the added benefit of being the varaible reconstructed in the NADA, the paleoclimate product that is used for comparison in Chapters 5 and 6. We will thus calculate PDSI for each model simulation.

PDSI is calculated from supply via precipitation and losses due to evapotranspiration (ET). PDSI ET is estimated by means of scaling potential evapotranspiration (PET) using a fixed beta function that is meant to represent vegetative controls on transpiration (e.g., stomata closure to reduce moisture stress). PET is often estimated using surface temperature via the Thornthwaite method (Thornthwaite, 1948). Because Thornthwaite-estimated PET is essentially a rescaling of surface temperature, it overestimates the PET influence on PDSI when temperatures far exceed the climatology of the PDSI standardization interval (as noted in Section 2.3.1 as the motivation for using soil moisture as the hydroclimate metric in Chapter 3; see also Milly & Dunne, 2011; Sheffield et al., 2012; Dai, 2013; Smerdon et al., 2015b). For a detailed treatment of the differences in PET estimates based on temperature, net radiation, and other physical variables, see the supplementary material of Sheffield et al. (2012). In this case we use model surface net radiation (RNET) to estimate PET. To do so, simulated monthly RNET (W/m^2) was set equal to PET (mm/day). This is equivalent to assuming that RNET is exactly balanced by latent heat through ET (with sensible heat flux equal to zero). The ideal method for computing PDSI is to estimate PET via the Penman-Monteith (PM) method, which includes the effect of the vapor pressure deficit along with the impact of RNET (a more detailed treatment of PM PDSI can be found in Sheffield et al., 2012; Cook et al., 2014a; Smerdon et al., 2015b). Unfortunately, the necessary model fields to compute PM PET were only available for three out of the six analyzed LM simulations. A comparison of the RNET and PM PDSI for these three simulations is included in Section 2.5.2. Unless otherwise specified, PDSI will be used throughout the remainder of this dissertation to specifically designate PDSI calculated using the RNET formulation.

For the analyses performed herein, model PDSI is derived on an even 2.5° latitude by

2.5° longitude grid. At each grid point, PDSI was calculated and then standardized against an instrumental normalization period (1931–1990 C.E.) for the forced simulations and the full 500-year period for the control simulations. The instrumental normalization period is the same time interval used by the National Oceanic and Atmospheric Administration for normalization of their PDSI calculations (Cook et al., 2014b), which were subsequently used as the target PDSI for the paleoclimate reconstructions described below. Soil moisture capacity was specified as 25.4 and 127 mm in the top and bottom layers of the PDSI calculation, respectively. The PDSI was averaged over JJA to produce a single average for each year; hereinafter, any mention of PDSI will be with regard to the JJA average values. PDSI with an absolute value over 10 was removed by replacement with the average PDSI of the eight neighboring grid points at that time step as a means of removing unrealistically anomalous PDSI values. This method for removing outliers is consistent with that used by van der Schrier et al. (2011) in the calculation of their observed PDSI dataset.

2.2.3 SPI

To provide a direct comparison to the Griffin et al. (2013) reconstruction in Chapter 6 we will additionally calculate the model SPI. For each CMIP5/PMIP3 model simulation, precipitation totals were converted to SPI for October–April (winter or cool season) and June–August (summer or warm season), with the α and β parameters of the gamma distribution computed for the 1896–2005 C.E. period. These choices match the SPI-reconstructed target variable in Griffin et al. (2013).

2.3 ASW and SW Regions

The ASW is defined in Chapters 3, 5 and 7 as 25°–42.5°N, 125°–105°W. This box is somewhat more restricted than that of Meehl & Hu (2006) and Herweijer et al. (2007), who also analyzed megadroughts over southwestern NA. The more restricted ASW definition was

chosen in order to maintain a homogeneous sample area, as determined by analyses of the spatial variance of soil moisture in the forced and control runs from the ECHO-G model (not shown). Chapter 6 uses a more latitudinally confined definition of the ASW in order to maintain consistency with an analysis of pancontinental drought from Cook et al. (2014b). The analysis region in Chapter 6 is 32°–40°N, 125°–105°W and this will be called the SW hereinafter in order to differentiate from the ASW in Chapters 3 and 5. A comparison of PDSI from the NADA (Cook et al., 2014b) averaged over these two regions for the period 1000–2005 C.E. indicates that there is good agreement in variability between the SW and ASW with a correlation of 0.99 on both interannual and decadal timescales. The SW and ASW are thus comparable regions for analysis of megadrought dynamics. We additionally use the NAM2 region (113.25°W–107.75°W, 30°N–35.25°N — Gochis et al., 2009) in Chapter 6 to match the reconstruction of Griffin et al. (2013). The same comparison between the ASW and NAM2 regions in the NADA gives correlations of 0.88 and 0.85 on interannual and decadal timescales, respectively.

Importantly, the ASW encompasses two distinct hydroclimate regimes, with winter precipitation produced by midlatitude eddies and summer precipitation controlled by NAM dynamics. To the extent possible, model biases in the simulation of these hydroclimate regimes will be related to the model-derived PDSI used in Chapters 5 and 6 in Section 2.5.3. Relating model biases in the simulation of precipitation to the soil moisture used in Chapter 3 is less important, as soil moisture is an inherent model output with much shorter memory timescales. Nevertheless, ECHO-G soil moisture will dominantly reflect winter precipitation conditions because the model lacks a NAM (not shown) likely as a result of the coarse model resolution (e.g. Langford et al., 2014), although Cook & Seager (2013) found no relationship between model resolution and the simulation of the NAM.

For the majority of analyses herein the drought variables at each grid point in the ASW or SW were averaged to create single timeseries of drought variability. This timeseries will be used for the identification of megadroughts, the methodology for which is explained

in Section 2.4.

2.4 Metrics

2.4.1 Drought Identification

Drought definitions vary in terms of both input data (e.g., PDSI versus precipitation) and criteria. We employ a drought definition similar to that described in Herweijer et al. (2007), with a drought commencing after two consecutive years of negative soil moisture (Chapter 3), PDSI (Chapters 5, 6 and 7) or SPI (Chapter 6) anomalies and continuing until two consecutive years of positive anomalies (the 2S2E definition). Herweijer et al. (2007) required one year to start a drought and included a criterion based on spatial extent, which is not used herein. The adopted definition is different but broadly consistent with the drought definition of Meehl & Hu (2006), who define drought as consistently negative anomalies in an 11-year running mean timeseries of box average precipitation (droughts begin with the first year of anomalously negative precipitation and end in the first year of anomalously positive precipitation in the filtered timeseries).

2.4.2 Drought Ranking

Megadroughts are the most persistent and severe of drought features in the ASW over the C.E. The droughts identified using the 2S2E definition thus must be ranked to determine which are the most persistent and severe and by consequence characteristic of megadroughts. To do so, the identified droughts were ordered by creating a cumulative drought severity or drought density rank. For each drought period, the soil moisture (Chapter 3), PDSI (Chapters 5, 6 and 7) or SPI (Chapter 6) was summed from the first to the last year of the drought. These values were subsequently ranked by the negative value of the sum. This cumulative drought severity ranking was chosen over a purely length-based ranking in order to incorpo-

rate both the persistence and severity of each drought. The 2S2E and cumulative drought severity method will hereinafter be referred to as the drought identification metric.

We will predominantly analyze the top five highest-ranking (or most persistent and severe) droughts. Although this cutoff is arbitrary, the analysis of five events is sufficient to determine if there is consistency in the simulated atmosphere-ocean states during persistent and severe drought. More generally, the choice of drought identification metric and the analysis of the top five highest-ranking droughts, while defensible, is not highly important as understanding the dynamics underlying persistent and severe drought does not require an objective determination of the timing of each drought and its severity.

2.5 Variable Comparison

2.5.1 ECHO-G Soil Moisture

The annually and spatially averaged normalized precipitation, precipitation minus evaporation (P-E), and soil moisture over the ASW region are highly correlated in the ECHO-G simulations (e.g., there is a 0.86 correlation between the soil moisture and precipitation ASW indices). Furthermore, yearly averaged soil moisture closely resembles the JJA average soil moisture for the ECHO-G model with a correlation of 0.70 between the two indices for the control run. The use of yearly average soil moisture is further justified by the agreement between the droughts identified in the annual and JJA soil moisture indices from the ECHO-G control run (8 of the 10 highest-ranking droughts in the control run are in agreement using the drought identification metric).

We also calculated model PDSI to allow for a direct comparison between simulated soil moisture and PDSI variability in the ECHO-G model (following Cook et al., 2013). Model PDSI is derived on an even 2.5° latitude by 2.5° longitude grid using simulated precipitation and surface temperature as inputs. At each grid point PDSI was calculated and then standardized against a preindustrial normalization period (1000–1850 C.E.). Soil mois-

ture capacity was specified as 25.4 and 127 mm in the top and bottom layers, respectively, and evapotranspiration was calculated using surface temperature via Thornthwaite (1948). While additional PDSI formulations have been investigated and shown to be preferable over the Thornthwaite formulation (see Sections 2.2.1 and 2.2.2), this original calculation (using the standard formulation at the time of analysis) was sufficient for testing the relationship between PDSI and soil moisture in the ECHO-G simulation.

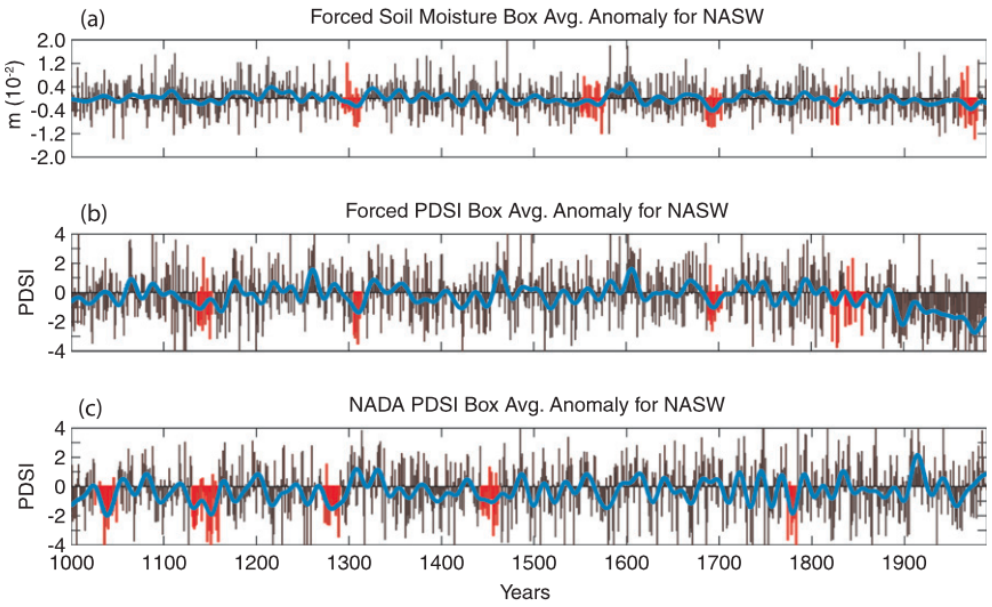

Figure 2.2: (a) Unnormalized forced soil moisture (m) and (b) Forced PDSI from the ECHO-G simulations and (c) The NADA PDSI; all variables are averaged over the ASW region. The soil moisture is a yearly average, while the PDSI is a JJA average. The top five highest-ranking droughts using the drought identification metric are highlighted in red, with the 20-yr low-pass filtered timeseries plotted in blue.

The simulated ASW soil moisture variability in the ECHO-G model correlates well (correlation coefficient of 0.75) with calculated model PDSI. The two records diverge in the postindustrial period owing to an unrealistically large negative 20th-century PDSI trend in the model simulation that can be attributed to an excessively positive temperature trend — more than twice the observed trend — and slightly negative precipitation trend (Figure 2.2). If the modern/postindustrial period is neglected, the identified droughts using the two variables are consistent in three out of five cases. The exceptions are the late 1500s drought,

which is the least severe of the five droughts identified in the soil moisture timeseries, and the 12th-century and late 19th-century droughts in the PDSI timeseries; this latter two droughts are present but much smaller in magnitude for the soil moisture timeseries (and thus not identified as one of the five highest-ranking droughts in the timeseries). The disagreements in drought timing and magnitude seem to be associated with strong temperature controls on calculated PDSI that are not reflected in the modeled soil moisture response. This can be observed most dramatically in the PDSI estimates for the 20th century in the forced run.

In terms of drought severity, the model exhibits approximately as much interannual and longer timescale PDSI variability in the ASW region as the proxy record (see the bottom two panels of Figure 2.2). Although the PDSI has been noted to be difficult to compare in an absolute sense (Dai et al., 1998, 2004), the model megadroughts appear similar in severity to those in the paleoclimate record. An analogous comparison between the forced and control simulations indicates that soil moisture variability is comparable in each. In particular, both model simulations have the same soil moisture variance in the ASW (30.25 mm^2). Subsequent comparisons (Chapter 3) of forced and control responses in normalized soil moisture timeseries, therefore, can be interpreted as equivalent in their range of variance and can be compared to the NADA PDSI timeseries.

2.5.2 CMIP5/PMIP3 PDSI

As stated in Section 2.2.2, the excessive temperature dependence of the Thornthwaite (1948) PDSI formulation (used in the previous section) necessitates the use of alternative PDSI formulations for the multi-model comparisons completed herein (Chapter 5). Two options are the RNET and PM PDSI formulations and RNET PDSI will be used instead of PM PDSI for the following three reasons: 1) the required input fields for PM PDSI are only available for three of the six employed models; 2) there is general agreement in drought timing and severity between the PM and RNET PDSI when using the drought identification metric; and 3) there is close agreement between the RNET and PM PDSI on both interannual and decadal timescales. We demonstrate support for justifications two and three in the

remainder of this section.

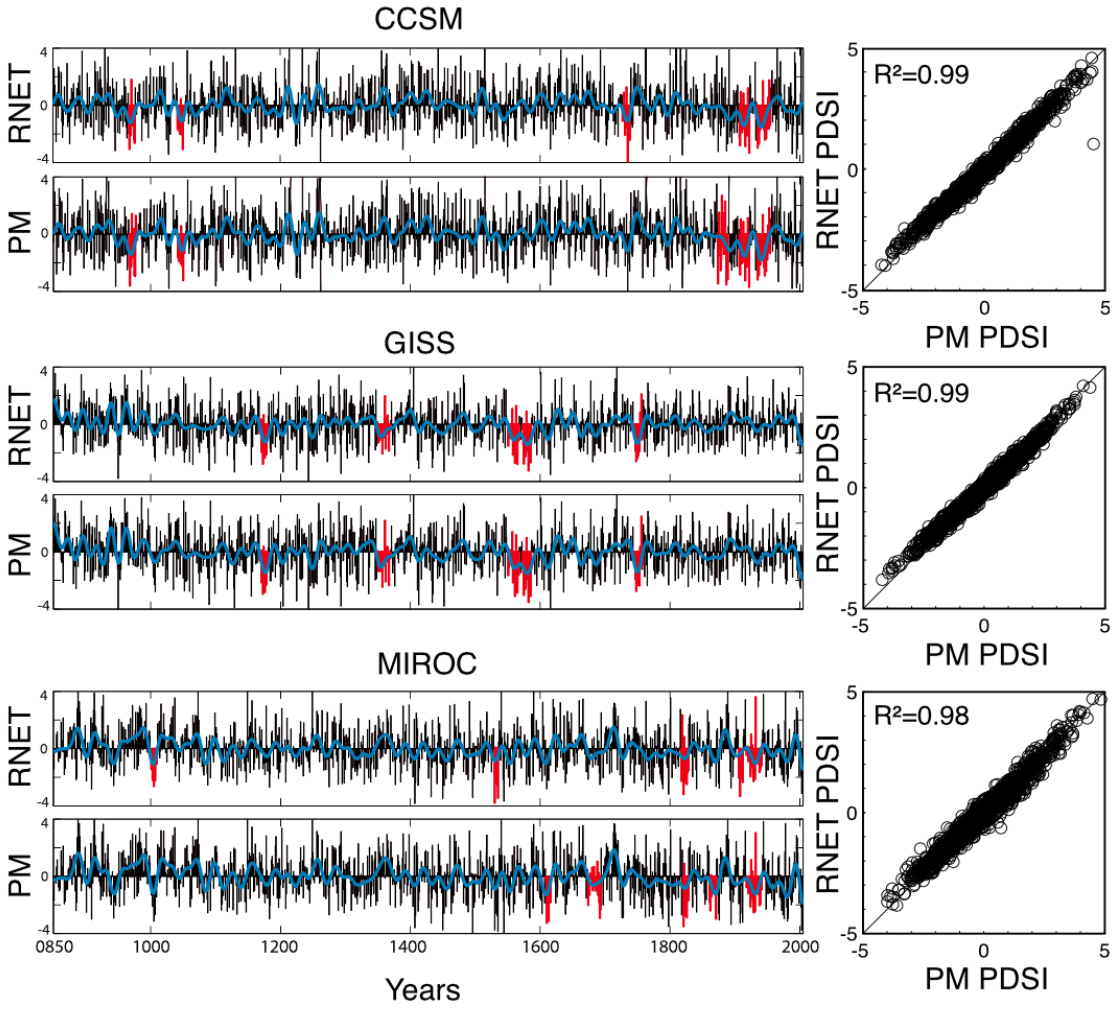

Figure 2.3: (left) RNET and PM PDSI timeseries for the period 850–2005 C.E. averaged over the ASW region for the three simulations that have provided the necessary output fields. Annual anomalies (black lines) are shown, along with smoothed versions using a 20-year low-pass filter (blue lines). The red highlighted periods in the annual timeseries are the five highest-ranking droughts in each model, as determined by the drought identification metric. (right) The ASW average PM PDSI is plotted against RNET PDSI over the same period used for the (left) timeseries plots and indicates the two calculated indices to be very similar (one-to-one lines are shown as black solid lines in each plot).

The right panels in Figure 2.3 show a comparison of the PM and RNET PDSI for the CCSM, GISS and MIROC simulations. There is good agreement between the ASW average PM and RNET PDSI timeseries, with R^2 values on interannual and decadal (not shown) timescales of approximately 0.99. Figure 2.3 also identifies for each model the five highest-

ranking droughts in the PM and RNET PDSI timeseries using the drought identification metric. For 11 of 15 cases, the same drought was identified in the two PDSI timeseries, and each of the five highest-ranking droughts identified in the RNET PDSI are also droughts in the PM PDSI. These results indicate that any differences in drought identification between PM and RNET PDSI result from a reordering of the droughts as ranked by cumulative drought severity. Additionally, it is important to note that simulated PDSI compares well with other soil moisture metrics (e.g., the standardized precipitation evapotranspiration index; Vicente-Serrano et al., 2010; Cook et al., 2014a) and model soil moisture (Section 2.5.1 and Cook et al., 2014a, 2015; Smerdon et al., 2015b).

2.5.3 CMIP5/PMIP3 Biases and PDSI

The PDSI calculation used herein incorporates model precipitation and net radiation to estimate soil moisture balance. Observations of surface energy balance are difficult to come by (e.g. Wild et al., 2013), and because PDSI is dominated by precipitation variability (e.g. van der Schrier et al., 2011), simulated surface net radiation biases will not be analyzed. Biases pertaining to model simulation of the spatial and temporal distribution of precipitation, however, are well documented (e.g. Stocker et al., 2014, , sections 9.5.2.4 and 9.6.1.1). The ASW encompasses a significant portion of the NAM region (Gochis et al., 2009) and thus has both winter and summer precipitation driven by largely independent atmosphere-ocean dynamics (winter precipitation is related to transient midlatitude eddies, while summer precipitation is controlled by the monsoon dynamics). Here we compare the model precipitation to observed data from the Global Precipitation Climatology Centre (GPCC) for the period 1951–2010 C.E., for which there are 26 precipitation stations over the ASW (Becker et al., 2013).

The spatial distribution of precipitation for the winter [November–April (NDJFMA)] and summer [May–October (MJJASO)] half years is plotted in Figure 2.4. Models reproduce many elements of the observed precipitation distribution, the main exceptions being a

tendency to simulate precipitation that is not limited spatially to the western coastal region in winter and to the southeastern portion of the ASW in summer, and difficulty simulating summer precipitation that peaks sharply in midsummer. In each case, these model biases can be related to the relatively coarse inherent model resolution that prevents a realistic simulation of orographic features. The erroneous spread of winter precipitation away from the coast, for instance, is largely due to the models not resolving the western NA coastal mountain ranges that effectively remove moisture from incoming westerlies and storm systems (e.g. Sheffield et al., 2013a). Additionally, realistic simulation of the NAM is predominantly found in the CMIP5 models with high spatial resolution (Langford et al., 2014).

Of the models analyzed herein, the MPI model simulates the observed spatial and temporal precipitation characteristics with the greatest fidelity. MIROC exhibits a large summer precipitation bias over the northeastern half of the ASW and, along with BCC, simulates winter precipitation that is not localized along the western coastal region as observed. In contrast, CCSM, GISS, and IPSL all simulate a reasonable spatial distribution of winter precipitation, although the amount of precipitation is too large in all of the model simulations. For summer precipitation, neither GISS nor IPSL simulates summer precipitation in the southeastern portion of the ASW. CCSM, on the other hand, simulates relatively realistic summer precipitation, but it does not peak sharply in midsummer as observed. The BCC model has a summer precipitation maximum in the ASW that is approximately correct in its spatial distribution, but the feature extends too far eastward outside of the ASW box, and it likewise does not peak in midsummer. Additionally, all of the models overestimate the magnitude and variability of ASW precipitation (not shown).

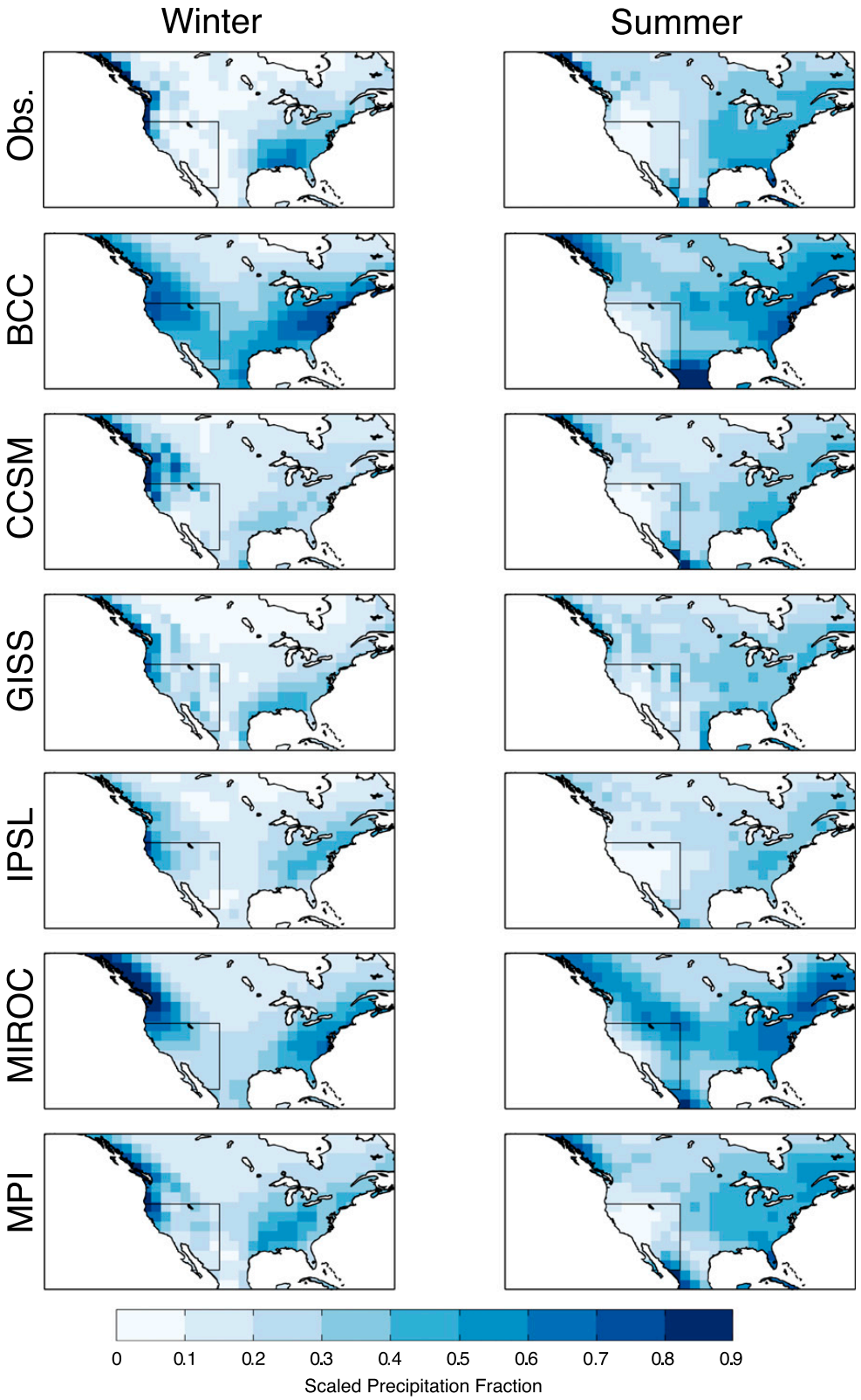

Figure 2.4: Fraction of precipitation at each grid point for the mean winter (NDJFMA) and summer (MJJASO) half years. Each value is additionally scaled by the ratio of the yearly integrated precipitation at that grid point to the largest yearly integrated precipitation of all grid points in the ASW to provide a sense for the contribution of each grid point's half-year integrated precipitation to the yearly integrated ASW spatial average precipitation.

It is important to characterize how these biases may impact the results presented herein. JJA PDSI reflects hydroclimate conditions for the past 12–18 months because of persistence built into the PDSI calculation, and as a consequence, precipitation biases in both seasons will impact PDSI. Nevertheless, tree-ring reconstructed PDSI has been shown to predominately reflect winter season precipitation variability over the ASW region (St. George et al., 2010; Griffin et al., 2013), a characteristic that is likely shared by the models. If this is the case, the impact of underestimating summer precipitation on comparisons between model and reconstructed PDSI may be minimal. Nevertheless, the paleoclimate model-data comparison in Chapter 5 will be limited to determining if models can simulate drought features with similar persistence and severity to megadroughts. The limitations of the paleoclimate record, however, make it unclear if the models are simulating these features for the right reasons (e.g., do reconstructed megadroughts result from winter, summer, or dual-season precipitation shortages?). Nevertheless, Chapter 6 will approach this question using an additional hydroclimate reconstruction from Griffin et al. (2013).

2.6 Modes of Variability

2.6.1 Definitions

The dynamical modes will be defined as listed below, with seasonality determined by the peak season of the impact of that mode of variability on the ASW (see also Figure 2.5). The input data to these calculations will be either the observed data or model output outlined in Sections 2.1.2 and 2.1.3. The methods for calculating any additional modes of atmosphere-ocean variability, principally those not used in Chapter 5 or multiple chapters, will be outlined in chapter specific methods sections (e.g. Chapter 7).

1) JJA AMO (10-year low-pass filtered extratropical North Atlantic minus global SST anomaly following Enfield et al., 2001);

2) DJF PDO (leading empirical orthogonal function (EOF) of monthly SST anomalies poleward of 20°N following Zhang et al., 1997; Mantua et al., 1997);

3) DJF central equatorial Indian Ocean (CEI; SST anomaly over 15°N–0°, 50°–80°E, following Goddard & Graham, 1999);

4) JJA tropical Atlantic Ocean (annually averaged anomaly of Atlantic SSTs from the equator to 20°N); and

5) DJF ENSO — tropical Pacific gradient (TPGR), following Karnauskas et al. (2009), Niño1+2 (average SST anomaly over 10°S–0°, 90°–80°W), Niño3 (average SST anomaly over 5°S–5°N, 150°–90°W), Niño3.4 (average SST anomaly over 5°S–5°N, 170°–120°W), and Niño4 (average SST anomaly over 5°S–5°N, 150°W–160°E).

The tropical Atlantic SST index was chosen based on prior work that shows it to be the equatorial component, as opposed to the extratropical component, of the AMO that influences NA hydroclimate (e.g. Schubert et al., 2004b; Sutton & Hodson, 2005; Kushnir et al., 2010). However, as shown in Ting et al. (2011), models tend to have weak expressions of the AMO in the tropical region.

The use of five different indices of tropical Pacific variability, with centers of action in different regions of the tropical Pacific basin, guards against the possibility that a single ENSO index may not adequately capture ENSO variability across all of the models. The TPGR index is a measure of the difference between SSTs averaged over 5°S–5°N, 150°E–160°W and 5°S–5°N, 130°–80°W, and it reflects the zonal temperature gradient between the western and eastern ends of the equatorial tropical Pacific basin. The Niño1+2, Niño3, Niño3.4, and Niño4 indices, by contrast, reflect the average SST anomaly over a single spatial region in the tropical Pacific.

Our understanding of the above-listed modes of variability and their "drying" (driving

anomalously dry conditions) or "wetting" (driving anomalously wet conditions) impact on the ASW is based on the literature in the "ASW impact" section of Figure 2.5. In each case, the (cool or warm) phase of the mode that drives drying in the ASW will be listed along with the corresponding (positive or negative) orientation of the associated index. These studies variously employ the paleoclimate record, observations, modeling results, physical theory, or some combination thereof to define the ASW hydroclimate state during each phase of the various indices (e.g., a La Niña-like or positive state in the TPGR index is associated with drying in the ASW).

	Index	**Phase**	**Index Sign**	**ASW Impact**
ENSO/Tropical Pacific	TPGR (Karnauskas et al. 2009)	Cool	Positive	Cane and Sarachik (2010)
ENSO/Tropical Pacific	Niño1+2, Niño3, Niño3.4 and Niño4	Cool	Negative	Cane and Sarachik (2010)
AMO	(Enfield et al. 2001)	Warm	Positive	McCabe et al. (2004)
PDO	(Zhang et al. 1997)	Cool	Negative	McCabe et al. (2004)
Equatorial Atlantic	Annually averaged SST anomaly from equator to 20°N in Atlantic	Warm	Positive	Oglesby and Feng (2011)
Global Temperature	Annual and globally averaged temperature	Warm	Positive	Held and Soden (2006); Seager and Vecchi (2010)
Indian Ocean	CEI (Goddard and Graham 1999)	Cool	Negative	Hoerling et al. (2003)

Figure 2.5: Modes of atmosphere-ocean and exogenous variability and the impact of these on the ASW. The "Index" column notes the reference or method for calculating the index for the mode listed in the first column. The "Phase" is that which drives drying in the ASW as concluded by the reference in the "ASW Impact" column. The "Index Sign" is the sign of the index during that phase.

2.6.2 Characteristics

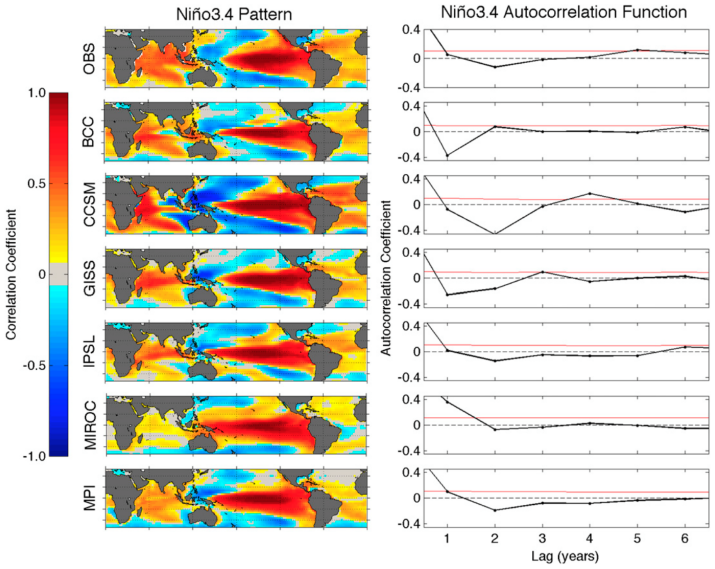

Figure 2.6:]

(left) Correlation between the DJF Niño3.4 index and the DJF SST field for each model and the observed SST dataset. (right) The autocorrelation of the Niño3.4 index for 1–6-year lags is plotted, with the red line indicating significance at the 95% level (2 times the large-lag standard error). The plotted domain is longitudinally global beginning at 0° and spans the latitudes 40°S–40°N.

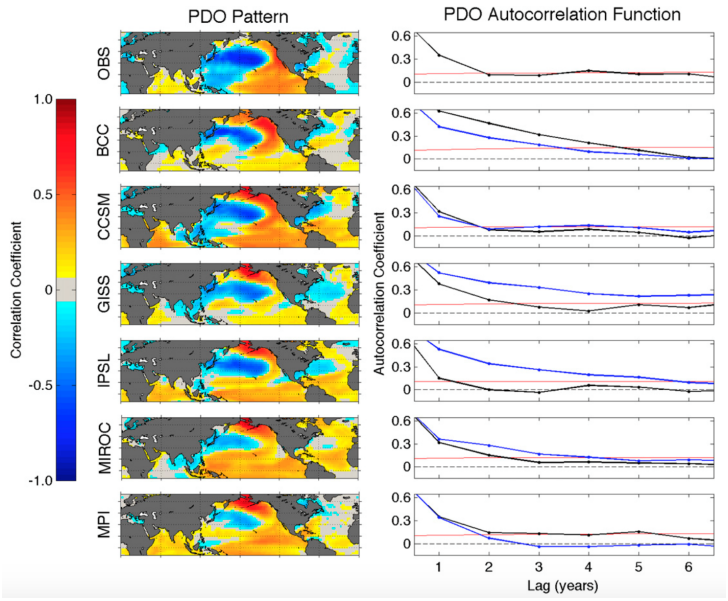

Figure 2.7: (left) The PDO pattern for each model and the observed SST dataset, calculated as the correlation between the DJF PDO index and the DJF SST field. (right) The autocorrelation of the PDO index for 1–6-year lags is plotted with the red line indicating significance at the 95% level (2 times the large-lag standard error). These values are plotted for both the control (black) and forced (blue) simulations from each model. The plotted domain is longitudinally global beginning at 0° and spans the latitudes 20°S–70°N.

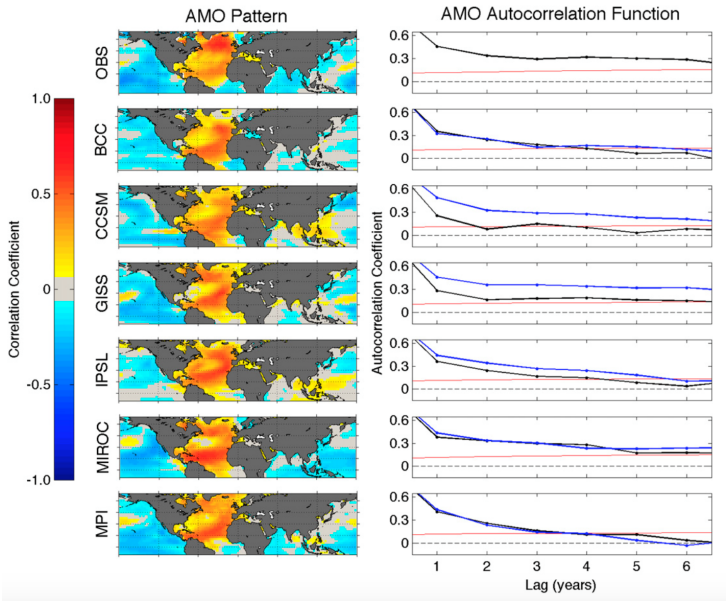

Figure 2.8: (left) Correlation between the JJA AMO index and the JJA SST field for each model and the observed SST dataset. (right) The autocorrelation of the AMO index for 1–6-year lags is plotted with the red line indicating significance at the 95% level (2 times the large-lag standard error). These values are plotted for both the control (black) and forced (blue) simulations from each model. The plotted domain is longitudinally global beginning at 180° and spans the latitudes 20°S–70°N.

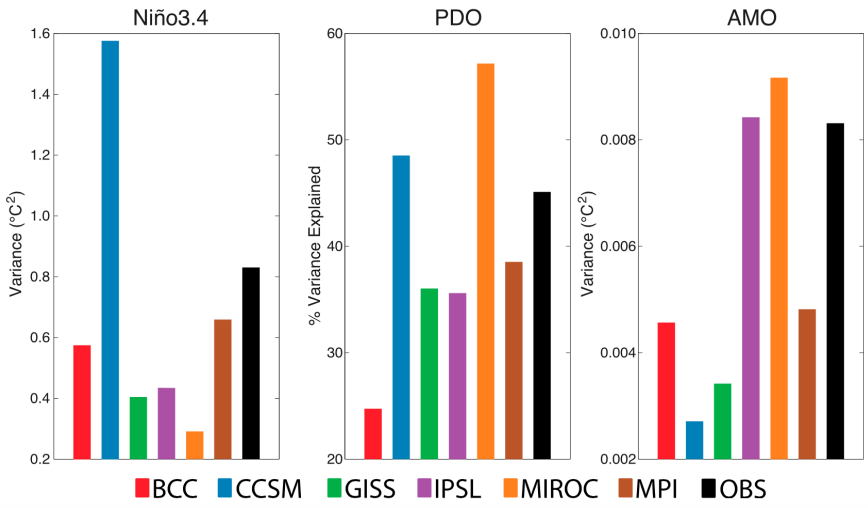

Figure 2.9: The (left) variance of the Niño3.4 index, (middle) percent variance explained in Pacific SSTs by the PDO mode of variability, and (right) variance of the 10-year low-pass-filtered AMO index. These were computed for each full control run and for the observed dataset over the period 1854–2005 C.E.

The ENSO, AMO and PDO are the dominant modes of variability that impact hydroclimate over NA. In this section we provide a brief assessment of the characteristics of these modes in the CMIP5/PMIP3 models and observations. Figures 2.6 through 2.8 show the SST spatial pattern and autocorrelation of the ENSO, PDO, and AMO for the full model simulations and observations. Figure 2.9 additionally shows the variance of, or variance explained by, these dynamic modes. Models are generally successful at simulating a reasonable ENSO spatial pattern, although the SST anomalies extend too far west (Figure 2.6). Additionally, the simulated ENSO autocorrelation structures are largely characteristic of the observations, with oscillatory behavior that varies between negative and positive. This oscillation looks to be most realistic in CCSM, IPSL, and MPI, with a cycle of variability that is too short and regular in BCC and GISS. The magnitude of the ENSO variability is not consistent across the models, with CCSM having too much variance, while GISS, IPSL, and MIROC have too little, as compared to the observations (Figure 2.9). The PDO and AMO patterns in the models are less characteristic of the observed patterns than for ENSO. Additionally, the BCC and GISS models fail at simulating the magnitude of the observed tropical expression of the PDO, with all of the models overestimating the high-latitude North Pacific expression

of the PDO relative to the expression in the tropics. This is critical because the PDO forcing of hydroclimate variability has been shown to originate in the tropical Pacific (Seager et al., 2015).

The persistence characteristics of the PDO and AMO are plotted for both the forced and control simulations in the right-hand panels of Figures 2.7 and 2.8, respectively. While the models have a reasonable PDO autocorrelation structure (BCC and the forced GISS and IPSL simulations, however, each have too much persistence), with the exception of CCSM and GISS they struggle at simulating the AMO with enough persistence (this is consistent with the behavior of the CMIP3 model ensemble in Ting et al., 2011). This lack of persistence suggests that models will have difficulty in simulating the observed drought persistence in regions that are tightly coupled to the AMO in the real world (e.g., the Great Plains and Southeastern United States — Kushnir et al., 2010; McCabe et al., 2004, 2008; Nigam et al., 2011; Ting et al., 2011). Finally, the magnitude of the PDO and AMO will partially determine the impact of these modes of variability, relative to the impact of ENSO and purely atmospheric variability, on NA hydroclimate. There is a large inter-model spread in the variance or variance explained by both modes, with CCSM and MIROC having too much and BCC, GISS, IPSL, and MPI having too little PDO variability compared to observations, and BCC, CCSM, GISS, and MPI having less AMO variability than observed (Figure 2.9).

2.7 Statistical Significance

To test the statistical significance we use an autocorrelation and distribution preserving bootstrapping method (Schreiber & Schmitz, 2000), which first sorts (ranks) a collection of Gaussian-distributed random numbers of the length of the input index (e.g. the modes of atmosphere-ocean variability in Chapter 5). Each input index is likewise sorted (ranked) and the k-th largest value of the index is replaced with the k-th largest Gaussian distributed random number. This modified index is phase randomized to produce 5000 Gaussian distributed surrogate indices. In order to preserve the distribution of the original index, the

k-th largest value of each artificial Gaussian index was then replaced with the k-th largest value of the original index. These new surrogate indices exactly preserve the distribution of the original index while largely preserving the spectral characteristics (there will be a slight whitening of the surrogate spectrum).

Chapter 3

ECHO-G Megadroughts

3.1 Motivation and Questions

Despite the large collection of literature in related areas (e.g. Chapter 1), there are few analyses of megadrought occurrences and characteristics in simulations using CGCMs. Meehl & Hu (2006), hereinafter MH06, use a 1000-year control run from the National Center for Atmospheric Research (NCAR) Parallel Climate Model (PCM) fully coupled CGCM and find drought features of comparable length to proxy-estimated megadroughts that are mechanistically linked to low-frequency variability in tropical Pacific SSTs. Additionally, Hunt (2011) analyzes global multiyear drought and pluvial occurrences in a 10000-year control run of the CSIRO CGCM and finds that persistent hydroclimate features can result from internal climatic variability, with stochastic atmospheric variability playing an important role.

The following study builds on the work of MH06, Hunt (2011), and Herweijer et al. (2007, — see Chapter 1) but differs in that we analyze both a forced transient millennium-length simulation and a 1000-year control run together with 1000 years of proxy-estimated drought conditions. Two principal questions are addressed: 1) is the model capable of producing megadroughts that are characteristic of the paleoclimate record and 2), if so, are

these drought features the result of internal variability or do they have a forced component? As is noted in Chapter 1, answering these questions is fundamental to understanding megadrought dynamics and interpreting simulations of future hydroclimate variability, which are in turn essential for future water supply management, risk assessment and infrastructure development in the ASW.

3.2 Paleoclimate Model-Data Comparison

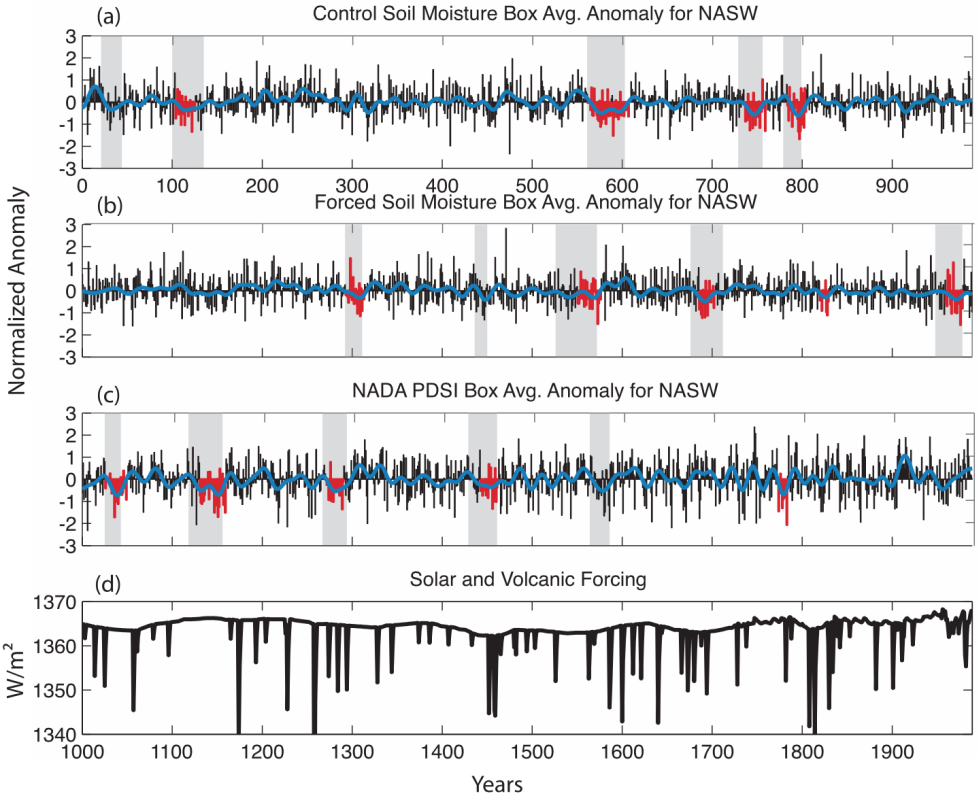

Figure 3.1: Normalized soil moisture anomalies (forced and control model runs) and PDSI (NADA) for the period 1000–1989 C.E. averaged over the ASW region: (a) the control soil moisture index, (b) the forced soil moisture index, and (c) the NADA PDSI index. Annual anomalies (black lines) are shown along with smoothed versions using a 20-year low-pass filter (blue lines). The red highlighted periods in the annual timeseries are the five highest-ranking droughts using the drought identification metric. The gray shaded regions are the five largest droughts determined by the MH06 drought definition. (d) The volcanic and solar forcing timeseries (W/m^2) used in the forced ECHO-G run for comparison to forced and NADA drought timing. Note that the bottom three panels are for the 1000–1989 C.E. period; the timing of the control run in (a) is arbitrary.

There is little or no agreement in timing between droughts in the forced simulation and the NADA PDSI indices (Figure 3.1). There are, however, droughts in both control and forced runs that are characteristic of the proxy estimates. In particular, the three timeseries in Figure 3.1 demonstrate that megadroughts in both model runs are of comparable duration to those of the paleoclimate record. Although the model exhibits more positive excursions during a given drought period in some cases, the average length of the five highest-ranking forced and control-run droughts is approximately equal to that of the NADA estimates (19, 22, and 21 years, respectively).

The presence of droughts in the control run that are comparable in length and severity to the forced run suggests that internal climate variability can cause megadroughts in the model. Although it is unclear if observed megadroughts are the result of radiative forcing, overlap between the forced model and proxy-estimated drought timeseries would be expected if the reconstructed forcing used to drive the model is realistic and the modeled megadroughts are a forced response. This is not the case. For instance, the low-pass correlation between the forced drought index and NADA PDSI index (0.023) is not significantly different from the range of low-pass correlations between the forced drought index and 1000 red noise series with the same persistence as the NADA PDSI index (r=-0.014 and r=0.075 are the 25th and 75th percentiles, respectively). Furthermore, the control drought index is just as temporally synchronous with the NADA record as the forced drought index, also indicating that any overlap between the historical droughts and those in the forced run occur by chance. Finally, a direct comparison to the forcing timeseries can be made in Figure 3.1, which indicates that modeled megadroughts do not have a preferred forcing state. For instance, the 1800s model drought occurs during a period of relatively low solar forcing and high volcanic activity while the 1300s and 1500s model droughts are contemporaneous with relatively high solar forcing and low volcanic activity. These results provide evidence that low-frequency ASW hydroclimate variability in the ECHO-G simulations is not solely a response to radiative forcing changes.

As a further line of inquiry, the number of droughts greater than a threshold length are plotted in Figure 3.2. The model produces more droughts in each threshold length than the NADA record, but the number of droughts in the model and NADA fall within a narrow range. Also in Figure 3.2, the droughts in each dataset are compared to those of 1000 first-order autoregressive (AR1) red-noise timeseries with the same characteristics as the corresponding model or observation (i.e., AR1 coefficient, variance, and mean). Historical and modeled droughts are more prevalent than those in the red-noise timeseries for longer timescales (greater than the 90th percentile for all three datasets for droughts of 15+ and 20+ years) but not for the 10-year threshold (Figure 3.2). This latter observation is not surprising as noise series with some persistence should be capable of producing periods of persistent negative anomalies. The greater drought persistence in the observed and modeled data for longer timescales nev-ertheless indicates that there are likely mechanisms creating persistence beyond first-order autoregressive variations that are responsible for megadrought occurrences. Interestingly, the box plots indicate that there is more persistent drought in the control simulation than in the forced simulation. A comparison of the spectra of the control and forced drought indices (Figure 3.2) suggests that the control run does in fact exhibit more power in the decadal-to-multidecadal range.

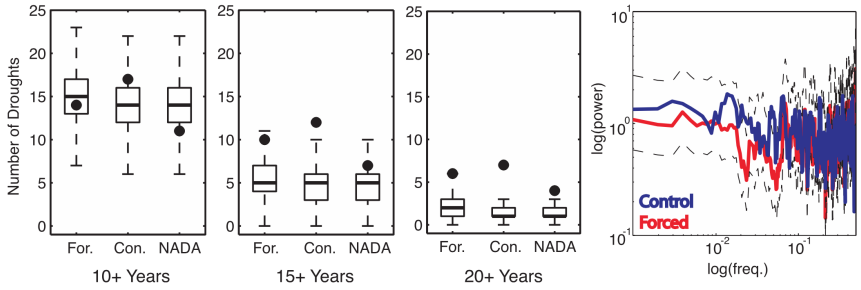

Figure 3.2: The black dots are the number of droughts in the ASW region in the forced (For) and control (Con) simulations and the NADA that are at least (from left to right) 10, 15, or 20 years in duration. Box plots are determined from 1000 AR1 red-noise timeseries with the same AR1 coefficient, variance, and mean as the corresponding model or NADA indices (middle bar is the median, top and bottom bars are the 75th and 25th percentiles, and the whiskers are the full data range). (far right) The spectra using the multitaper method (Mann & Lees, 1996) for the forced (red) and control (blue) soil moisture indices with dashed lines for the 5th and 95th percentile confidence intervals of the forced multitaper spectrum.

3.3 Drought Spatial Patterns and Teleconnections

To investigate the influence of the tropical Pacific on drought variability in the ASW, we calculate the correlation of the yearly SST field with the ASW drought index: the former was averaged from May to April, and for the model output the latter was averaged from October to September to reflect a lag between the ENSO-driven precipitation anomaly and the soil moisture anomaly (the NADA PDSI is JJA average). These calculations were performed for the full period in the two model simulations and the 133-year time overlap between the NADA and Kaplan SST datasets (1857–1989 C.E.). Three analyses were completed: one with raw data, one with 10-year low-pass filtered data, and one with high-pass filtered data (separated using a 10-point Butterworth filter). Results are shown in Figure 3.3.

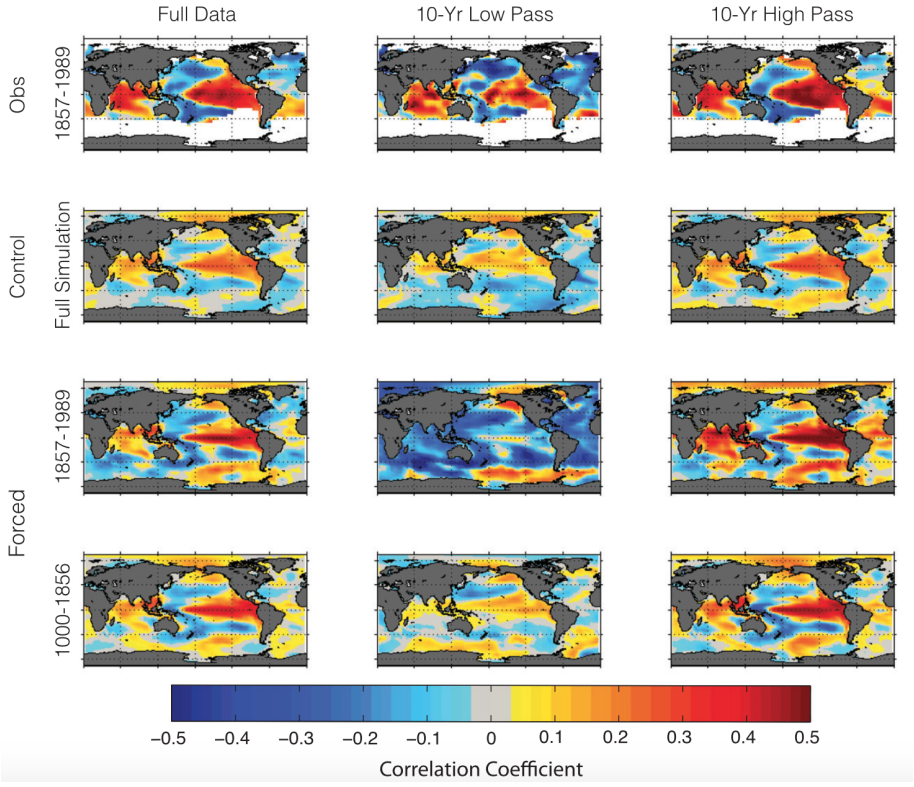

Figure 3.3: Correlation coefficient maps between soil moisture (models) or PDSI (NADA) ASW indices and SST fields. (from top to bottom) The correlation of the overlapping period of the NADA with the Kaplan SST dataset, the full control simulation, the forced simulation for the modern period (1857–1989 C.E.), and the forced simulation for the period 1000–1856 C.E. (left) The full unprocessed data, (middle) the 10-year low-pass filtered data, and (right) the 10-year high-pass filtered data.

The ASW region has a weaker connection to the tropical Pacific in the annual and high pass correlations for both the forced and control runs than in the observational data. Despite the discrepancy, the model index is still highly correlated with the tropical Pacific Ocean. Furthermore, it captures the major spatial features of the observed correlation map, indicating that the model contains realistic though weaker teleconnections.

The low-pass correlation map is relevant for the purpose of understanding what drives multidecadal drought variability. For the observations, the connection of ASW PDSI to the tropical Pacific is only slightly lower for low-frequency variations as compared to high-frequency variations. In the model simulations the control run maintains a connection to the tropical Pacific Ocean when low-pass filtered data are used (similar to MH06). The forced run, on the other hand, does not maintain this connection; this results from a strong positive trend in eastern Pacific SSTs in the modern period (1870–1989 C.E.) that coincides with a slightly negative trend in the forced soil moisture index and washes out the phase connection between the two fields. With the modern period removed there is a moderately positive correlation for low frequencies in the tropical Pacific Ocean, but still much weaker than the observational record (the average correlation between ASW soil moisture and Niño3 SSTs is 0.16 in the forced run versus 0.36 for the paleo-observed record). The frequency-dependent relationships are further illustrated in Figure 3.4 in which the wavelet coherence of the ASW box average NADA PDSI and the Niño3 index is shown for the full 133 years of the instrumental period. Shown below the instrumental plot are wavelet coherence spectra between three randomly selected 133-year segments of soil moisture and the corresponding Niño3 SST indices from the ECHO-G control run. As was seen in the correlation fields, the model clearly exhibits much less coherence in the decadal time range than the observations. Note that the low-pass filtered observations also show a relationship between positive PDSI and cool Atlantic Ocean SSTs. Like the tropical Pacific correlations, this is much weaker in the model (Figure 3.3).

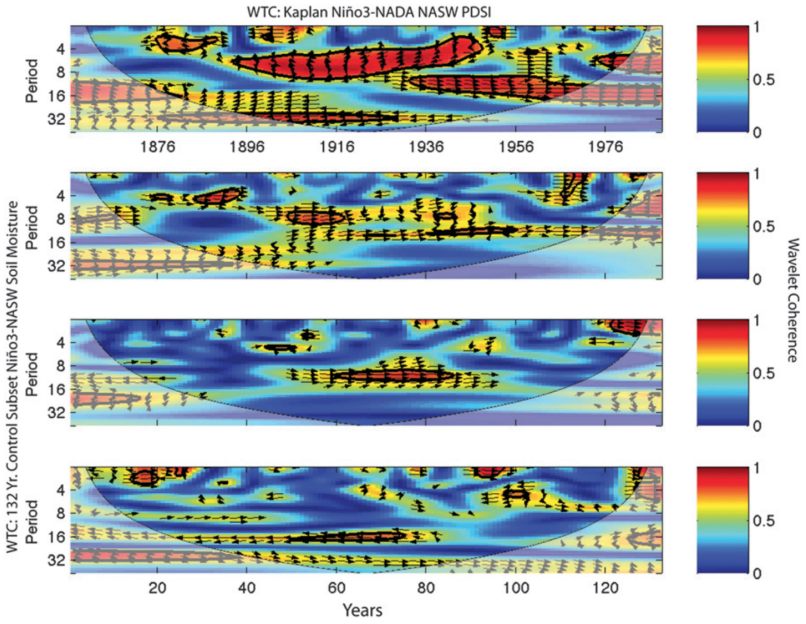

Figure 3.4: (top) Wavelet coherence of ASW box average PDSI from the NADA with Niño3 box average SSTs over the common period 1857–1989 C.E. (lower panels) Coherence of ASW average soil moisture and Niño3 SSTs for three random 133-year subsets of the control run. The arrows show the phasing direction, the colored contours show the magnitude of the coherence, and the black outline shows significance at the 95% level. Shaded regions are outside the significance windows. Note the higher coherence in the decadal range for the observed/proxy data in the top panel.

3.4 Dynamical Diagnostics

Not surprisingly, given the climatology of the ASW, negative December–February average (DJF) precipitation anomalies are the dominant cause of the annual soil moisture signal during ASW droughts. Figure 3.5 shows maps of the DJF precipitation anomalies during each of the five highest-ranking droughts in the forced and control simulations, as well as composites over all of these droughts. The spatial features are consistent within each of the droughts and between the forced and control simulations, with a positive precipitation anomaly in the Northwest (for all but the 784–804 drought in the control simulation) while the ASW is anomalously dry. This structure is reminiscent of a La Niña winter moisture anomaly resulting from a northward shift of the storm track (e.g. Sarachick & Cane, 2010).

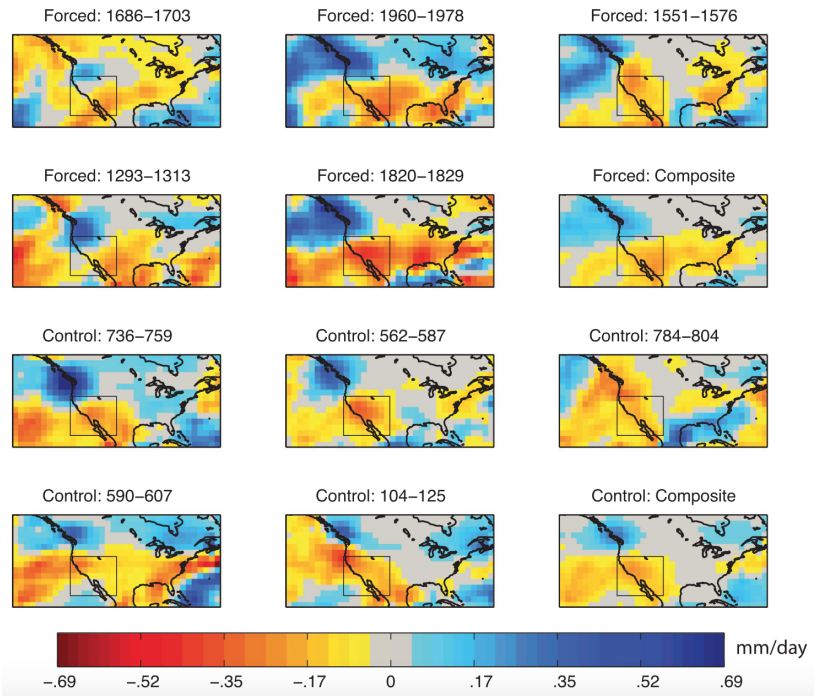

Figure 3.5: Average DJF precipitation anomalies (mm/day) for the five highest-ranking droughts. Time-weighted composite averages for the forced and control simulations are also shown. Blue indicates above average precipitation and red below average precipitation. The square box is the ASW region.

Figure 3.6 shows the forced and control TPGR index with the five highest-ranking drought periods identified in the corresponding ASW index highlighted in red. Considering the evidence for synchronous phasing between La Niña states and negative ASW soil moisture periods on both interannual and decadal timescales (in observations) one might expect the drought periods to be coincident with the largest positive excursions in the TPGR index (the most La Niña-like states). This is not the case, however, and the state of the tropical Pacific does not appear to have a consistent and strong control over simulated low-frequency drought periods in the ASW (only the late 13th- and 20th-century forced droughts and the late 6th-century control drought correspond to persistent La Niña states). Low-frequency ENSO variability is, therefore, not the only mechanism driving persistent moisture anomalies in the ASW in the ECHO-G model.

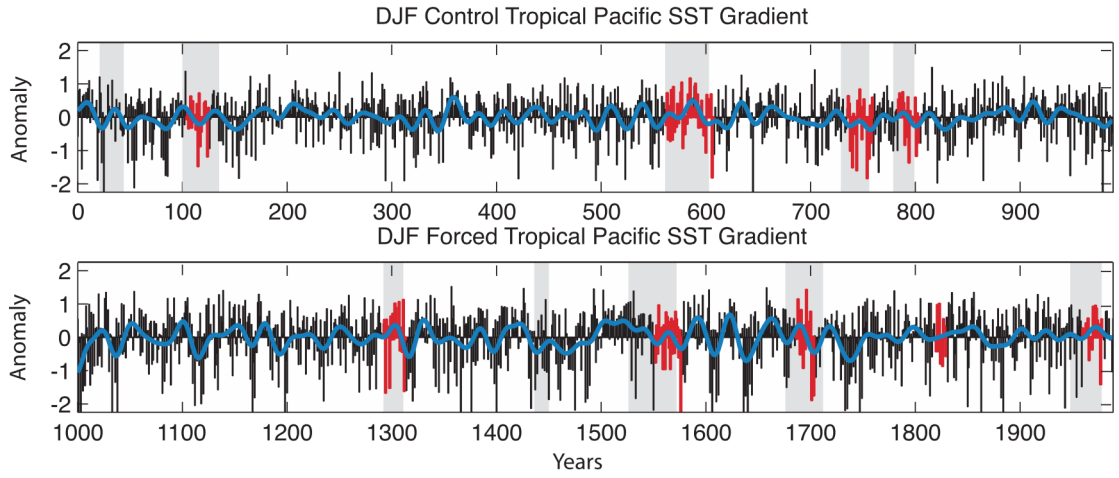

Figure 3.6: TPGR (°C) for the forced and control runs. The five highest-ranking drought periods as determined from the ASW soil moisture index and either the drought identification metric or MH06 definitions are highlighted in red or gray shading, respectively.

Analysis of both the PDO and the AMO suggests that these oscillations also exert a similarly weak influence on modeled ASW hydroclimate (both were analyzed as in Figure 3.6). Furthermore, there is very little consistency outside of the ASW region in the seasonal and annual mean model fields of temperature and evaporation during drought periods. By contrast, the winter half-year average [November–April (NDJFMA)] SLP field shows a high pressure anomaly over the North Pacific during nearly all of the megadroughts (Figure 3.7). This is consistent with a northward shift of the storm track. For the forced simulation, the hemispherically symmetric SLP anomaly in the composite is reminiscent of La Niña, but the individual droughts tend not to exhibit characteristic ENSO-driven SLP symmetry. In the control run, the composite and individual drought patterns are even less characteristic of ENSO variability, suggesting that stochastic NH atmospheric variability can drive persistent ASW drought in the model. The Arctic Oscillation (AO), defined as the leading mode of the monthly mean wintertime SLP following Thompson & Wallace (1998), is more tightly coupled to both the forced and control soil moisture indices than the ENSO, PDO, or AMO (not shown), nevertheless the correlation is still weak (correlation coefficients of -0.21 and -0.14 for the forced and control runs, respectively). It is therefore likely that the stochastic variability associated with the simulated decadal-length droughts in the ASW is the result of numerous atmospheric modes that are not readily described using a single atmospheric

index. Given the very consistent spatial structure of the precipitation anomalies and the above characterization of SLP anomalies, our collective analysis suggests that stochastic atmospheric variability can produce persistent northward shifts of the storm track in ECHO-G, similar to those seen during La Niña events, and thus drive megadrought occurrences in the model.

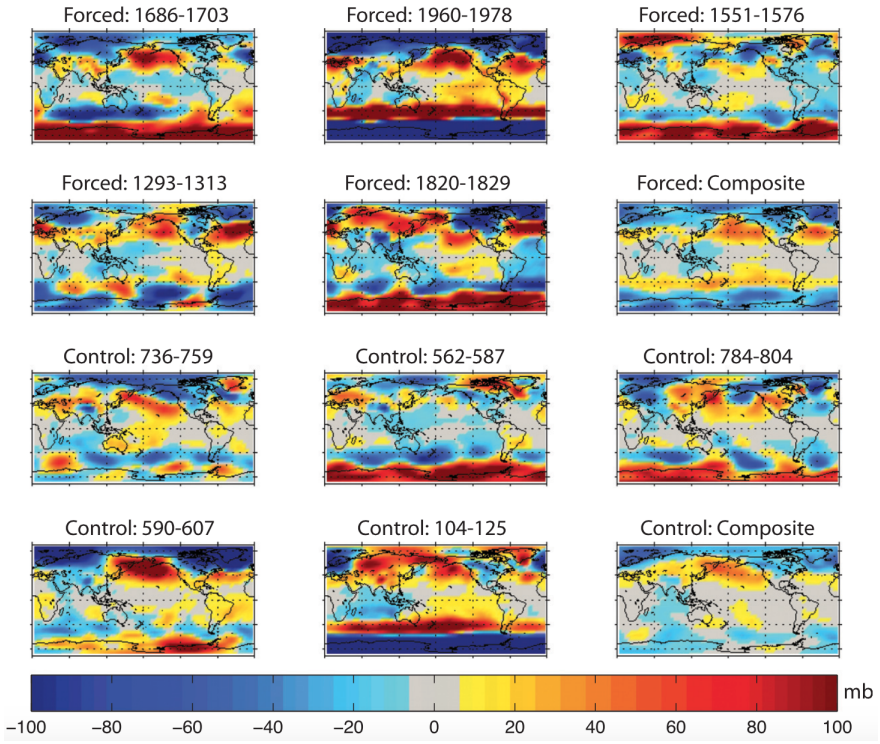

Figure 3.7: Winter (November–April) SLP anomalies (mb) for each of five highest-ranking droughts using the drought identification metric and the composites over all the drought years for the forced and control runs.

3.5 Conclusions

Megadroughts in the ASW, in forced and control simulations using the ECHO-G CGCM, are similar in duration and magnitude to those seen in the paleoclimate record. The droughts in the forced simulation are not, however, temporally synchronous with those in the proxy record or the forcing timeseries, nor are there significant differences between the drought features simulated in the forced and the control runs. This indicates that

model-simulated megadroughts can result from internal variability of the modeled climate system, rather than as a response to changes in exogenous forcings. The frequency and persistence of megadroughts in the model and NADA suggests that mechanisms beyond first-order autoregressive variability are producing these drought features. Although the ECHO-G CGCM is capable of simulating megadroughts through a persistent anomalous SST forcing in the tropical Pacific (e.g., the late 6th-century drought in the control run and the late 13th-century drought in the forced run), other mechanisms can produce similarly extreme moisture anomalies in the ASW in the model. In particular, the lack of low-frequency coherence between ASW soil moisture and other modeled fields and the PDO, AMO, and AO indices during identified drought periods suggests that stochastic atmospheric variability can contribute significantly to the occurrence of simulated megadroughts in the ASW. These results, while limited to a single model, demonstrate the importance of analyzing both forced and control simulations in concert with the paleoclimate record. Stochastic variability has been shown to drive drought in models on interannual-to-decadal timescales, particularly in weakly teleconnected regions by Hunt (2011). In this instance, it seems plausible that stochastic atmospheric variability in the ECHO-G model can produce storm track shifts (and associated hydroclimatic changes like ASW drought) that are uninterrupted by tropical Pacific influence because of the weak, or potentially non-stationary, NASW-ENSO teleconnection on multidecadal timescales.

In the observational record, persistent droughts in the ASW have all been tied to cool SSTs in the tropical Pacific Ocean (e.g. Seager et al., 2005b; Herweijer et al., 2006), but it is not known if this relation holds for the entire last millennium. Consequently, these model results have two implications depending on whether the modeled hydroclimate variability is a reasonable representation of the actual climate system: 1) if the model is accurately simulating real-world variability, then stochastic atmospheric variability and ENSO both appear capable of producing persistent droughts in the ASW or 2), if the model is misrepresenting the actual variability, then this feature is a likely component of CGCMs that will influence fu-

ture projections of hydroclimate, an inaccuracy that must be addressed when assessing model projections. One possible explanation for point two is that a weak teleconnection between the ASW and the tropical Pacific Ocean in the model allows atmospheric variability to drive droughts, whereas the tighter link to the Pacific in nature ensures that megadroughts are more strongly forced by tropical Pacific SST anomalies. Additionally, there is observational evidence that warm tropical Atlantic SSTs can create a tendency toward dry conditions in the ASW (Seager et al., 2008b; Kushnir et al., 2010; Nigam et al., 2011) and this has been appealed to as a cause of MCA megadroughts (Feng et al., 2008; Oglesby et al., 2012). The connection of the ASW drought index in the model to the Atlantic is weaker than observed and this too could allow atmospheric variability to exert a stronger relative influence on ASW hydroclimate.

Longer records of proxy-estimated tropical Pacific SST (e.g. Emile-Geay et al., 2013, and Chapter 7) are necessary to assess the state of ENSO during megadroughts and to determine how coherent ASW drought and ENSO variability may have been prior to the observational record. In the meantime, additional analyses of CGCM simulations will identify what produces model-simulated megadroughts and help evaluate model treatment of regional low-frequency hydroclimate variability. In particular, multiple CMIP5/PMIP3 LM, control and historical simulations will be employed in Chapter 4 to analyze the strength and stationarity of the tropical Pacific teleconnection to the ASW in state-of-the-art models. This will provide a point of comparison to the teleconnection characteristics in the ECHO-G model, which we have suggested are important to the simulation of megadroughts. Likewise, a multi-model intercomparison employing the CMIP5/PMIP3 CGCMs is completed in Chapter 5 to determine if stochastic atmospheric variability similarly influences ASW megadrought occurrences in the most recent generation of CGCMs.

Chapter 4

Teleconnection Stationarity

4.1 Motivation and Questions

The tropical Pacific Ocean impacts regional hydroclimate variability in the extratropics by means of wave propagation from areas of persistent precipitation and divergence anomalies that are in turn forced by SST variations (e.g. Sarachick & Cane, 2010). The preferred circulation responses to tropical Pacific SST forcing are called atmospheric teleconnections and depend on a Rossby wave response (see Trenberth et al., 1998, for a review) and subsequent interaction between the mean flow anomaly and transient eddies (Hoerling & Ting, 1994; Seager et al., 2003, 2010; Harnik et al., 2010). A quintessential feature of the ENSO teleconnection is the Pacific jet stream shift over the western coast of NA, which a wealth of research has implicated as an important forcing of hydroclimate variability in the ASW. Critically, it was the character of this teleconnection that was invoked to explain the megadrought dynamics in the ECHO-G model. It is thus necessary to better understand the range of simulated teleconnection behavior. Toward such ends, the CMIP5/PMIP3 archive provides a state-of-the-art ensemble of model simulations for evaluating and testing teleconnections over multiple timescales.

The basis of our understanding of atmospheric teleconnections, between ENSO and

NA or otherwise, is derived from the temporally limited observational record and associated reanalysis products (Trenberth et al., 1998). Even within the short observational record, there is evidence that teleconnection patterns can vary considerably in space and time (e.g. Hu & Feng, 2001; Rajagopalan et al., 2000; Cole & Cook, 1998; Gershunov & Barnett, 1998). A full characterization of teleconnection patterns and their stationarity on decadal-to-centennial timescales, however, is not possible using only reanalysis and observational data because of their limited temporal extent. These limitations necessitate the use of alternative approaches to further characterize and understand teleconnection stationarity. Herein, we analyze three ensembles of CCGMs from the CMIP5/PMIP3 archive and compare them to the NCEP-NCAR reanalysis project 1 (Kalnay et al., 1996) to assess the stationarity of the modeled ENSO-NA teleconnection.

4.2 20th-Century Teleconnection Variability

The analyzed model fields are surface temperature and 200 mb geopotential height. The latter was chosen over precipitation because it comprises a more spatially and temporally homogeneous representation of the NA teleconnection, and because it is the ultimate driver of the precipitation variability. For both fields, the climatology (calculated over the full simulations and the full length of the reanalysis) has been removed and the December–February (DJF) anomalies averaged. Winter averages were chosen because winter is the dominant period of precipitation forcing by ENSO in the ASW (Trenberth et al., 1998).

The teleconnection is defined by the grid point correlation between the DJF average 200 mb geopotential height fields and the DJF average Niño3.4 SST index. The resulting correlation field indicates both the teleconnection strength and its spatial features. As an estimate of the observed teleconnection pattern, the correlation field was calculated for two periods in the NCEP-NCAR reanalysis: 1949–2005 C.E. (the overlapping period with the historical runs) and 1979–2005 C.E. (the overlapping period with the AMIP runs). To assess

the modeled teleconnection over NA, the centered pattern correlation statistic (hereinafter CPCS — following Santer et al., 1995) was calculated between these reanalysis teleconnection patterns and the teleconnection patterns from the models over the NA region (160°W–50°W, 70°N–20°N). The CPCS is equivalent to a Pearson's product-moment linear correlation between spatial values (Santer et al., 1995).

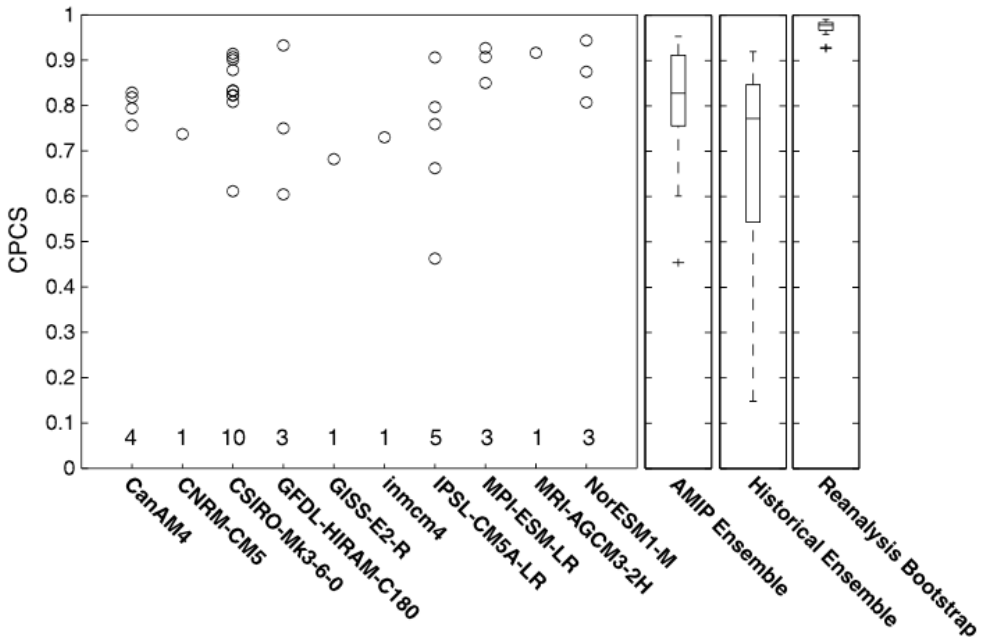

Figure 4.1: Teleconnection stationarity, as measured by the CPCS over NA, using teleconnection patterns estimated from the NCEP-NCAR reanalysis (see Figure 4.2) and the AMIP simulations. The first panel on the left is the CPCS value for each AMIP simulation. The second panel from the left plots the CPCS range for all 32 AMIP simulations. The third panel is the CPCS range for the 1979–2005 C.E. period in the 16 coupled historical runs. The last panel on the right is the CPCS range for the reanalysis bootstrap experiment. Box plots represent the 25th and 75th percentiles of the data with the median as the central line and the whiskers showing the full data range excluding outliers; outliers are marked with a cross. The number of ensemble members from each AMIP model are the inset values.

Figure 4.1 characterizes the teleconnection variability across the collection of AMIP models and within the individual model ensembles. For each AMIP ensemble member, a teleconnection pattern was calculated and compared to the 27-year period from the reanalysis using the CPCS. Because each simulation is forced with the same observed SSTs, the range in CPCS within each AMIP model ensemble represents an estimate of the impact of

internal atmospheric variability on the circulation over NA. The calculated range was subsequently compared to the CPCS range from the same period in the historical runs, which have coupled SSTs, and thus different SST variability and patterns. When all of the AMIP simulations are considered (32 in total), the CPCS range (excluding outliers) is about 0.35 (Figure 4.1). This is less than half the range over the same period (1979–2005 C.E.) in the coupled historical runs with dynamically evolving SSTs (Figure 4.1). Atmospheric noise (or internal atmospheric variability), therefore, cannot be considered the dominant driver of differences between modeled teleconnections over NA in the collection of model simulations, and the relative differences in the range of the CPCS statistic are interpreted as arising from the SST-induced variations on the teleconnection over NA in the coupled simulations.

To evaluate the temporal stationarity of the observed teleconnection in the reanalysis data over a 27-year window, a bootstrap resampling of CPCS values in continuous 27-year segments was computed over the 56-year reanalysis record. The range in CPCS for 1000 of these resampled segments against the 1979–2005 C.E. reanalysis target is also plotted in Figure 4.1. The narrow range indicates that the character of the reanalysis teleconnection in the 27-year overlapping period between the AMIP and historical simulations well represents the full 56-year period of the reanalysis.

4.3 Multidecadal Teleconnection Variability

To investigate the nature of teleconnection stationarity, the control and LM runs were divided into 56-year segments to match the length of the NCEP-NCAR reanalysis record, generating a time-slice ensemble of 17 members for each LM run and eight members for each control run. For each segment, the correlation between the Niño3.4 index and the 200 mb geopotential height field was calculated and compared to the 56-year (1949–2005 C.E.) pattern from the reanalysis, again using the CPCS. The range in the CPCS is thus interpreted as a measure of the temporal stationarity of the teleconnection within a given model.

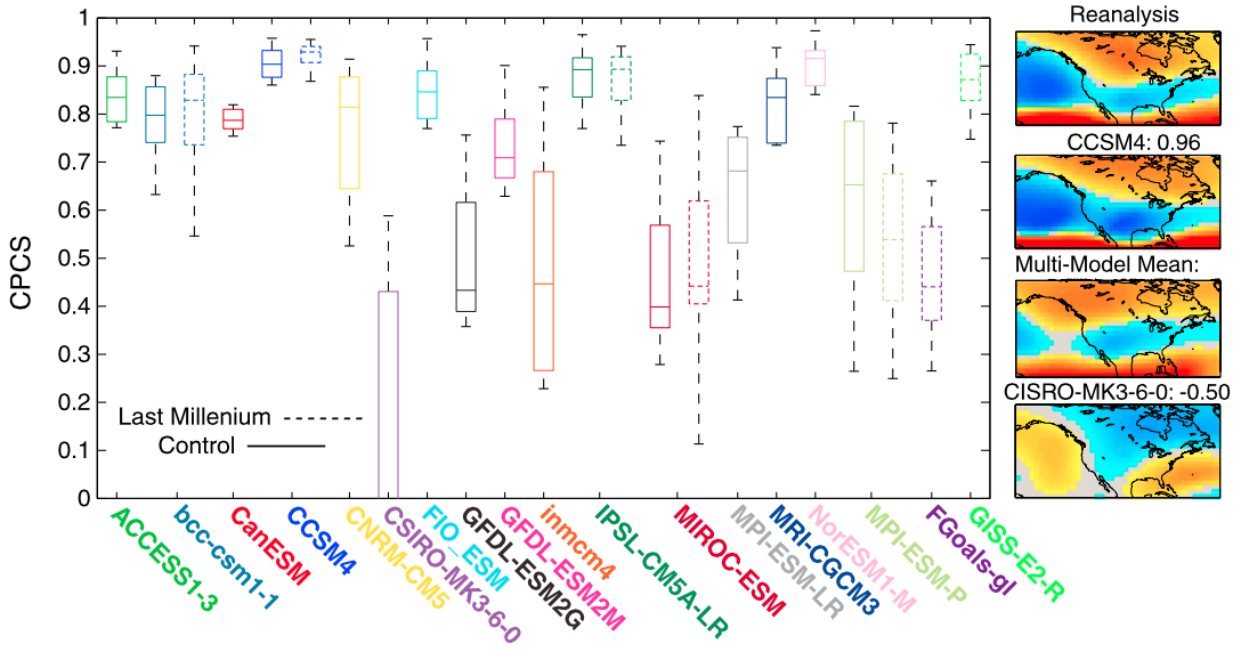

Figure 4.2: Teleconnection stationarity, as measured by the CPCS over NA, using teleconnection patterns estimated from the NCEP-NCAR reanalysis and nonoverlapping 56-year segments from the 500-year control (solid boxes) and 1000-year forced LM runs (dashed boxes). Box plots indicate the 75th and 25th percentile of the CPCS statistic across the segments in the respective coupled model runs with the median as the central line and the whiskers showing the full data range excluding outliers. The right four panels are the teleconnection pattern over 160°W–50°W, 70°N–20°N for the (first panel) reanalysis, (second and fourth panels) the most and least realistic segments, respectively, and the (third panel) model ensemble average. The colorbar range is -1 (blue) to +1 (red). LM ranges have been included as per their availability in the PMIP3 archive. Only models with 500-year control simulations were included, as a consequence, the GISS-E2-R and F-Goals models only have a LM simulation.

The range of CPCS for the 16 control and seven LM runs is shown in Figure 4.2 and indicates a wide range in the teleconnection character within and between models. The models that have a stationary teleconnection (small range in CPCS values) in the control runs possess a similarly stationary teleconnection in the corresponding LM runs (e.g., CCSM). The converse is also true (e.g., MIROC and MPI). Transient forcing characteristics therefore do not appear to significantly impact the simulated teleconnection stationarity.

There is considerable spread in the CPCS range between models. For instance, CCSM simulates a stationary teleconnection that is consistently comparable to the reanalysis data.

CanESM is likewise stationary but less consistent with the reanalysis pattern, while the teleconnection simulated by the CSIRO model is neither stationary nor consistent with the reanalysis pattern. These observations are not explained by model resolution: while the CCSM model has the highest resolution of the simulations (0.9° by 1.3°), CanESM is relatively low resolution (2.8° by 2.8°) and CSIRO is in between (1.9° by 1.9°). We therefore investigate below the potential dynamical links between variability in tropical Pacific SSTs and changing teleconnection characteristics over NA.

4.4 Dynamical Influences on Temporal Teleconnection Variability

What might cause the teleconnection over NA to be nonstationary? The dynamics of teleconnection variability within the models are not fully explored herein, but our analysis suggests that a significant role is played by both the strength and spatial features of the SST anomalies in the tropical Pacific Ocean.

We use the Center of Heat Index (CHI — Giese & Ray, 2011) as a measure of the strength and location of SST anomalies in the tropical Pacific. The CHI statistic is analogous to the first moment of the SST anomaly field and provides both an amplitude and mean longitude for each ENSO event. Panels A and B of Figure 4.3 plot average CHI amplitudes for each 56-year segment from the 16 control runs against the CPCS over NA during the same segment to assess the impact of the magnitude of ENSO events on the teleconnection. Segments with larger El Niño and La Niña events have higher values of the CPCS, although the connection is weak. The same analysis was completed for CHI longitude and a weak relationship between eastward CHI longitude and high values of CPCS over NA was found.

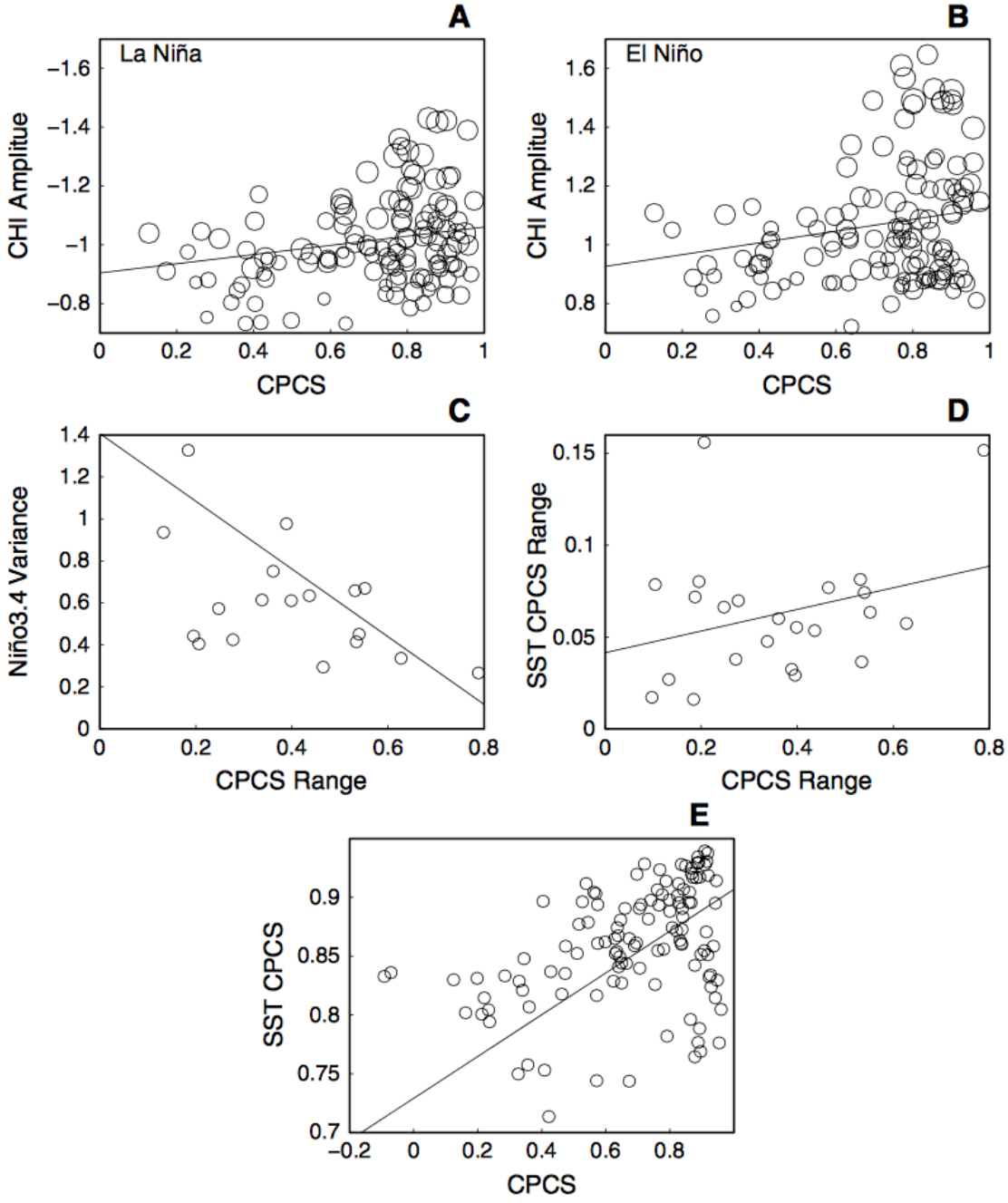

Figure 4.3: Average CHI amplitude for (A) La Niñas and (B) El Niños in each 56-year segment plotted against the CPCS for that segment in the model control runs. The circle radius is proportional to the number of ENSO events in each segment. (C) The variance of the Niño3.4 index for the full control and LM simulations against the range in CPCS for that model simulation. (D) The range in the CPCS of the first EOF of tropical Pacific SSTs for the time-slice ensemble against the teleconnection CPCS range. (E) The CPCS of the first EOF of tropical Pacific SSTs from the top eight segments of each control run (see Section 4.4 for ranking criteria) with that from the NCEP-NCAR reanalysis plotted against the CPCS of the NA teleconnection for that segment. The lines on each panel are the linear regression lines calculated using ordinary least squares.

Panel C of Figure 4.3 investigates the impact of a model's tropical Pacific SST variability on teleconnection stationarity by plotting the average variance of the Niño3.4 index for each time-slice ensemble against the range in the CPCS. There is a significant positive relationship between the ENSO amplitude and teleconnection stationarity, suggesting that large tropical Pacific SST variability allows the associated teleconnection to emerge above noise from secondary patterns of variability.

To determine the impact of the stationarity of the modeled ENSO spatial patterns on teleconnection stationarity, we compute the first empirical orthogonal function (EOF) of the DJF tropical Pacific SST anomaly (defined as 120°E–60°W, 30°N–30°S) for each segment of the control and LM simulations and compare them, using the CPCS statistic, to the same field from the reanalysis. This EOF was determined to be representative of ENSO by a strong correlation (average Pearson's correlation coefficient of 0.96 for all control and LM segments) between its principal component time series and the Niño3.4 index. In Panel D of Figure 4.3, the range in the CPCS between the model and reanalysis EOFs is compared to teleconnection stationarity to determine if models with large multidecadal variability in the spatial expression of ENSO have nonstationary teleconnections. There is a weak positive relationship, indicating that temporal changes in the spatial character of ENSO exert a limited control on the stationarity of the NA teleconnection.

To further characterize the spatial nature of modeled ENSO, the first EOF of the DJF tropical Pacific SST anomaly was calculated for each control run using a 56-year sliding window (incremented by 1 year, thus including overlap) and compared, using the CPCS statistic, to the same field from the reanalysis. The top eight segments for each simulation, as determined by the largest variance explained by the first mode of tropical ocean variability, were subsequently chosen for analysis. This method of segment identification was done in order to maximize the ENSO-forced extratropical atmospheric signal, using the rationale that segments with a dominant first mode of tropical Pacific Ocean variability will contain less "noise" from secondary patterns in the tropical Pacific Ocean. Additionally, there is a

0.86 correlation between the variance of the Niño3.4 index and the percent variance explained by the first EOF across all models, thus the identified segments will also have the largest ENSO amplitude. The results are plotted in Panel E of Figure 4.3 and indicate that the modeled and observed teleconnection will compare well when both strong ENSO variability exists and when the model's ENSO spatial features match those of the reanalysis.

The statistical significance of the relationships in Figure 4.3 is investigated using Pearson's correlation coefficients. Despite our use of this metric for a quantitative description of the variable associations, there is no reason to assume that the functional form is linear or that the relationship can be fully captured given the small sample size. While there is clearly a relationship between temporal and spatial changes in ENSO and the NA teleconnection, the correlations are weak (R^2 values of 0.07, 0.06, 0.34, 0.10, and 0.40 for Panels A through E of Figure 3.3). This is not surprising given other sources of atmosphere-ocean variability. Nevertheless, the correlation in Panel E of Figure 3.3, our best attempt to isolate the signal of the ENSO spatial pattern and amplitude, indicates a moderate and statistically significant relationship (R^2 of 0.40).

4.5 Conclusions

The similarity of the ENSO-NA teleconnection between coupled model simulations and the observational record over the historical interval is an often used metric of model fidelity in reproducing coupled ocean-atmosphere dynamics (e.g. Joseph & Nigam, 2006; Smith & Chandler, 2010; Polade et al., 2013). We nevertheless have shown that many models exhibit considerable variability in their teleconnection strength and character during different 56-year windows of continuous simulations. These results suggest that analyses of teleconnection fidelity should be limited to atmosphere-only simulations forced with observed SSTs (e.g. Langenbrunner & Neelin, 2013). Furthermore, considerable variability in modeled ENSO on multidecadal timescales has been reported in the literature (e.g. Wittenberg, 2009;

Karnauskas et al., 2012; Ogata et al., 2013). If such modeled behavior is dynamically realistic and drives changes in the atmospheric teleconnections, the 56-year reanalysis period may not be sufficient for adequately representing the character of the teleconnection over long timescales. In particular, the impact of nonstationary teleconnections on regional precipitation variability must be better understood, particularly given the range of reconstruction (e.g. MacDonald & Case, 2005; D'Arrigo et al., 2005) and forecasting efforts (see Barnston et al., 2010, for a review of seasonal forecasting efforts) that rely on the stationarity of the observed teleconnection.

Our conclusions also have important implications for efforts to explain the hydroclimate history of the ASW and its links to tropical Pacific climate variations. The analyses in Chapter 3, for instance, suggest that the multidecadal character of ENSO teleconnections can explain the megadrought dynamics in the ECHO-G model. While this is only a single model, if true, the range of multidecadal teleconnection characteristics outlined herein suggest that the CMIP5/PMIP3 models may exhibit a range of megadrought dynamics — principally the modes of atmsophere-ocean variability that underly these features. An analysis of these models and their megadrought dynamics follows in Chapter 5. If teleconnection nonstationarity is a feature of the actual climate system it would undermine reconstruction efforts that make use of teleconnection patterns or regularization that trains on the instrumental interval, including our own climate analogous framework completed in Chapter 7. In particular, this would have consequences for the hypothesis, based on observed teleconnection patterns, that past megadroughts imply a La Niña-like state of the tropical Pacific Ocean.

Chapter 5

CMIP5/PMIP3 Megadroughts

5.1 Motivation and Questions

Some paleoclimate reconstructions and analyses (Cobb et al., 2003; Herweijer et al., 2007; Mann et al., 2009) and modeling evidence (Graham et al., 2007; Seager et al., 2008a; Feng et al., 2008; Oglesby et al., 2012) suggest that observed megadroughts, and more generally past persistent hydroclimate change, were driven by SST boundary conditions in the tropical Pacific and Atlantic Oceans. Nevertheless, in Chapter 3 millennium-length simulations from the ECHO-G model were used to demonstrate that simulated persistent drought in the ASW can be driven by internal variability of the atmosphere alone, thus occurring independently of the exogenous forcing or SST boundary conditions. If such atmosphere-only processes play an important role in generating multidecadal droughts, it potentially would indicate a limited predictability of the onset, persistence and termination of these features, because prediction and projection efforts are largely dependent on slowly changing SSTs and changes in trace gas concentrations, respectively.

Here we use millennium-length simulations from CMIP5/PMIP3, and paleoclimate estimates from the NADA to investigate megadrought dynamics. Two principal questions will be addressed: 1) Does the large collection of CGCMs simulate persistent multidecadal

droughts similar to those in the paleoclimate record? 2) Are these events driven by variations in exogenous forcing conditions and/or oceanic boundary conditions (for instance, the ENSO-ASW teleconnection — Schubert et al., 2004a,b; Seager et al., 2005a, 2008a; Herweijer et al., 2006)? Answers to these questions are critical for improving our understanding of megadrought dynamics and in determining whether CGCMs are capable of providing robust estimates for the range of future hydroclimate states in the ASW and, hence, realistic projections of regional hydroclimate change and variability on decadal-to-centennial timescales.

5.2 Modeled and Proxy-Reconstructed Megadrought Dynamics

5.2.1 Model-Paleo Multidecadal Drought Comparisons

The timeseries of PDSI averaged over the ASW box for the CGCM simulations and the NADA are shown in Figure 5.1, along with the timing and duration of the five highest-ranking droughts (as ranked by the drought identification metric). There are droughts in the model simulations that are characteristic of the severity and persistence seen in the proxy estimates (Figure 5.2). In particular, every model but MIROC simulates at least five 15-year droughts with a cumulative drought severity value between -10 and -17. This is consistent with the NADA, which has eight 15-year droughts, though with a slightly larger cumulative drought severity of -18. Furthermore, all models except MPI simulate at least one 20-year drought, as in the NADA. This suggests that models, in general, are able to simulate persistent drought and that these droughts have similar severity, albeit slightly reduced, relative to the megadroughts in the proxy record.

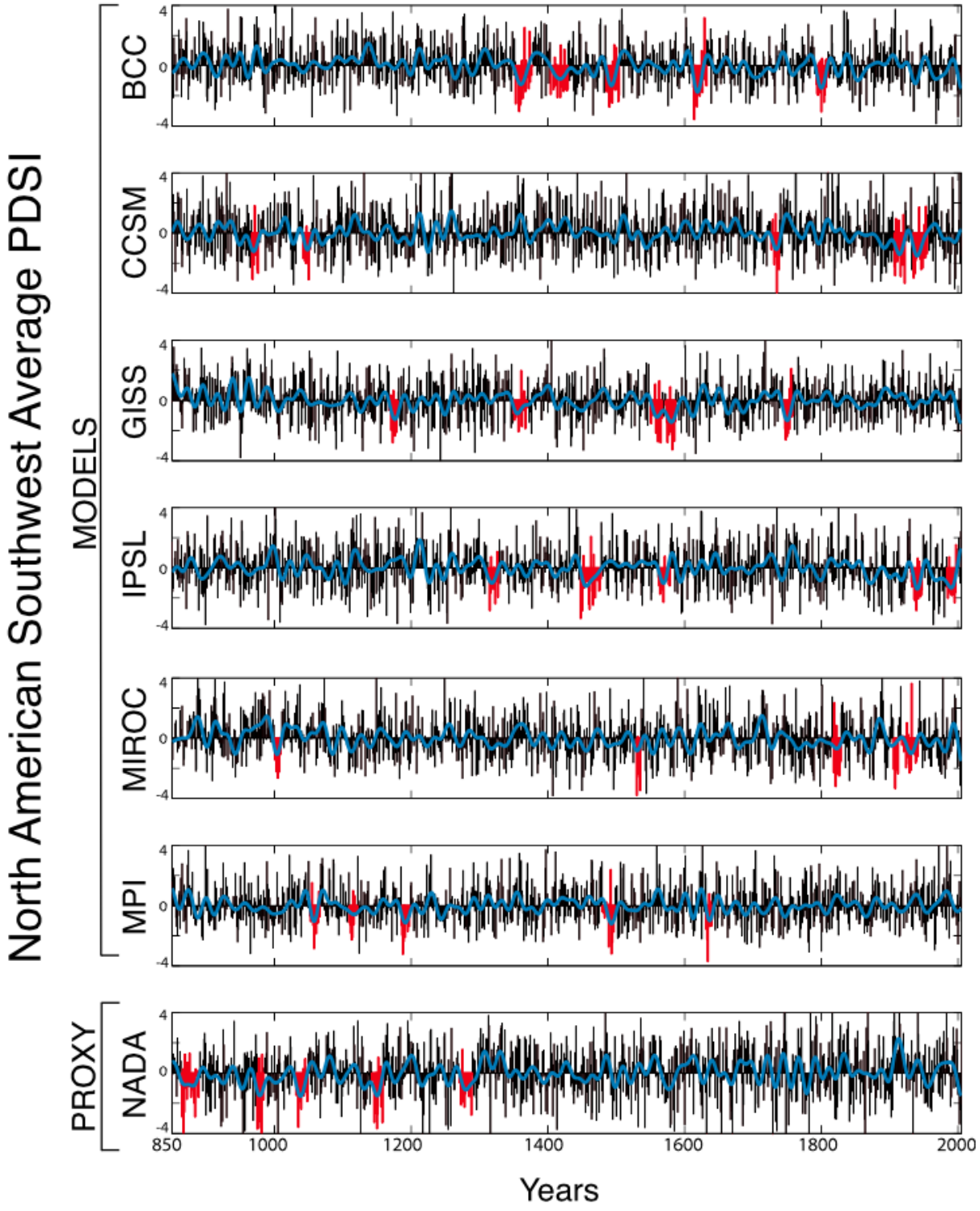

Figure 5.1: Proxy-reconstructed and simulated PDSI for the period 850–2005 C.E. averaged over the ASW region. Annual anomalies (black lines) are shown, along with smoothed versions using a 20-year low-pass filter (blue lines). The red highlighted periods in the annual timeseries are the five highest-ranking droughts, as determined by the drought identification metric.

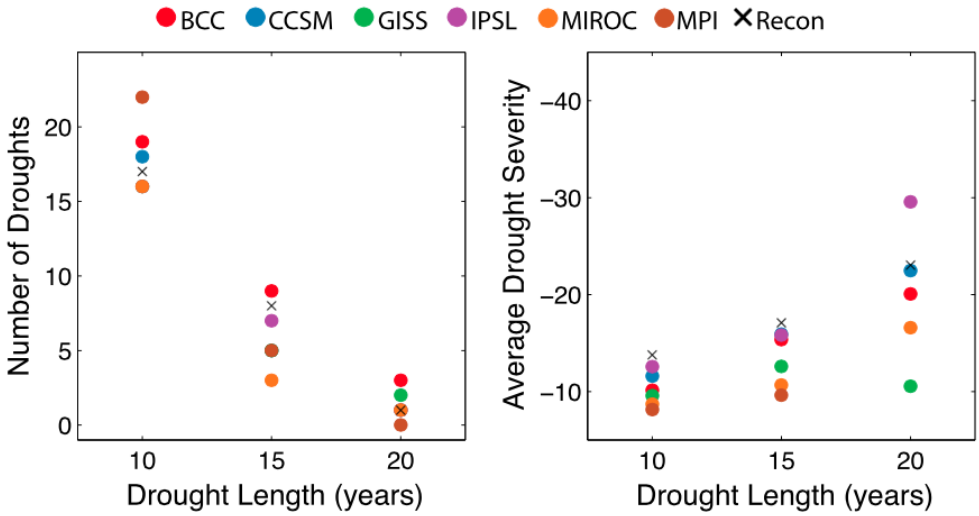

Figure 5.2: (left) The number of 10-, 15-, and 20-year droughts and (right) the average cumulative drought severity for droughts of each length for the full forced simulations, as compared to drought length and severity observed in the NADA reconstruction.

The ability of models to simulate a realistic frequency of persistent drought occurrence is perhaps surprising for three reasons: 1) the CMIP5 models, including those analyzed herein, have been shown to exhibit less hydroclimate persistence than the observed or paleoclimate record (Ault et al., 2013, 2014); 2) the models analyzed herein do not have dynamical vegetation, which has been shown to impact simulated climate variability (e.g. Sun & Wang, 2014); and 3) the individual soil and land surface components within the model ensemble span a range of complexity, which will impact the ability of models to simulate realistic low-frequency variability in terrestrial water storage. None of these issues appears to greatly impact the ability of models to simulate persistent drought that is characteristic of the paleoclimate reconstruction. The apparent impact of point three, however, may be partially mitigated by the use of PDSI, an offline soil moisture estimate, as the analyzed hydroclimate metric.

Although the models are capable of simulating megadroughts in the ASW, these features are not coincident in time across model simulations, despite the fact that the models were run with similar forcing series (see Schmidt et al., 2011, and Figure 5.3, which lists the forcings employed in each simulation). Furthermore, there are no statistically significant interannual correlations between any of the ASW hydroclimate timeseries and weak correla-

tions for 10-year low-pass filtered timeseries (separated using a 10-point Butterworth filter). Nevertheless, the CMIP5 models have different climate sensitivities and, in particular, different parameterizations of land surface and aerosol processes that may drive compensating feedbacks and mask the model response to external forcing. With this caveat, the results presented above suggest that simulated megadroughts, and more generally hydroclimate in the ASW, are predominantly driven by internal variability of the modeled atmosphere-ocean system. A comparison between the number of 10-, 15-, and 20-year drought features in 500-year control simulations and the range in these values for sliding 500-year segments in the forced simulations, however, indicates that exogenous forcing may impact simulated hydroclimate variability in the ASW in different ways for different models (Figure 5.4).

	Orbital	**GHG**	**Volcanic**	**Solar**
BCC	PMIP3 table	Joos table[1]	GRA[2]	VSK[4] + WLS[6] back
CCSM	Internally calculated	Joos table[1]	GRA[2]	VSK[4]
GISS	Internal calculated	Joos table[1]	CEA[3]	VSK[4] + WLS[6] back
IPSL	Internal calculated	Joos table[1]	GRA[2]	VSK[4] + WLS[6] back
MPI	PMIP3 table	Joos table[1]	GRA[2]	VSK[4] + WLS[6] back
MIROC	PMIP3 table	Joos table[1]; CO_2 is model precdicted	CEA[3]	DB[5] + WLS[6] back

[1]https://wiki.lsce.ipsl.fr/pmip3/lib/exe/fetch.php/pmip3:design:lm:ghg_lawdome_giss_merge_c5mip_24jul09.1-2000.txt.

[2]Gao, C., A. Robock, and C. Ammann: Volcanic forcing of climate over the last 1500 years: An improved ice-core based index for climate models. J. Geophys. Res., 113, D2311, doi:10.1029/2008JD010239 (2008).

[3]Crowley, T. et al. Volcanism and the Little Ice Age. PAGES Newsletter, 16, 22-23 (2008).

[4]Vieira, L.E.A., and S. Solanki (2009), Evolution of the solar magnetic flux on time scales of years to millenia, arXiv/0911.4396, doi:10.1051/0004-6361/200913276.

[5]Delaygue, G and E. Bard, (2009), Solar forcing based on Be-10 in Antarctica ice over the past millennium and beyond, EGU 2009 General Assembly, #EGU2009-6943.

[6]Wang, Y.-M., J. L. Lean, and N. R. Sheeley, Jr. (2005), Modeling the Sun's Magnetic Field and Irradiance since 1713, ApJ, 625, 522–538, doi:10.1086/429689.

Figure 5.3: Forcing series used to run the last millennium simulations (from pmip3.lsce.ipsl.fr).

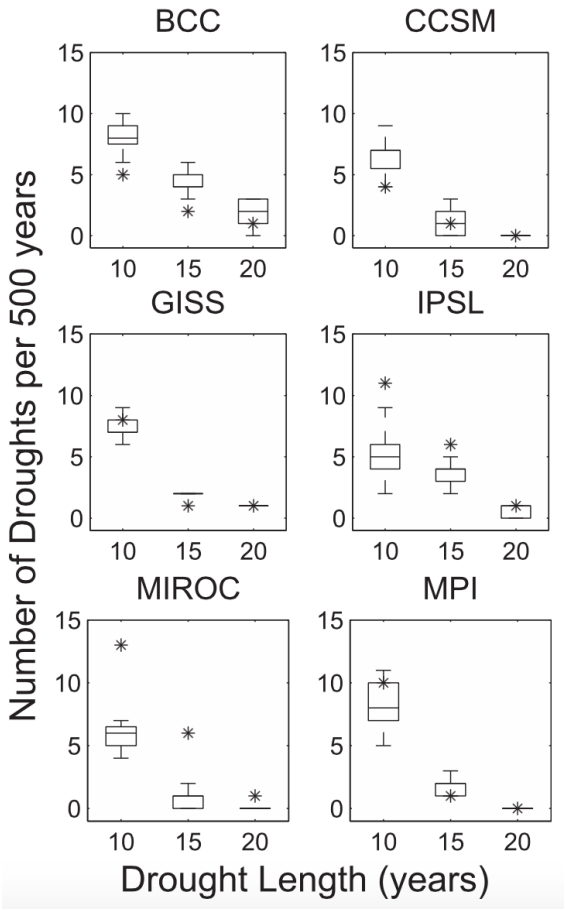

Figure 5.4: The numbers of 10-, 15-, and 20-year droughts (black asterisks) for a 500-year control simulation are plotted with the range in the number of 10-, 15-, and 20-year droughts (whiskers are full range; box plot shows median, 25th, and 75th percentile) for a sliding 500-year window of the full 1156-year period in the forced simulation.

In particular, the MIROC and MPI control simulations have more persistent droughts than the corresponding forced simulations. This was also found for the ECHO-G model in Chapter 3 and suggests that the forcing in some models may act to interrupt persistent hydroclimate features via, for instance, volcanic driven changes to circulation and precipitation. Nevertheless, the analyzed models are split between showing greater or fewer numbers of 10-, 15-, and 20-year droughts in the forced versus the control simulations (BCC tends to have more persistent droughts in the forced simulation, while the range overlaps for CCSM, GISS, and MPI). Furthermore, 10 of the 18 possible combinations of model and drought length yield control values that fall within the range estimated from the forced simulations. There is thus no compelling evidence in the analyzed collection of models for an important and consistent

role played by exogenous forcing in driving simulated hydroclimate variability on decadal and longer timescales. To simplify dynamical interpretations, the diagnosis of megadrought dynamical causes will thus be completed using the 500-year control simulations from each of these models (all analyses hereafter, unless noted, are with these control simulations).

5.2.2 Diagnosis of Megadrought Dynamical Causes

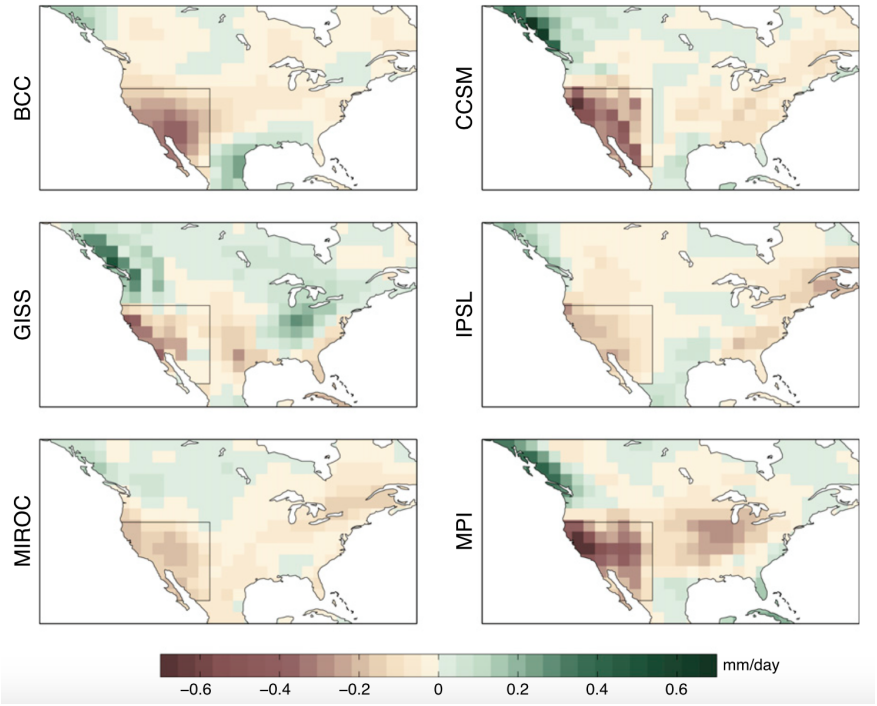

Figure 5.5: Time-weighted composite averages of winter (NDJFMA) precipitation anomalies (mm/day) during the five highest-ranking droughts using the drought identification metric. The full domain is 20°–60°N, 150°–60°W. The straight black lines and the western coastline mark the ASW region.

While the ASW average PDSI indicates that models are capable of simulating megadroughts, the inherent persistence and multiple inputs to PDSI justify the need to determine if changes to precipitation or the surface energy balance, and in what season, are driving these features. An analysis of the surface energy balance and precipitation fields during megadroughts in the winter and summer seasons indicates that megadroughts are consistently associated with anomalously high winter precipitation over the Northwest and low winter precipitation over

the ASW in all of the simulations (Figure 5.5). This spatial pattern is reminiscent of the precipitation anomaly during La Niña winter and spring (e.g. Seager et al., 2014a, their Figure 1), but the analyses in Chapter 3 suggest that atmospheric-only dynamics can produce this feature.

To assess how these models generate megadroughts, Figure 5.6 investigates the association of model megadroughts with various climate modes. If the magnitude of the circle in Panel A of Figure 5.6 is at the 100% drying level, then 100% of the megadrought years are coincident in time with index values of a given dynamic mode that are typically associated with dry conditions in the ASW (based on the references listed in Figure 2.5). The values for each individual megadrought are also plotted in Panel B of Figure 5.6. To test the statistical significance of these associations, we use a bootstrapping method (Schreiber & Schmitz, 2000) to produce 5000 surrogate indices that exactly preserve the distribution of each dynamic-mode index while largely preserving the spectral characteristics (Section 2.7). The magnitude of the artificial indices was recorded for each megadrought year identified in the ASW PDSI timeseries. Significance at the 95% level is achieved if the drying or wetting mode of the true dynamic-mode index is coincident with megadrought years at a percentage greater than 95% of the artificial indices; this assessment is performed for each individual megadrought (to produce the range in the 95% significance levels in Panel B of Figure 5.6) and for all five megadroughts together (Panel A of Figure 5.6). Additionally, only significant model-index combinations that follow contemporary understanding of drought dynamics are analyzed (e.g., statistically significant association between megadroughts and the wetting state of a mode are not considered in detail).

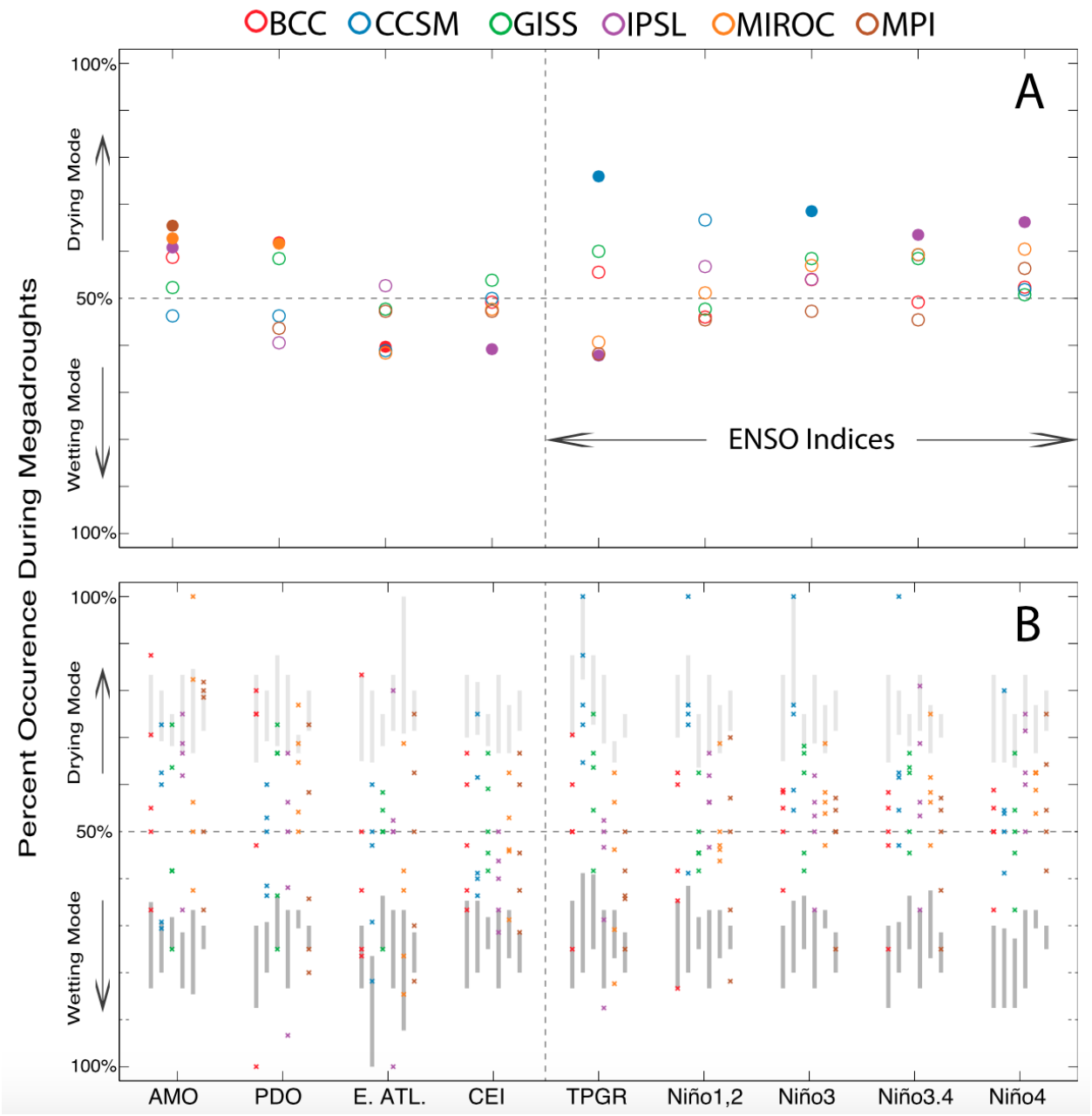

Figure 5.6: (A) The percent occurrence of the wetting and drying mode of each dynamical index during the five highest ranking droughts or megadroughts, considered together, with the filled circles being those index-drought combinations that are significant at the 95% level (using the significance test outlined in Section 2.7). (B) As in (A), but for each of the individual megadroughts (marked by a cross — five in total). The shaded regions in (B) are the range in 95% significance level for the individual megadroughts. In both (A) and (B), for index-drought combinations at 100% drying, every year of the individual megadrought [in (B)] or the five identified megadroughts [in (A)] would have a modal index value (e.g., the TPGR index for ENSO) associated with dry conditions in the ASW (vice versa for wetting).

Seven model-index combinations satisfied the defined significance requirements: CCSM and IPSL with ENSO; IPSL, MIROC, and MPI with the AMO; and BCC and MIROC with the PDO. These results suggest that multiple dynamical mechanisms can drive megadroughts in the majority of the models. For instance, even in models that have a preferred dynamical driver of megadroughts in Panel A of Figure 5.6, there can be individual megadroughts that are associated with the wetting phase of that dynamical mode (e.g., two of the MPI megadroughts and the AMO in Panel B of Figure 5.6). Furthermore, there is little agreement between models on which atmosphere-ocean dynamics are the dominant driver of these features and, in fact, megadroughts driven by internal atmospheric variability cannot be fully discounted for those models that do not exhibit a significant connection to any traditional mode of ocean variability thought to influence hydroclimate conditions over the ASW region (e.g., GISS).

The ability of multiple atmosphere-ocean modes and internal atmospheric variability to drive simulated megadroughts is reaffirmed in Figure 5.7, which shows the composite ND-JFMA average 200 mb geopotential height anomaly for the five highest-ranking droughts in each simulation, with the cross-hatched regions showing agreement in sign with the composite anomaly for at least four of the five droughts. As was suggested in Figure 5.6, models vary in their geopotential height fields during the simulated megadroughts, indicating that multiple dynamical mechanisms can produce these features. The one relatively consistent feature across the models is a high geopotential height anomaly in the north/central Pacific that would be associated with dry, subsiding air and a northward shift of the storm track away from the ASW. These features are reminiscent of the geopotential height field forced by a La Niña-like state in the tropical Pacific (e.g., Chapter 3, Seager et al., 2014a). The model behavior is similar to what was found in the forced and control ECHO-G simulations analyzed in Chapter 3, where stochastic atmospheric variability was found to drive persistent drought.

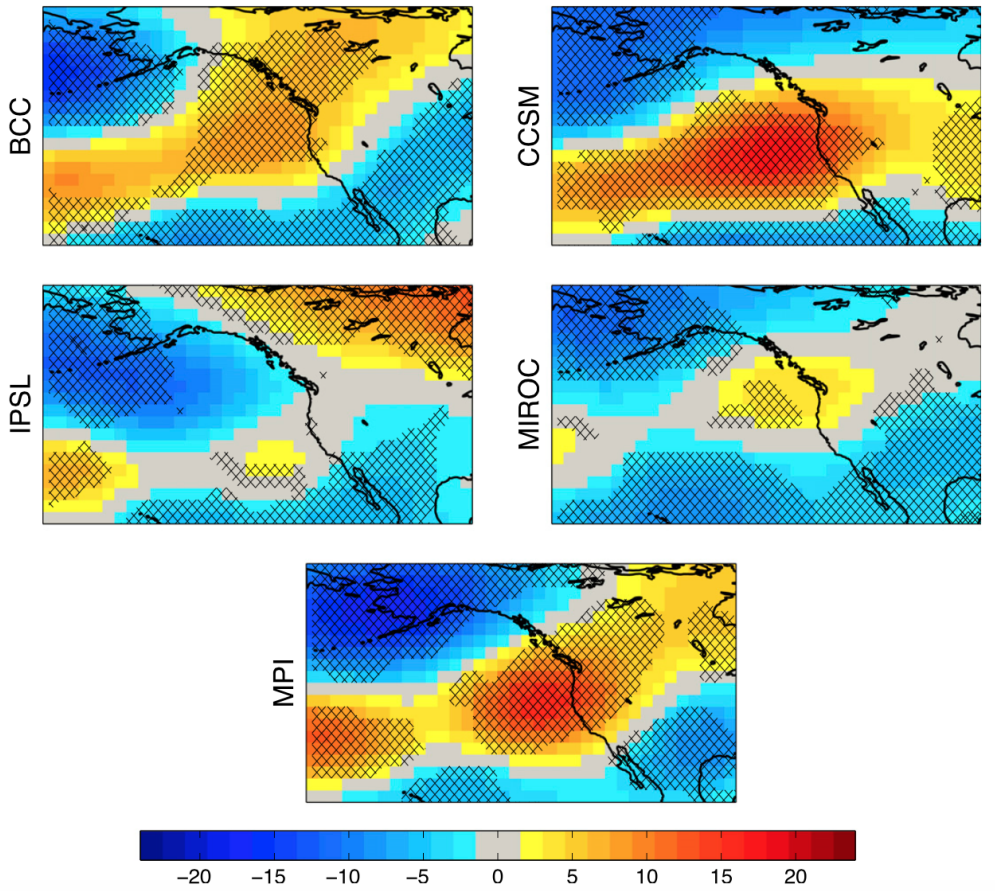

Figure 5.7: Composite NDJFMA average 200 mb geopotential height anomaly for all years identified as occurring during the five highest-ranking droughts in each control simulation. Cross-hatching indicates that the sign of the geopotential height anomaly is in agreement with the composite for at least four out of five identified droughts. The full domain is 20°–70°N, 180°–90°W. Note: the GISS simulation does not have geopotential height fields available for the full control simulation and is not included in this figure.

5.2.3 Megadroughts in the CCSM Simulation

The tropical Pacific has been hypothesized to play a role in megadroughts (Meehl & Hu, 2006; Cook et al., 2007; Herweijer et al., 2007; Seager et al., 2007, 2008a; Graham et al., 2007; Oglesby et al., 2012) because it has been established as the dominant driver of interannual hydroclimate variability in the ASW (Schubert et al., 2004a,b; Seager et al., 2005a, 2008a; Herweijer et al., 2006) and this hypothesis was buoyed by some paleoclimate evidence that the tropical Pacific was cold during the MCA (Cobb et al., 2003; Mann et al., 2009). Despite this, only CCSM and IPSL exhibit a coherent state of the tropical Pacific during the simulated megadroughts. While both models have a tropical Pacific-megadrought

connection, CCSM is anomalous with respect to the control of the tropical Pacific on persistent drought, with all five of the five highest-ranking droughts coincident with a persistent La Niña-like state (and with 76% of megadrought years corresponding to a positive TPGR). Next, we examine whether this tropical Pacific-megadrought connection in CCSM arises from a shift in ENSO variability or the mean state, whether the changes in the tropical Pacific are driven by exogenous forcing or internal variability, and why this tropical Pacific-megadrought connection is particularly strong in CCSM.

Tropical Pacific Mean State or ENSO Variability?

The top and bottom panels of Figure 5.8 show histograms of the percentage of La Niña years (defined as a half standard deviation of the Niño3.4 index below the mean) and the Niño3.4 variance in 27-year windows (chosen to reflect the length of the longest drought in the record). The 27-year window has been slid every five years through the full length of the CCSM simulation to derive the distributions shown in Figure 5.8. The bins with the 27-year window that corresponds to each of the five highest-ranking droughts in the CCSM simulation are marked with red crosses. The locations of these markers within the statistical distributions demonstrate that megadrought periods in the CCSM simulation are not characterized by a large number of La Niña events or unusual ENSO variance and instead have approximately average Niño3.4 statistics (mean, variability, and distribution). In contrast, the megadrought periods are consistent with a shift toward a more La Niña-like mean state (as indicated by the anomalously positive TPGR index values in Figure 5.6), suggesting that this shift in the mean state is what drives megadroughts in the CCSM model.

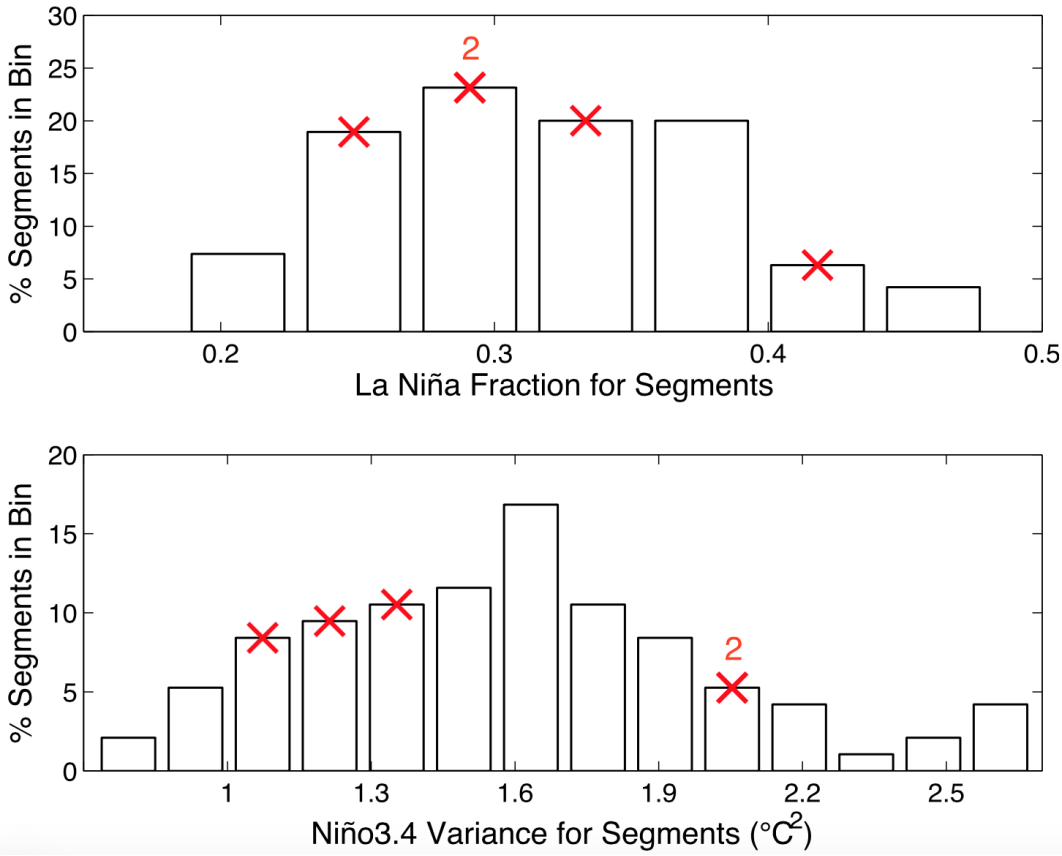

Figure 5.8: (top) Histogram of the fraction of La Niña years (defined as a half standard deviation below the mean) in sliding 27-year segments of the CCSM control simulation. (bottom) Histogram of the Niño3.4 variance in the same segments. The bins that correspond to the values during the five highest-ranking CCSM drought periods are plotted with a red cross (if two fall in the same bin, it is marked as such).

Forced or Internal Mean-State Changes?

To assess the dynamics that drive variability in the tropical Pacific in CCSM on megadrought (between 10- and 20-year) timescales, the EOFs of the 20-year low-pass filtered tropical Pacific (20°S–20°N, 100°E–70°W) SST field were computed. The principal components (PCs) were then compared to the TPGR index to determine if a particular mode of variability corresponds to low-frequency variations in the TPGR. The second EOF (Figure 5.9) and associated PC explains 90% of the variance in the TPGR on these timescales. As noted in Karnauskas et al. (2012), this pattern is consistent with the internal Pacific centennial oscillation (PCO) mode of variability. It is thus the PCO that produces the tropical Pacific mean-state changes in CCSM that are then driving megadroughts in the ASW.

This suggests that predominantly internal variability of the tropical Pacific Ocean, manifest as changes to the mean state, can drive megadroughts in CCSM. It is difficult, however, to determine unequivocally that exogenous forcing does not impact mean-state changes in the model, particularly given that forcing can project onto internal modes of climate variability (Palmer, 1993). Nevertheless, a comparison of trends in the TPGR on multidecadal timescales in the forced and control simulations indicate that the PCO-driven mean-state changes in the control simulation are as large as any in the forced run (Figure 5.10; justification for the use of a 56-year window to calculate the trend is provided in the following subsection).

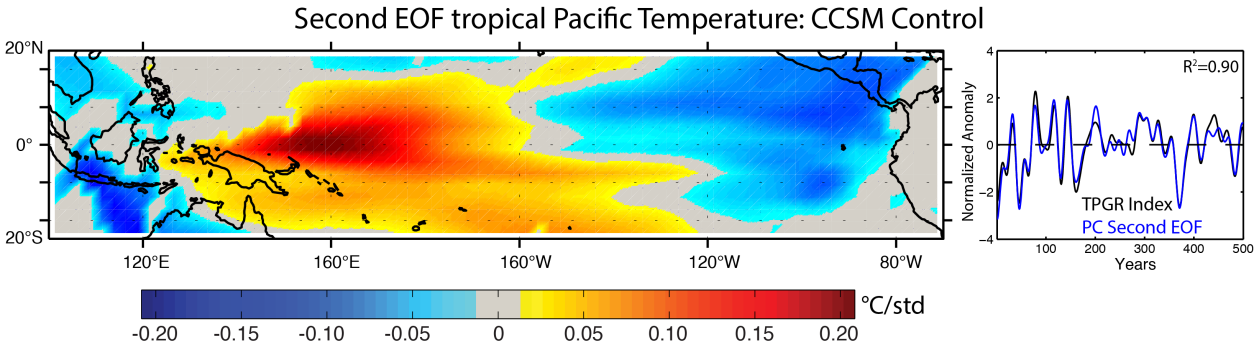

Figure 5.9: (left) The pattern of the second EOF in the 20-year low-pass filtered 500-year CCSM control simulation. (right) The PC (black) plotted with the 20-year low-pass filtered TPGR (blue) from that simulation. The R^2 between these timeseries is listed at top right of the right panel.

Why the CCSM?

Why does CCSM have an extratropical hydroclimate response to mean-state changes in the TPGR, and why do other models not exhibit similar behavior? First, CCSM, of all the PMIP3 models, yields the largest trends in the TPGR on multidecadal timescales (up to 0.15°C per decade for 56-year periods; Figure 5.10). The 56-year period was chosen to reflect the length of the NCEP-NCAR reanalysis (Kalnay et al., 1996) and the time period used to assess teleconnection stationarity in Chapter 4. For reference, a 0.15°C per decade trend in the TPGR is five times the magnitude of the TPGR trend between 1950 and 2005 C.E. in the NCEP-NCAR reanalysis. This result suggests that CCSM will have the largest mul-

tidecadal changes in the mean state of the tropical Pacific Ocean. To maintain consistency with Karnauskas et al. (2012), the same analysis was also completed for 125-year trends in the TPGR, and the same relative magnitude of TPGR trends between models was found.

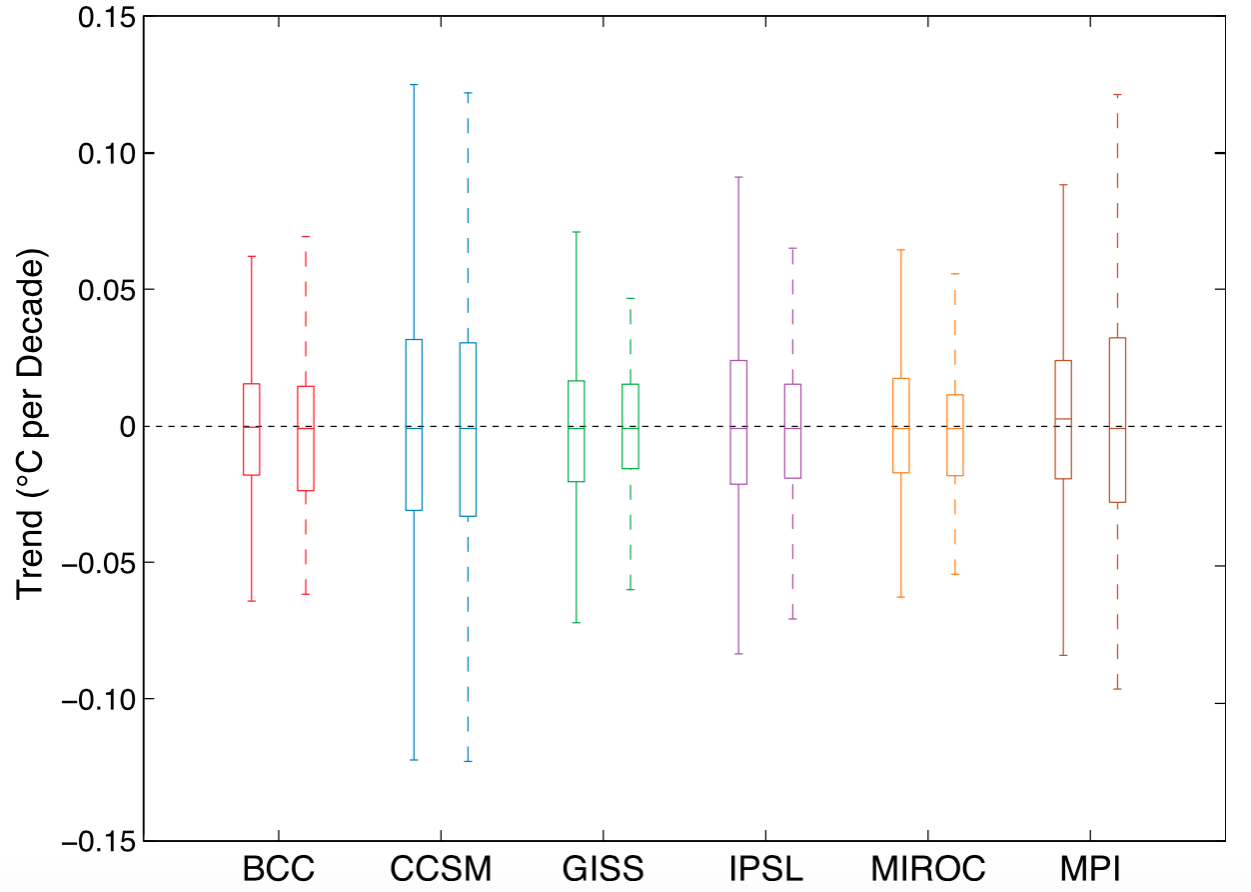

Figure 5.10: Range of trends in the TPGR (°C per decade) for 56-year sliding windows in each forced (solid whiskers) and control (dashed whiskers) simulation. A La Niña-like trend is positive.

In addition to the strong multidecadal variability in the TPGR, CCSM exhibits a very realistic ASW-ENSO teleconnection pattern and strength that is stationary on multidecadal timescales. This is characterized in Chapter 4 and most explicitly in Figure 4.2. Importantly, the consistent representation of the observed interannual connection between NA and the tropical Pacific across the full CCSM simulations is not as robust in the other CMIP5 models, which is to say that CCSM has the most stationary teleconnection between NA and the tropical Pacific.

Strong tropical Pacific control on ASW hydroclimate occurs over the instrumental interval, but if the features of this teleconnection were to change through time, the tropical Pacific likely would have varying degrees of control over hydroclimate in the ASW. The fact that CCSM both faithfully represents the observed teleconnection and maintains the teleconnection features throughout the simulation is critical in this regard and allows changes in the mean state of the tropical Pacific Ocean, which CCSM simulates with relatively large magnitude, to generate megadroughts. All of the other models exhibit weaker teleconnections that are less realistic and also less stationary, and/or display weaker mean-state changes in the tropical Pacific Ocean. Following the hypothesis in Chapter 3, such model behavior allows stochastic atmospheric variability and non-ENSO oceanic modes of variability to produce storm track shifts (and associated hydroclimatic changes like ASW drought) that are uninterrupted by the influence of the tropical Pacific Ocean.

Megadrought Dynamics in the Other Models and the CCSM Hypothesis

As in CCSM, megadroughts in the IPSL model are significantly connected to the tropical Pacific at the 95% level. In this case, the significant relationships are between megadroughts and the Niño3.4 and Niño4 indices, but importantly, these connections are weaker than between megadroughts and the TPGR in CCSM (with 65% and 67% of megadrought years corresponding to the drying mode of these indices, respectively; Figure 5.6). Interestingly, IPSL also shows a significant connection between megadroughts and a negative or El Niño-like state in the TPGR. This is indicative of what was suggested in Section 2.6, that some ENSO indices do not adequately capture ENSO variability in some models.

The behavior of IPSL — which has a significant connection between megadroughts and the tropical Pacific Ocean, but one that is weaker than in CCSM — and the other models that do not exhibit this connection can be better understood in the context of the CCSM behavior outlined in the previous section. If models have a realistic and stationary teleconnection, with large multidecadal variability in the tropical Pacific Ocean, as in CCSM, then

the simulated megadroughts should be driven consistently by the tropical Pacific boundary conditions. The IPSL model does, in fact, exhibit a strong and stationary teleconnection between NA and the tropical Pacific (Figure 4.2). Furthermore, it has moderate variability in the tropical Pacific Ocean, exceeded only by MPI and CCSM. In the context of the above-outlined hypothesis, if this variability were larger, the connection between the tropical Pacific Ocean and megadroughts would be stronger, as in CCSM. Nevertheless, the IPSL model has the most CCSM-like tropical Pacific variability and teleconnection behavior, and, of the other five models analyzed herein, would be expected to have megadroughts that are most strongly connected to the tropical Pacific boundary conditions.

The other models exhibit fewer of the characteristics hypothesized to be necessary for simulating megadroughts that are consistently forced by the tropical Pacific boundary conditions. The BCC and GISS models have a moderately realistic and stationary teleconnection but weak variability in the tropical Pacific on multidecadal timescales. The MPI model has large variability in the tropical Pacific on multidecadal timescales but a highly nonstationary teleconnection. The MIROC model has both weak variability in the tropical Pacific and a highly nonstationary and likewise unrealistic teleconnection.

5.3 Conclusions

Models from the CMIP5/PMIP3 generation are capable of simulating megadroughts in the ASW that are similar in duration and magnitude to those observed in the paleoclimate record. The droughts are not, however, temporally synchronous with those in the proxy record. Furthermore, there is very little overlap between the drought features in models, despite the use of similar forcing series to drive these simulations. This suggests that model-simulated megadroughts can result from internal variability of the modeled climate system, rather than as a response to changes in exogenous forcings, or that models exhibit compensation between feedback mechanisms that masks a forced hydroclimate response.

While stochastic atmospheric variability is able to drive persistent drought in CGCMs (e.g. Chapter 3), it is not a robust feature. In particular, models with strong and stationary teleconnections (e.g., CCSM) and large multidecadal variability in the tropical Pacific, simulate megadroughts driven by internal variability of the tropical Pacific mean state. A dominant role for the tropical Pacific Ocean in driving megadroughts is consistent with a prominent hypothesis for the origin of these features in the real world. Nevertheless, the decadal to, at most, multidecadal character of the tropical Pacific mean state changes in CCSM and the internal dynamics that produce this variability are not. Additionally, the characteristics of the CCSM model are not necessarily realistic and in many ways CCSM is an outlier when considering the full CMIP5 model ensemble. Characterizing CCSM within the context of real-world megadrought dynamics will provide important information on the predictability of regional extratropical hydroclimate on decadal-to-multidecadal timescales. Such an effort will be presented in Chapter 7.

Chapter 6

CMIP5/PMIP3 Spatial Features and Megadrought Seasonality

6.1 Spatial Features

6.1.1 Motivation and Questions

Up to this point megadroughts in the models and paleoclimate record have been analyzed using a timeseries averaged over the ASW. There is evidence, however, that drought conditions during past megadroughts extended beyond the ASW. During much of the MCA, for instance, the Great Plains (GP) region of NA also experienced drought conditions (Cook et al., 2010b). In fact, droughts during the MCA were often pancontinetal (Cook et al., 2014b), with drought conditions simultaneously affecting the majority of the area represented by the present day United States. Pancontinetal droughts such as these have occurred over the instrumental interval. In 2012, for instance, 62% of the contiguous United States was classified as moderately or extremely dry. The potential socioeconomic impact of a future megadrought occurrence (e.g. in the Introduction) would be amplified if such features were pancontinental in character. This is because simultaneous drought impacts

across regions with distinct water resource constraints (e.g., irrigation from rivers versus groundwater), ecosystems (e.g., forests and grasslands), and crops would pose significant management challenges. The 2012 drought provides a stark example of these impacts, as it was the fourth most costly weather or climate event of the last 20 years (behind hurricanes Ike, Katrina and Sandy — https://www.ncdc.noaa.gov/billions/events).

There are two fundamental reasons why a comprehensive characterization of pancontinental droughts, and their causes, proves challenging. First, regional hydroclimate variability is characterized by distinct atmosphere-ocean dynamics, for instance, SW hydroclimate variability is controlled primarily by winter precipitation variability coupled to the tropical Pacific Ocean (e.g. Herweijer et al., 2006; Seager et al., 2008a; Schubert et al., 2009), while the GP has predominantly summer hydroclimate variability that is driven by the tropical and subtropical Atlantic Ocean (e.g. Sutton & Hodson, 2005; Kushnir et al., 2010) in addition to the tropical Pacific Ocean (Seager et al., 2005b). Second, the relative rarity of pancontinental drought and the short (150 year) observational record means that there are few events by which to diagnose how relatively distinct regional hydroclimate dynamics can combine to produce pancontinental drought. In this first section of Chapter 6 we therefore use the same paleoclimate model-data comparison framework as in Chapter 5 to analyze pancontinetal drought. We ask three fundamental questions: 1) Are models able to reproduce the statistics of pancontinental drought occurrence as represented by the NADA? 2) Do the models have centennial-scale variability in the occurrence of pancontinental droughts (e.g. the increase in these features during the MCA), and if so, is this driven by forced or internal variability? and 3) What are the simulated atmosphere-ocean dynamics that drive pancontinental droughts in the model simulations? It is important to note that while these analyses are motivated by the pancontinental character of megadroughts, pancontinental droughts as defined herein are single-year events. Megadroughts, by contrast, are likely to have changing spatial expressions over the multiple years of their occurrence.

6.1.2 Defining Pancontinental Drought

Following Cook et al. (2014b), the regional boundaries used in this chapter are the SW, 32°–40°N, 125°–105°W; the CP, 34°–46°N, 102°–92°W; the Northwest (NW), 42°–50°N, 125°–110°W; and the Southeast (SE), 30°–39°N, 92–75°W. Similar to results shown for the NADA in Cook et al. (2014b), the designated regions in the models do not have climate variability that is completely independent. Nevertheless, correlation maps between the four regionally-averaged time series and gridpoint PDSI indicate that the hydroclimate within each region is homogenous and that variability between individual regions is largely independent (not shown).

Again following Cook et al. (2014b), droughts are characterized to have occurred in the regional-mean time series when PDSI falls to a value of -0.5 or lower in any individual year. Pancontinental droughts are then defined as occurring when any three [SW, CP, and SE (hereinafter SW+CP+SE); SW, CP, and NW (hereinafter SW+CP+NW); SW, NW, and SE (hereinafter SW+ NW+SE); or CP, NW, and SE (hereinafter CP+NW+SE)] or all four [SW, CP, NW, and SE (hereinafter SW+CP+NW+SE)] of the regional mean time series simultaneously have PDSI values of -0.5 or lower in the same year. By this definition, the four-region droughts will overlap with, and also be counted as, three-region droughts. For some of the analyses noted in the results section the three- and four-region droughts were treated as distinct events.

6.1.3 Are Megadroughts Pancontinental?

There is evidence that the MCA, the period with the greatest incidence of megadroughts, was also characterized by relatively frequent pancontinental drought (Cook et al., 2014b). Likewise, spatiotemporal analysis of MCA megadroughts suggests that they have a large spatial extent (e.g. Herweijer et al., 2007). Nevertheless, to directly assess if megadroughts are pancontinental, the percentage of megadrought years that also satisfy the pancontinental

drought definition in Section 6.1.2 is compared to the percentage of all years that are pancontinental in Figure 6.1. In the NADA, the five highest-ranking droughts are more likely to be pancontinental than a normal year (37% versus 20% for all years). Additionally, these values are 48% for the five highest-ranking droughts relative to 40% for all drought years over the ASW (not shown). While this shift is modest, given the socioeconomic risk associated with both megadroughts and pancontinental drought it is important to better understand the origin of these features and their relationships. In models, the shift in the percentage of pancontinetal drought years for the five highest-ranking droughts is most consistent with the NADA in the GISS and MPI simulations (Figure 6.1). The other models, however, may still be useful for understanding pancontinental drought and such analyses will determine if CGCMs are capable of reproducing the statistics of past pancontinental drought occurrence as a consequence of the correct dynamical drivers, which is necessary to assess whether state-of-the-art CGCMs can accurately constrain future drought risks.

Data Set	Probability PC Drought Megadrought	Probability PC Drought All Years
NADA	37%	20%
BCC	28%	20%
CCSM	32%	25%
GISS	32%	15%
IPSL	34%	22%
MIROC	23%	18%
MPI	37%	20%

Figure 6.1: (left column) The percentage of years during the five highest-ranking droughts that are also pancontinental using the definition in Section 6.1.2. (right column) The percentage of all years that are pancontinental, this does not include drought years that are a part of the five highest-ranking droughts.

6.1.4 Pancontinental Drought Occurrence

Figure 6.2 shows the drought recurrence interval for the individual geographic regions in both the forced and control simulations from the models (dark and light bars, respectively)

and the NADA. Models, in general, are able to simulate the correct recurrence interval for drought in each of the regions. The model ensemble, however, slightly overestimates the occurrence of SW and NW drought, and underestimates the occurrence of drought in the CP and SE. This model behavior may be suggestive of more realistic, and in some cases overactive, ENSO variability and teleconnections (e.g., CCSM — Chapter 5) relative to other modes of coupled atmosphere-ocean variability, because ENSO-driven hydroclimate variability tends to load heavily on western NA and thus predominantly affects the SW and NW.

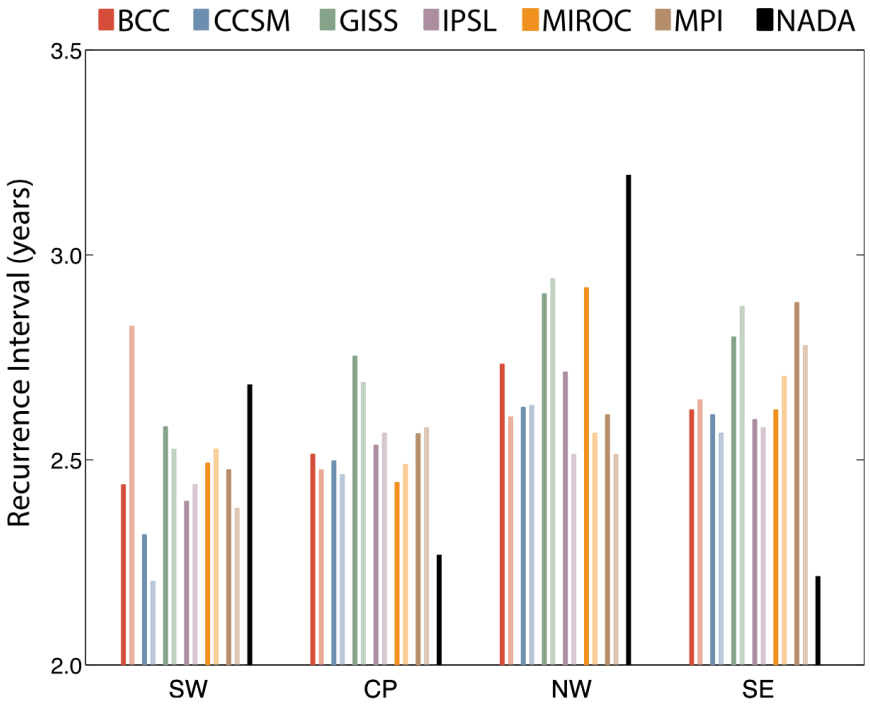

Figure 6.2: Drought recurrence intervals for each region. Reconstruction results are shown in black. Model results are shown in color, where the lighter-shaded bars of the paired colors represent the recurrence value for a control simulation from each model, while the darker-shaded bars are from the associated forced simulation.

The model ensemble is also largely successful at simulating the pancontinental drought recurrence intervals characterized by the NADA (again for both forced and control simulations; see Figure 6.3). Taken individually, however, the models appear split into two categories, with CCSM, IPSL, and MPI slightly underestimating the recurrence interval of pancontinental drought of all types and GISS and MIROC overestimating the recurrence

interval of these droughts by a much larger margin (BCC has realistic recurrence intervals for three of the five pancontinental drought types). Nevertheless, the spread of the model ensemble encompasses the pancontinental drought recurrence interval of the NADA for each drought type. Furthermore, each model is individually successful at capturing the relative occurrence of the different types of pancontinental drought, for instance, the SW+CP+SE combination being the most common and the SW+CP+NW+SE combination being the least common.

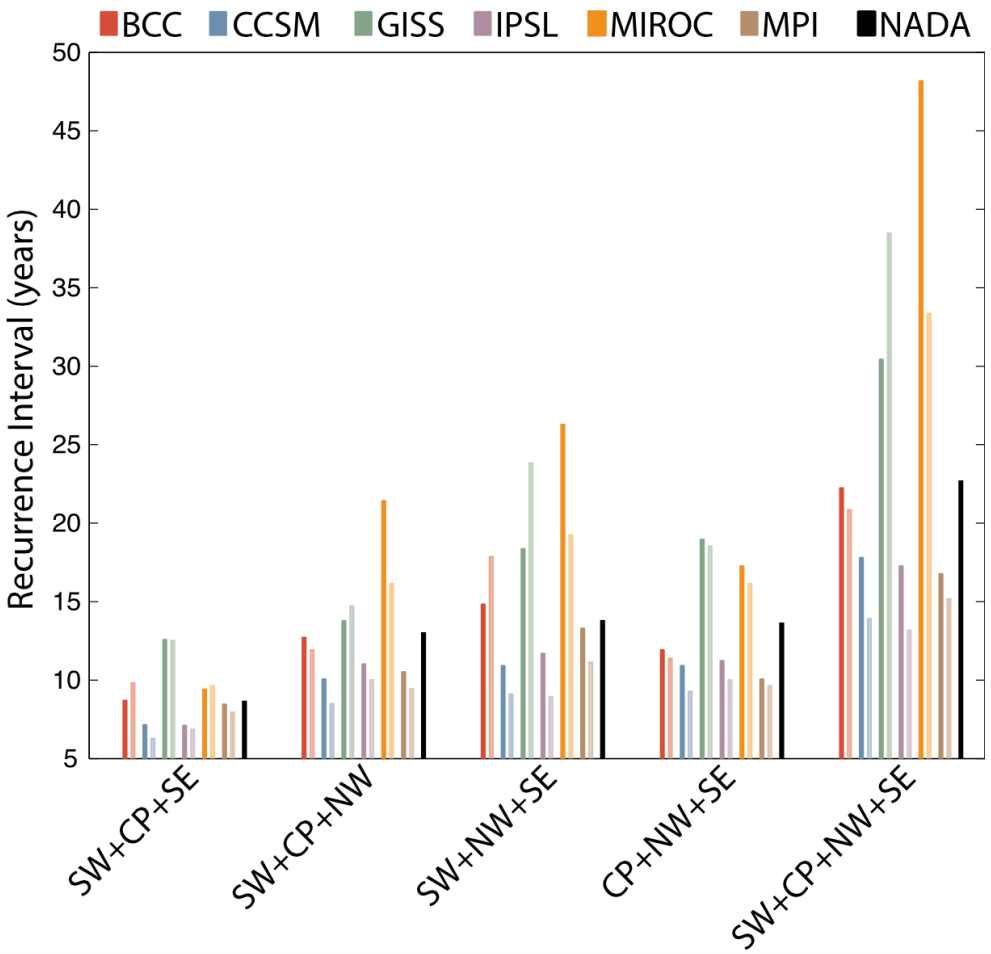

Figure 6.3: Drought recurrence intervals for each type of pancontinental drought. Reconstruction results are shown in black. Model results are shown in color, where the lighter-shaded bars of the paired colors represent the recurrence value for a control simulation from each model, while the darker-shaded bars are from the associated forced simulation. To maintain consistency with Cook et al. (2014b), drought years were allowed to overlap between the three- and four-region droughts.

The recurrence intervals for the droughts in the individual regions and for pancontinental droughts are not consistently different for the forced and control simulations (Figures 6.2 and 6.3). This suggests that the simulated pancontinental drought dynamics are not dependent on the exogenous forcing and, as such, provide confidence in the use of control simulations to assess simulated atmosphere-ocean variability and its connection to pancontinental drought (Section 6.1.6). These findings are consistent with Chapters 3 and 5 that focused specifically on the dynamics of persistent droughts in the ASW.

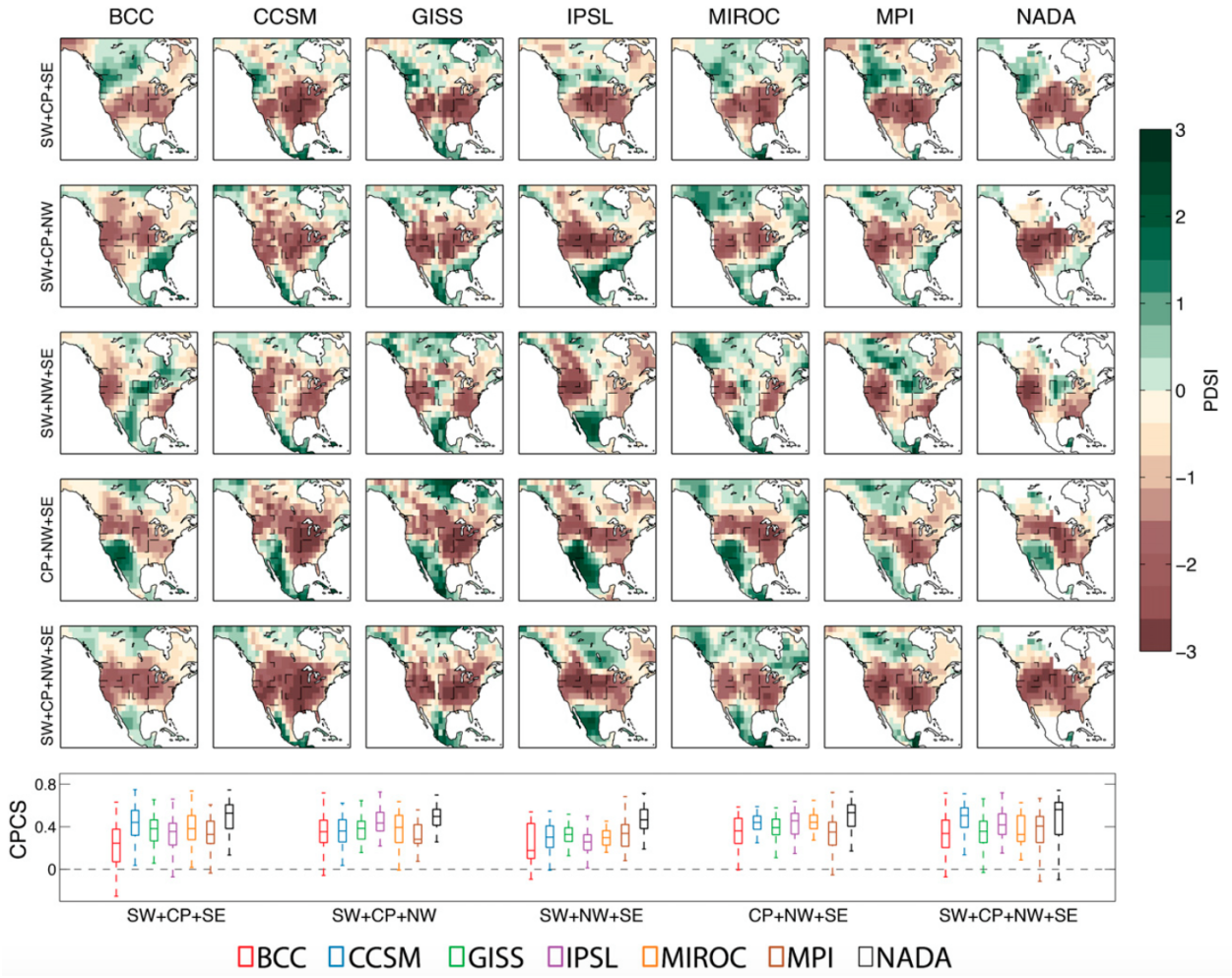

Figure 6.4: In the top five rows, PDSI composites or averages over all pancontinental drought years of each type are shown. (bottom) The range in CPCS for individual droughts with the NADA composite pattern. Boxplot colors indicate the associated control model simulation or reconstruction. Unlike in previous figures, drought years were not allowed to overlap between the three- and four-region droughts.

The composite PDSI patterns of each pancontinental drought type for the control model simulations and reconstruction are plotted in Figure 6.4. The bottom panel of Figure 6.4 shows the CPCS calculated between the composite PDSI pattern from the NADA and each individual pattern of that pancontinental drought type. The range in CPCS is thus a measure of the consistency of individual drought patterns (small range being more consistent), with the average magnitude of the CPCS values for each model being indicative of how well the model composite matches the NADA composite. These values have been calculated separately for the three- and four-region droughts (unlike in previous analyses). The composite model patterns compare well with the NADA composite for all but the SW+NW+SE droughts, which are the least common of the pancontinental drought types. The CPCS range in the models and the NADA are likewise consistent for all but the SW+NW+SE combination. Nevertheless, it is important to note that for all drought types there is a large CPCS range in both the models and the NADA, indicating that individual pancontinental droughts can have different spatial patterns. Pancontinental droughts driven by a consistent dynamical driver might be expected to have a consistent pattern. If this is the case, the large CPCS range may then suggest that multiple dynamical drivers are capable of producing each type of pancontinental drought. Equally likely, however, is that pancontinental droughts are influenced not just by SST variations but also by internal atmospheric variability that can create different spatial patterns, as was argued by Hoerling et al. (2014) for the 2012 drought. A third possibility is that a large CPCS range would also be expected if pancontinental droughts were driven by consistent dynamical drivers but with teleconnection dynamics that are variable through time. The question of pancontinental drought dynamical drivers will be addressed in Sections 6.1.6 and 6.1.7.

6.1.5 Centennial Variability in Pancontinental Drought

Perhaps the starkest characteristic of the NADA drought record is the centennial-scale variability in the number of pancontinental droughts, punctuated by an increased rate

of occurrence in the MCA relative to the LIA (Cook et al., 2014b). The relative timing of hydroclimate change in the models — if such changes are present in the CMIP5 models — and the NADA is of particular interest because exogenous forcing may, or may not, have played a role in driving the MCA-to-LIA transition (e.g. Mann et al., 2009; Gonzalez-Rouco et al., 2011; Goosse et al., 2012, and Chapter 5). If, in fact, radiative forcing produced this transition, it would be relevant to our understanding of current and future radiatively forced climate change. Because the models are driven with similar forcing series (see Schmidt et al., 2011), a strong role for exogenous forcing in driving periods with increased pancontinental drought frequency should lead to these periods being contemporaneous in time across the model simulations. The role of radiative forcing in driving the variability of pancontinental drought frequency on centennial timescales can therefore be tested to potentially better understand the origin of this variability in the NADA. It must be noted, however, that the CMIP5 models have different climate sensitivities and, in particular, different parameterizations of land surface and aerosol processes that may drive compensating feedbacks and mask the model response to external forcing (as was also noted in Chapter 5). If these differences are large, they would impact our ability to test the role of forcing as posed above.

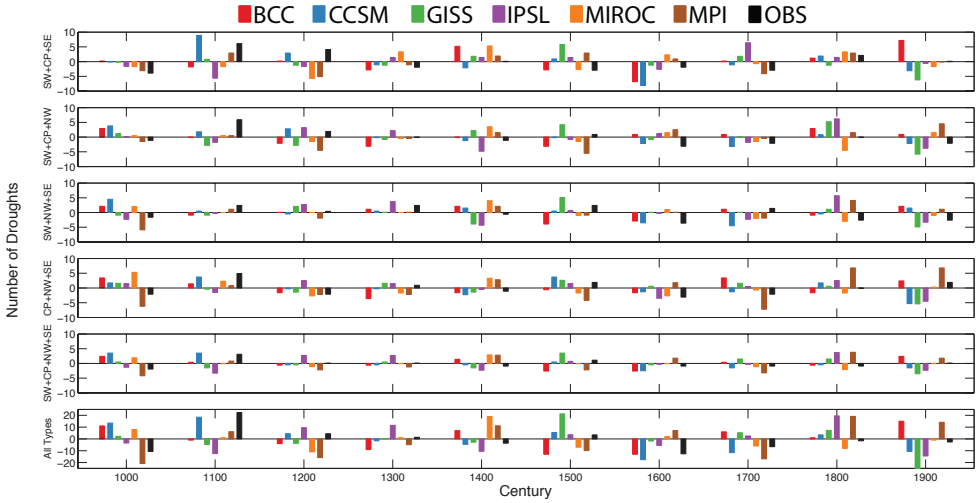

Figure 6.5: Number of pancontinental drought years in each century relative to the mean number of droughts per century between 1000 and 2000 C.E. To maintain consistency with Cook et al. (2014b), drought years were allowed to overlap between the three- and four-region drought categories. Bar color indicates the forced model simulation or reconstruction.

The number of pancontinental droughts for each century relative to the mean number of droughts per century between 1000 and 2000 C.E. is plotted for the forced model simulations and the reconstruction in Figure 6.5. For the NADA, the percentage increase in the number of pancontinental droughts, relative to mean conditions, during the twelfth century averages to 60%, with a maximum increase of 75% for the SW+CP+NW drought type and a minimum of 40% for the SW+NW+SE type. This period of increased drought frequency does not appear to be captured by the models, nor do the individual models agree on the timing of hydroclimate change, suggesting that these changes are not tied in any coherent way to the exogenous forcing. A possible exception is the CCSM model, which exhibits increased aridity during the eleventh and twelfth centuries (particularly manifest in the number of SW+CP+SE drought occurrences, although the number of droughts in both centuries is within the range from the CCSM control simulation); changes that are contemporaneous with those in the NADA. The models do, however, appear to simulate a large range in the number of pancontinental droughts. To test if this range is of the magnitude observed in the NADA, the number of each pancontinental drought type was calculated for a sliding 100-year window across the forced model simulations and NADA record and the range is plotted in Figure 6.6. Each model is individually capable of simulating centennial-scale variability in the frequency of pancontinental drought occurrence that is characteristic of the NADA. The fact that models simulate large differences in the number of pancontinental drought features for different 100-year periods, and that these changes are not tied in any coherent way to the exogenous forcing, is suggestive of a large amount of internal variability on centennial timescales. This model behavior is consistent with Chapters 3 and 5 that focused on the dynamics of persistent drought in the ASW. Additionally, if the model dynamics are in fact representative of the real atmosphere-ocean system, then this result indicates that the observed preponderance of pancontinental droughts during the MCA could have arisen from internal variability, as opposed to changes in radiative forcing.

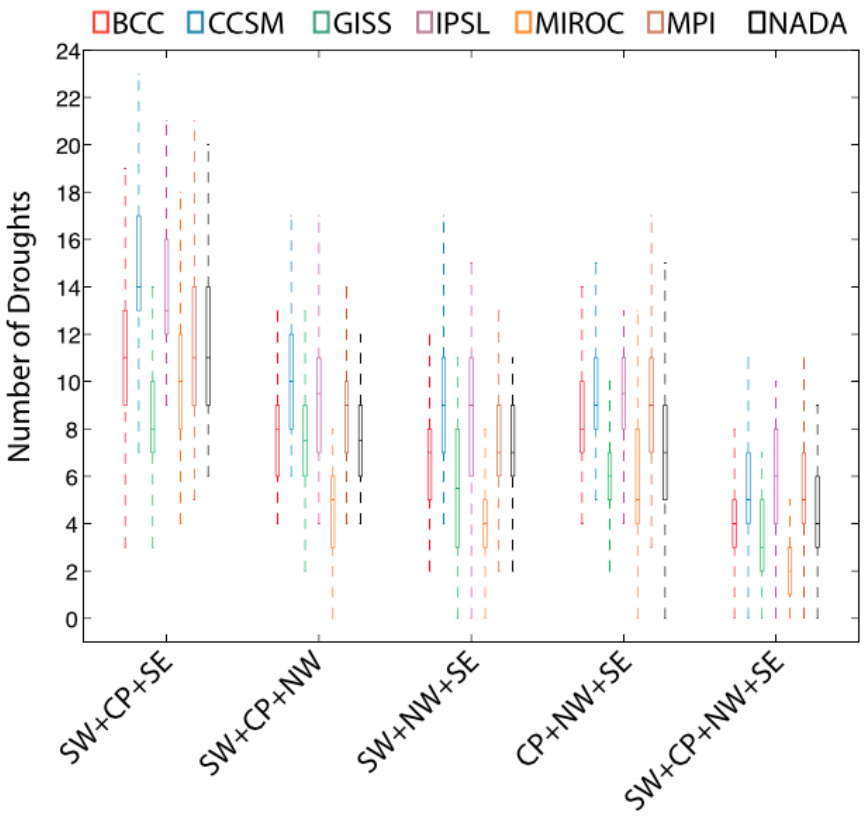

Figure 6.6: Ranges in the number of drought years for each pancontinental drought type. This was calculated for a sliding 100-year window across the model record or reconstruction. Boxplot colors indicate the associated forced model simulation or reconstruction.

6.1.6 Observed Pancontinetal Drought Dynamics

Figure 6.7 analyzes the associations between pancontinental droughts and the dynamical drivers using the overlapping period between the observed dynamics (the SST observations begins in 1854 C.E.) and the reconstruction (1854–2005 C.E. — hereinafter observation-to-reconstruction). The specific methodology, a full explanation of which follows, allows for a robust statistical assessment of the possibility that it is a combination of dynamical modes that produces pancontinental drought features. To do so, all pancontinental drought types are treated as the same, and considered to be Bernoulli processes (with 1 for drought years and 0 for non-drought years), with the drought frequency then defined as the number of pancontinental drought occurrences over the number of analyzed years (152 years for the observation-to-reconstruction). Within a Bayesian framework, the posterior distribution of

the drought frequency can be calculated for subsets of the data that have different phases of the dynamic modes (e.g., a negative or La Niña-like state in the Niño3.4 index) or some combination of phases of the dynamic modes (e.g., a negative Niño3.4 index, positive AMO, and negative PDO). If, following Kam et al. (2014), we assume that the prior distribution is a uniform beta distribution or uninformative, then the posterior distribution is easily derived with the alpha and beta parameters being equal to the number of drought occurrences plus one and the number of years minus the number of drought occurrences plus one, respectively. The observation-to-reconstruction posterior distributions in the right-hand panel of Figure 6.7 indicate that the frequency of pan-continental drought occurrence is greatest when there are simultaneously negative Niño3.4 and PDO indices and a positive AMO index (with pancontinental drought occurring nearly 40% of the time when these conditions are met). Interestingly, for the observation-to-reconstruction record the individual impacts of the three modes of variability on the frequency of pancontinental drought are roughly equal.

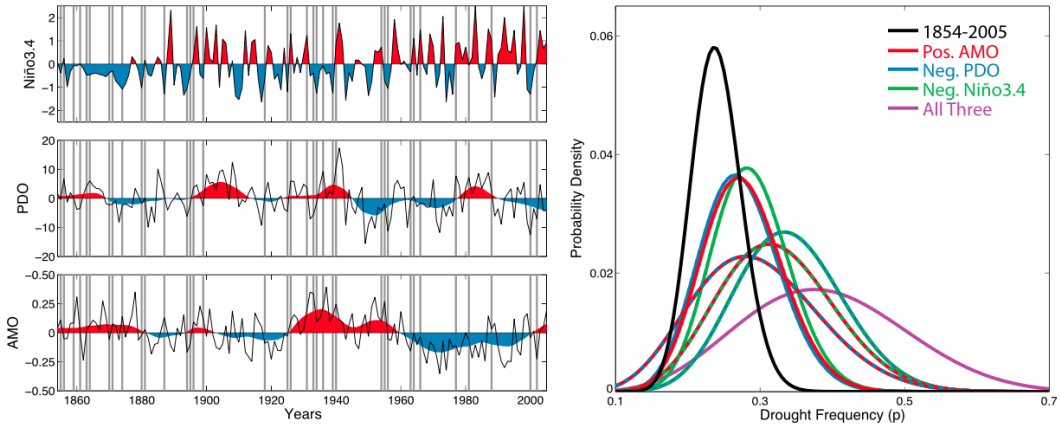

Figure 6.7: (left) The observed DJF Niño3.4, DJF PDO, and JJA AMO indices for the period 1854–2005 C.E. are plotted as solid black lines. For the PDO and AMO, the filled regions (red for positive, blue for negative) are the smoothed time series using a 10-year LOWESS spline, while for the Niño3.4 index the filled regions are the unfiltered interannual data. The timing of each pancontinental drought occurrence is indicated with a gray bar (all five types of pancontinental drought are considered together). (right) The posterior distribution of the frequency of pancontinental drought occurrence (all types considered together) for the full data (black) and for the subset of data with a positive AMO (red), negative PDO (blue), or negative Niño3.4 (green) index and years with combinations of two or all three of these conditions. The distributions for combinations of two conditions are dashed using the two respective colors while the distribution for the all three conditions is plotted in purple.

6.1.7 Simulated Dynamical Characterisitics

The roughly equal impact of the ENSO, PDO and AMO on the frequency of pancontinental drought occurrence over the instrumental interval (Figure 6.7) suggests a need to better understand the simulated characteristics of these modes before assessing pancontinental drought dynamical drivers within the models. An assessment of the multidecadal character and stationarity of the ENSO teleconnection was completed in Chapter 4; in this section similar assessments will be completed but for all three modes together.

Figure 6.8 shows the teleconnection patterns calculated as the correlation between the Niño3.4, PDO, and AMO indices and PDSI over NA. These patterns have been calculated for both the NADA and an observed PDSI dataset (Dai et al., 2004) during the overlapping period with the observed SST dataset (1854–2005 C.E. and 1950–2005 C.E., respectively), and for a sliding 152-year window (the length of the observation-to-reconstruction overlap) across the full control model simulations. The model pattern in Figure 6.8 plots the 152-year period in which the simulated teleconnection pattern best represents the observation-to-reconstruction pattern, as determined by the maximum CPCS between the two fields. The CPCS is a quantitative measure of the similarity of the simulated and observation-to-reconstruction teleconnection patterns, with the range in the CPCS for all of the 152-year periods in the models being a measure of the stationarity of that simulated teleconnection (Figure 6.8, middle). Additionally, the bottom panel of Figure 6.8 shows the strength of the ENSO, PDO, and AMO teleconnections. To do so, the sum of the squared teleconnection correlation coefficients was calculated for each of the model segments and the range in these values was then plotted as a boxplot. For comparison, the sum of the squared teleconnection correlation coefficients was also calculated for the full observation-to-reconstruction and observational records. This analysis was limited to the grid points common to each dataset over the plotted NA domain in the top panels of Figure 6.8.

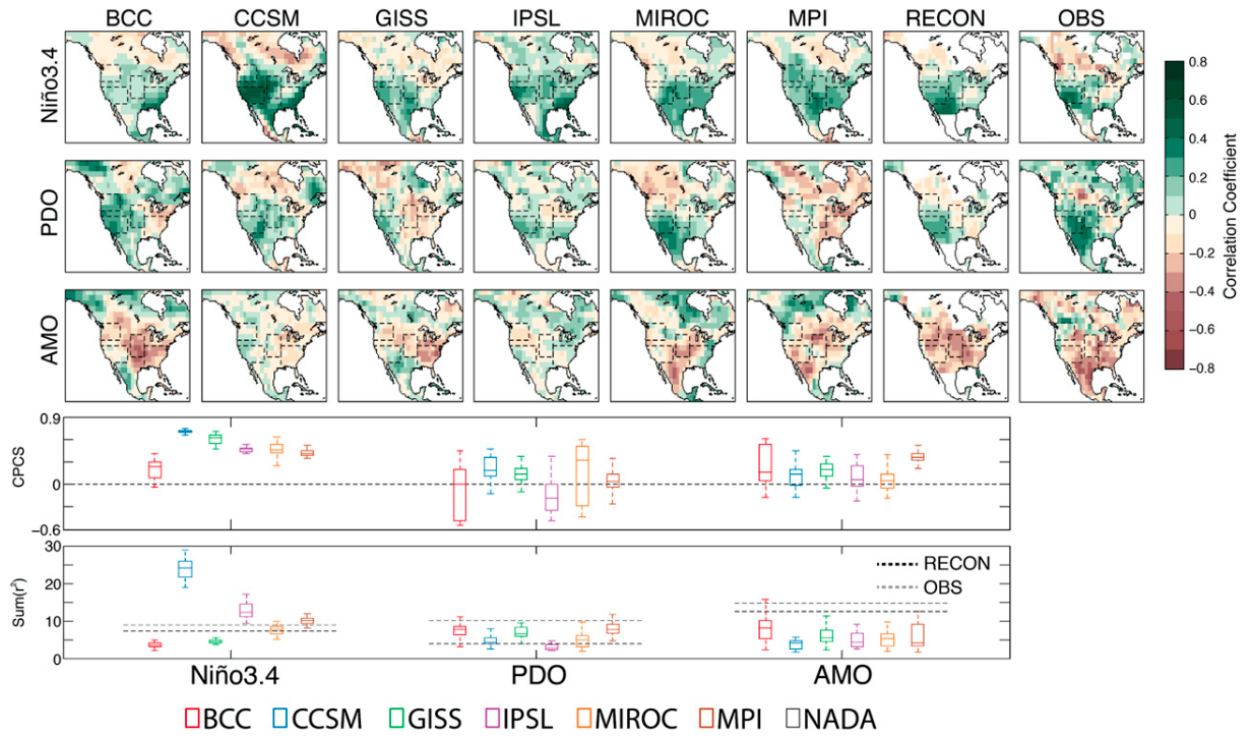

Figure 6.8: Correlations between gridpoint PDSI from the NADA or models and the (top) DJF Niño3.4 index, (middle) DJF PDO index, and (bottom) JJA AMO index. For the PDO and AMO, correlations are based on filtered [(10-year locally weighted scatterplot smoothing (LOWESS)] PDSI and climate indices. The observation-to-reconstruction correlations (RECON) are from the overlapping period (1854–2005 C.E.) between the NADA and the observed SST dataset (Smith & Reynolds, 2003) and the observed correlations (OBS) are from the 1950–2005 C.E. period in an observed PDSI dataset (Dai et al., 2004) and the same SST dataset. For the models, the teleconnection pattern was calculated for a sliding 152-year window (the length of the observed record). The plotted pattern is the 152-year segment with the teleconnection pattern that best matches the observation-to-reconstruction pattern as determined by the CPCS between the two fields. The upper boxplot shows the range in CPCS between the model pattern for each 152-year segment and the observation-to-reconstruction pattern. The bottom box plot shows the range in the sum of squared correlation coefficients over NA for the model segments with the value from the observations and observation-to-reconstruction record plotted as dashed gray and black lines, respectively.

The observation-to-reconstruction ENSO and AMO dynamics are largely characteristic of those in the observed PDSI dataset with CPCS values between the patterns of 0.75 and 0.50 and of nearly equal strengths. The PDO teleconnection, however, is significantly weaker in the reconstruction, despite having a similar spatial pattern (CPCS of 0.52). While this may suggest a deficiency in the reconstruction, it is more likely indicative of an inconsistent impact of the PDO over the much longer reconstructed record (152 versus 56 years for the

observed PDSI). In fact, while the ENSO behavior appears to be consistent throughout the instrumental interval in the left hand panel of Figure 6.8, the variability in the early part of the PDO and AMO records is subdued.

The models are able to simulate 152-year periods that have a realistic ENSO teleconnection pattern to NA (with the exception of BCC); however the strength of this teleconnection varies greatly, with CCSM having far too strong of a teleconnection and BCC and GISS having an ENSO teleconnection that is too weak. The stationarity of this teleconnection, likewise, varies significantly between the models; the CCSM ENSO teleconnection (as seen in Chapters 4 and 5), for instance, is highly stationary while the ENSO teleconnections in BCC and MIROC are highly nonstationary. The AMO and PDO teleconnections in the models are much less realistic, with none of the models simulating a 152-year period with a CPCS value over 0.6 and the teleconnection strength being weaker than the observations for each model and both modes. These teleconnections are also nonstationary, with the largest CPCS range occurring in MIROC for the PDO and BCC for the AMO, but with a CPCS range of at least 0.4 for all of the models.

Figure 6.9 shows the range in the CPCS between simulated spatial patterns calculated for a sliding 152-year window (length of the observed SST dataset) across the full control model simulations and the observed spatial patterns. As suggested by the teleconnections, models are generally successful at simulating a reasonable ENSO spatial pattern (with the highest pattern correlation values of the three modes). Interestingly, the simulated PDO and AMO behavior is largely consistent between the models with a highly nonstationary, but at times realistic, PDO pattern (every model simulates a PDO pattern CPCS of at least 0.6), and a more stationary, but generally unrealistic, AMO pattern (Figure 6.9). In both cases, however, the PDO and AMO patterns in the models are less characteristic of the observed patterns than for ENSO.

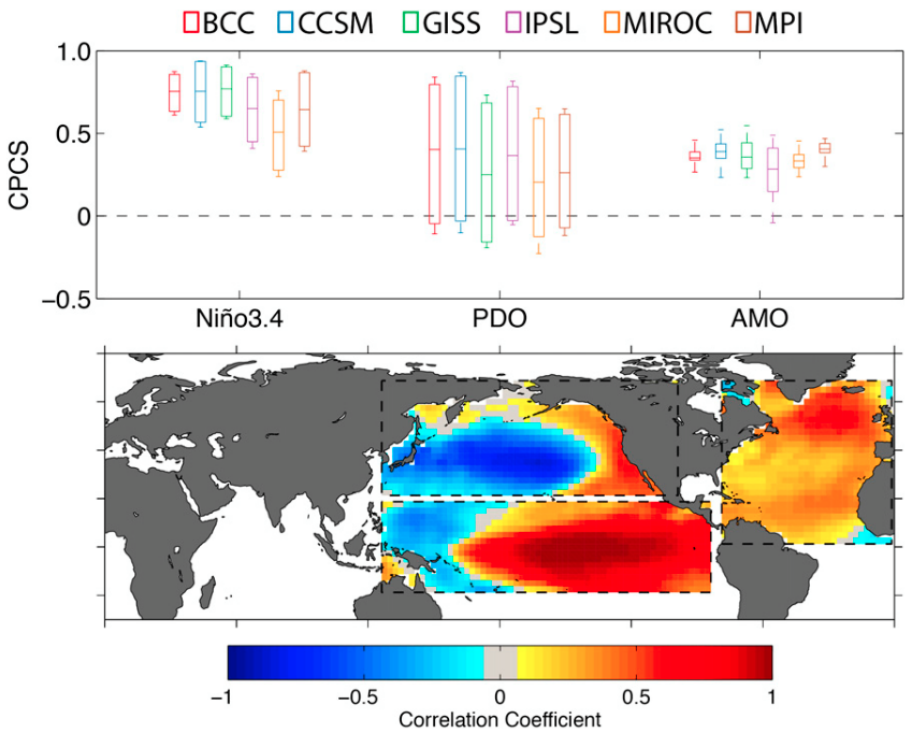

Figure 6.9: (top) The range in the CPCS between the simulated ENSO, PDO, and AMO spatial patterns calculated for a sliding 152-year window (length of the observed SST dataset) across the full model simulations and the observed spatial patterns. (bottom) The observed target patterns. The plotted domain is longitudinally global beginning at 0° and spans the latitudes 30°S–80°N. The boxes over which the CPCS values were calculated for each region are designated by the black dashed lines.

In aggregate, the models exhibit different teleconnections between the oceanic boundary conditions and NA, with no individual model matching the observed atmosphere-ocean dynamics particularly well. Together, this suggests that models are not likely to agree on the modes of atmosphere-ocean variability that are associated with pancontinental drought. This was also true of megadroughts in Chapter 5, and these additional dynamical characterizations may help explain the range in model behavior. Additionally, the models have a stronger and more realistic ENSO and associated teleconnections, as compared to the PDO and AMO and are therefore expected to be more successful at simulating the pancontinental drought dynamics associated with this mode of variability. Nevertheless, the simulated dynamical relationships are largely nonstationary, and the observed dynamics have been inferred from the short 152-year instrumental interval. The observed dynamics, thus, may

themselves be time variable or inadequately characterized (particularly given the large persistence and consequently the small number of degrees of freedom for the PDO and AMO). It is therefore difficult to attribute differences between the models and observations as solely associated with the model characteristics, as opposed to some combination of model misrepresentations and poorly characterized observational teleconnections due to undersampling of low-frequency modes and nonstationarity.

6.1.8 Simulated Pancontinetal Drought Dynamics

Figure 6.10 shows the posterior distributions for frequency of pancontinental drought occurrence over the full 500 years of the control simulations. The models tend to overestimate the impact of ENSO on pancontinental drought occurrence (with the main exception being BCC — Figure 6.10 versus 6.7). This result is likely indicative of the more realistic, and in some cases overactive, ENSO variability and teleconnections (e.g., CCSM — Sections 2.6.2 and 6.1.7) relative to other modes of coupled atmosphere-ocean variability. The model split between slightly underestimating the recurrence interval of pancontinental drought of all types (CCSM, IPSL, and MPI) and moderately overestimating the recurrence interval of these droughts (BCC, GISS, and MIROC) in Figure 6.3 can potentially be explained by this result. CCSM, IPSL, and MPI all greatly overestimate the impact of ENSO on the frequency of pancontinental drought occurrence and, as a consequence, produce more of these features than is realistic. In CCSM this behavior appears to result from ENSO variability that is too strong (Figures 2.6 and 2.9), while in IPSL and MPI the ENSO variability is more realistic (though slightly too strong — Figure 2.9) but the hydroclimate response to ENSO is too homogenous over the NA continent (Figure 6.8). BCC, despite underestimating the impact of ENSO on pancontinental drought occurrence, is able to largely reproduce the impact of the AMO, while slightly overestimating the PDO impact, and has a posterior distribution of ocean-forced pancontinental drought occurrence (Figure 6.10) that is similar to the observation-to-reconstruction (Figure 6.7). The same is true of GISS, which

exhibits the most realistic impact (as compared to the observations) of the three modes of atmosphere-ocean variability (and the oceanic boundary conditions in general) on pancontinental drought occurrence (although it slightly underestimates the AMO impact relative to the PDO). The fact that GISS, and to a lesser degree BCC, underestimate the overall occurrence of pancontinental drought (e.g., Figure 6.3), therefore, appears to be related to the frequency with which the simulated ocean produces a simultaneously positive AMO, negative PDO, and negative ENSO. MIROC also underestimates the frequency of pancontinental drought occurrence, and while it simulates a reasonable impact of a negative Niño3.4 index on the frequency of pancontinental drought occurrence, the PDO and AMO impacts are too weak (Figure 6.10).

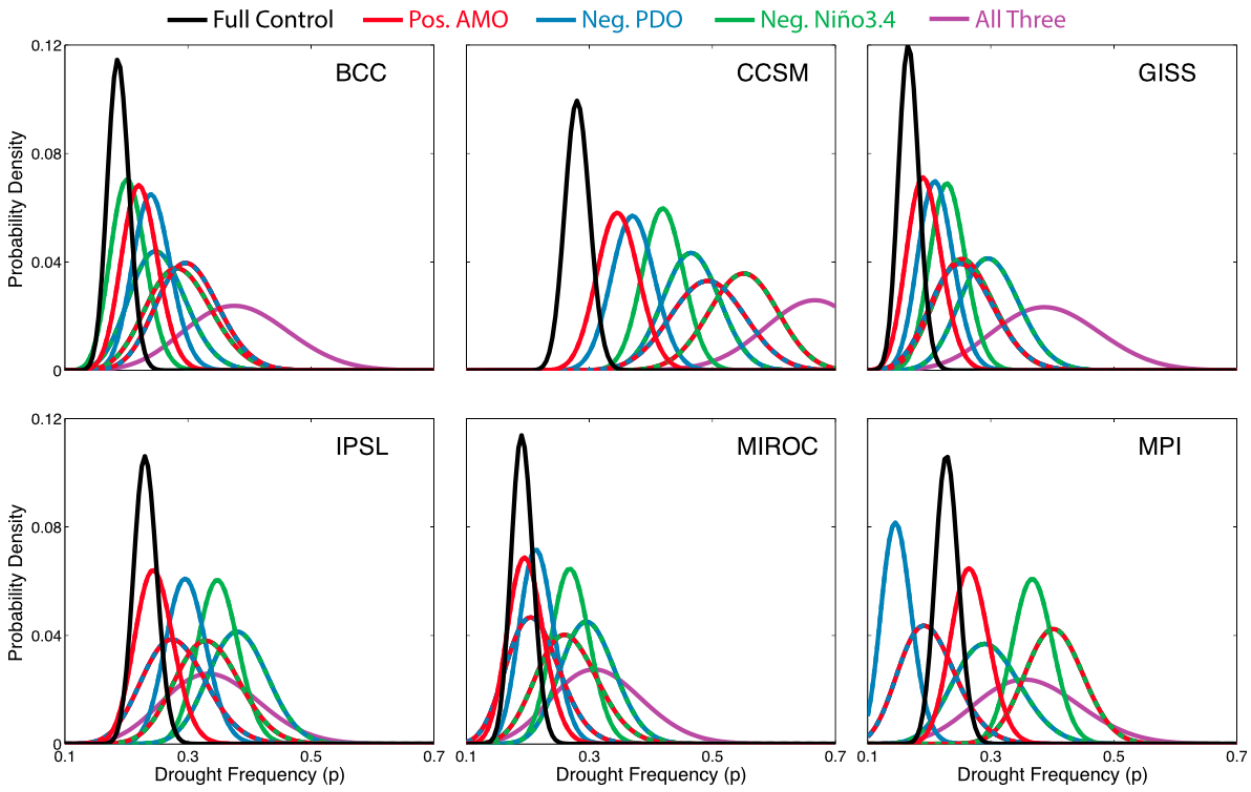

Figure 6.10: Posterior distributions for each model of the frequency of pancontinental drought occurrence (all types considered together) for the full data (black) and for the subset of data with a positive AMO (red), negative PDO (blue), or negative Niño3.4 (green) index and years with combinations of two or all three of these conditions. The distributions for combinations of two conditions are dashed using the two respective colors while the distribution for the combination of all three conditions is plotted in purple.

It must be noted that because of the short length of the instrumental record, which limits our knowledge of real-world pancontinental drought dynamics, it is difficult to make conclusions about the veracity of the simulated dynamics. Nevertheless, attempting to understand the simulated pancontinental drought dynamics within the context of the characteristic model behavior outlined in Section 6.1.7 may help determine if models will be able to properly constrain the risk of future drought over NA. In particular, the patterns of behavior of CCSM and BCC are an interesting juxtaposition of pancontinental drought dynamics. CCSM greatly overestimates the impact of ENSO on pancontinental drought occurrence (Figure 6.10), while BCC underestimates (Figure 6.10). This behavior can perhaps be understood in terms of the model dynamics outlined in Section 6.1.7. While BCC has a somewhat realistic ENSO spatial pattern (Figure 6.9), and variability that is moderate (but too regular, e.g., the large negative lag-1 autocorrelation value; see Figure 2.6), the ENSO teleconnection to NA is the least realistic, weakest, and most nonstationary of the models analyzed herein (Figure 6.8). By contrast, the PDO and AMO teleconnections are more realistic, stronger (Figure 6.8), and consequently more strongly connected to pancontinental drought (Figure 6.10). CCSM, on the other hand, has a very realistic and stationary ENSO teleconnection (Figure 6.8 and Chapters 4 and 5), along with ENSO variability and spatial patterns that are too strong (Figures 2.6 and 2.9). As a consequence pancontinental drought is consistently connected to the tropical Pacific Ocean. The same characteristics were used to explain the association between megadroughts and ENSO in CCSM (Chapter 5).

6.1.9 Conclusions

Simulated ENSO, PDO, and AMO dynamics, and their teleconnections to NA, differ between models and in their comparisons to observations. As a consequence, and similar to earlier findings for megadroughts (Chapter 5), models do not agree on the modes of atmosphere-ocean variability that are associated with pancontinental drought. The models do, however, simulate pancontinental droughts with the frequency and spatial patterns

exhibited by the NADA. Additionally, the models display centennial-scale variability in the occurrence of pancontinental drought that is similar to the magnitude observed in the NADA. These changes do not appear to be tied to the exogenous forcing, suggesting that simulated internal hydroclimate variability on these timescales is large in magnitude.

These results have implications for our understanding of megadroughts. Firstly, the preponderance of pancontinental drought during the megadroughts in the NADA (Section 6.1.3) and the observed dynamics of pancontinental drought (Section 6.1.6) suggest a role for multiple modes of atmosphere-ocean variability in driving past megadroughts. In particular, the percentage of megadrought years that are pancontinental is 37% as compared to 20% for all other years between 850–2005 C.E. (Figure 6.1). Figure 6.7 suggests that the percentage of years that have pancontinental drought increases from approximately 20% to nearly 40% when there are simultaneously negative states of the ENSO and PDO and a positive state of the AMO. While the close association of these values provides no proof of causation, it appears possible that the increase in the frequency of pancontinetal drought occurrence during megadroughts is a consequence of these features being driven by a combination of the three modal states. Importantly, this interpretation is consistent with other paleoclimate and modeling studies that suggest that the MCA, the period with the greatest incidence of megadroughts, was characterized by a negative PDO (e.g. MacDonald & Case, 2005) and ENSO (e.g. Mann et al., 2009) and a positive AMO (e.g. Feng et al., 2008), with the combined atmosphere-ocean state argued for by Seager et al. (2007).

The behavior of the models is also interesting. In CCSM, for instance, megadroughts are consistently driven by the tropical Pacific boundary conditions (Chapter 5). This appears to result from the strong and stationary teleconnection between the tropical Pacific and NA and the large variability in the tropical Pacific Ocean (likely too large — Section 2.6.2) in CCSM. These characteristics also appear to impact the simulation of pancontinental drought, with CCSM greatly exaggerating the impact of the tropical Pacific Ocean on the frequency of pancontinental drought occurrence (Section 6.1.8). Given the interpretation

of the NADA, the observations given above and the model characterizations in Figure 6.10 (specifically the impact of a negative ENSO state), we would expect megadroughts in CCSM to be pancontinental approximately 45% of the time (because they are consistently driven by the tropical Pacific Ocean). Nevertheless, the actual value is 33% relative to 25% for all years between 850–2005 C.E. (Figure 6.1). This may indicate that other atmosphere-ocean dynamics are also at play during megadroughts in CCSM. There is, for instance, a weak but insignificant tendency towards negative AMO during megadroughts in the model (Chapter 5), which would decrease the frequency of pan-continental drought occurrence.

6.2 Seasonality

6.2.1 Motivation and Questions

In Chapters 3 and 5 megadroughts in CGCMs were shown to consistently result from anomalously low winter precipitation. The NADA does not provide information on the seasonality of precipitation signals, nevertheless research has demonstrated that reconstructed PDSI in the ASW predominantly reflects winter moisture conditions (St. George et al., 2010). This suggests that similar to the models, megadroughts identified in the NADA result from anomalously low winter precipitation. Nevertheless, some areas of the ASW have a dual-season precipitation signal: winter precipitation occurs within transient midlatitude eddies, while summer precipitation is controlled by the NAM. The NAM provides critical moisture relief during winter drought years. Consequently, if megadroughts are characterized by precipitation deficits occurring in both the winter and summer seasons, i.e. dual-season drought, this would further impact an already vulnerable region. The phasing of winter and summer precipitation variability in the ASW, and the specific role played by the NAM in that phasing, is therefore important to understand and characterize.

The instrumental interval is marked by a relatively high occurrence of out-of-phase winter-to-summer precipitation anomalies in the ASW (e.g. Griffin et al., 2013), and there

is dendroclimatic evidence that anti-phasing of precipitation extremes may be a consistent feature of the last millennium (Stahle et al., 2009). Out-of-phase winter-to-summer precipitation would suggest a limited risk of dual-season drought on interannual and longer timescales. Nevertheless, a recent reconstruction of NAM variability using tree-ring records of latewood width has established that the latter half of the 20th century exhibits potentially anomalous NAM behavior with regard to the prevalence of out-of-phase seasonal precipitation anomalies (Griffin et al., 2013). The 20th century, therefore, may not be a characteristic period for defining the NAM precipitation climatology, its relationship to the winter climate regime, and the potential connections to the coupled atmosphere-ocean system. Our investigation herein builds off the analyses of Griffin et al. (2013) using coupled model simulations to further assess assumptions about the stationarity of seasonal precipitation phasing relationships in the ASW. We use independent tree-ring based reconstructions of NAM and winter precipitation variability (Griffin et al., 2013) in the NAM2 region (113.25°W—107.75°W, 30°N—35.25°N — Gochis et al., 2009) for the period 1539–2008 C.E. as the basis for comparisons to the NAM dynamics in CMIP5/PMIP3 simulations. Four fundamental questions are addressed. 1) Are the teleconnections between the reconstruction and the tropical Pacific Ocean over the instrumental interval consistent with the lack of systematic in- or out-of-phase seasonal precipitation (Section 6.2.2)? 2) Is there a seasonal precipitation phasing relationship, of either sign, in the models over the whole record or for shorter periods (e.g. the period with predominantly out-of-phase seasonal precipitation anomalies in the latter part of the instrumental record — Section 6.2.4, Part 1)? 3) Are the model dynamics in agreement with the reconstruction and observations, and are these consistent with the simulated seasonal precipitation phasing relationships (Section 6.2.4, Parts 2 and 3)? And 4) Do models produce periods with predominantly in-phase winter-to-summer precipitation anomalies that lead to dual-season drought on interannual or longer timescales (Section 6.2.5)? The answers to these questions will clarify our understanding of seasonal precipitation phasing in the ASW and the seasonality of megadroughts, while potentially elucidating the dynamics responsible

for the real-world and simulated phasing behavior.

6.2.2 Reconstruction Dynamics and Phasing

Griffin et al. (2013) note that the number of years with in- and out-of-phase seasonal precipitation anomalies are approximately equal over the length of their reconstruction and, on that basis, they declare that there is no systematic seasonal precipitation phasing relationship in the NAM2 region. The reconstructed SPI record, however, is punctuated by shorter periods when out-of-phase events congregate (most notably in the mid-to-late 20th century), as well as periods with predominantly in-phase seasonal precipitation anomalies (the beginning of the 20th century). In both cases these are significant against the null hypothesis that the phasing could occur randomly (not shown), which suggests that there are atmosphere-ocean dynamical associations underlying the most in- and out-of-phase periods in the reconstruction. There are a number of dynamics that have been implicated as having the potential to drive seasonal precipitation phasing, specifically the out-of-phase winter-to-summer precipitation anomalies in latter part of the instrumental interval. These include: 1) opposite-sign winter and summer teleconnections tied to same-sign winter and summer SST anomalies (e.g. Castro et al., 2001); 2) a winter-to-summer shift in tropical Pacific SSTs and a same-sign winter and summer teleconnection (e.g. Seager et al., 2009); and 3) land-surface feedbacks, for instance Notaro & Zarrin (2011) demonstrate that deep Rocky Mountain snowpack tends to hinder the poleward advance of the summer monsoon, and associated rainfall, into the ASW (for the relationship between antecedent winter moisture on the summer monsoon see also Gutzler, 2000; Higgins & Shi, 2000; Zhu et al., 2005). To determine which, if any, of these dynamics are consistent with the SPI reconstructions of Griffin et al. (2013), the relationship between the tropical Pacific Ocean and hydroclimate over the NAM2 region will be analyzed using an instrumental SST dataset and the overlapping period in the SPI reconstructions (1856–2005 C.E. — as in the previous section hereinafter this will be referred to as observation-to-reconstruction). We do not make an

explicit attempt to analyze land-surface feedbacks (point 3), but it is worth noting that these processes are expected to be present in the observational and reconstructed data and are not separable from the observation-to-reconstruction teleconnection dynamics analyzed herein. Additionally, we do not analyze potential drivers of seasonal precipitation phasing that receive less attention in the literature, for instance forcing from tropical or extratropical Atlantic SSTs (e.g. Kushnir et al., 2010).

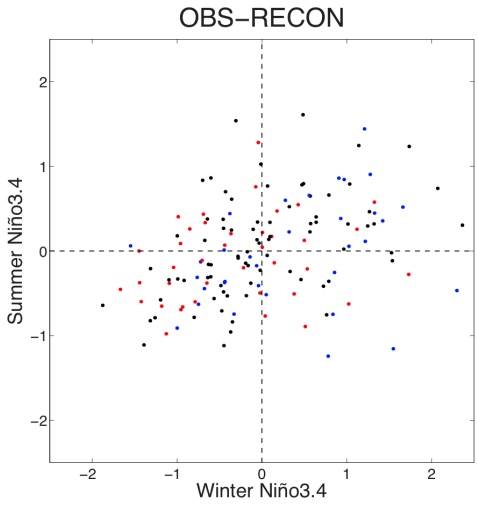

Figure 6.11: Winter and summer SST anomalies for the Niño3.4 region are plotted for the 1856–2005 C.E. period in the observed SST dataset (Kaplan et al., 1998). Years that correspond to in-phase wet precipitation are plotted in blue, in-phase dry precipitation are plotted in red and out-of-phase precipitation are plotted in black.

There is evidence that an evolution from El Niño to La Niña-like conditions going from winter to summer is possible (e.g. in 1998; see also Seager et al., 2009) but that tropical Pacific SST anomalies can also persist from winter to summer (e.g. Rasmusson & Carpenter, 1982). The seasonal evolution of tropical Pacific SST anomalies, along with the winter and summer teleconnections, will determine the impact of the tropical Pacific Ocean on seasonal precipitation phasing. Figure 6.11 plots the winter versus following summer tropical Pacific SST anomalies and indicates the seasonal precipitation phasing relationship in that year by the color of the marker. There is a slight positive relationship between winter and summer tropical Pacific SST anomalies, indicating a tendency for same-sign SST anomalies to persist from winter to summer. Nevertheless, this relationship is weak, with a squared Pearson's

correlation coefficient (R^2) of 0.13 when all values are considered. Additionally, the largely random scattering of in and out-of-phase years in the four quadrants of Figure 6.11 suggest a generally weak control of tropical Pacific SSTs on seasonal precipitation phasing. This is consistent with the lack of a systematic seasonal precipitation phasing relationship in the reconstruction (Griffin et al., 2013).

To explain the origin of the above demonstrated weak associations, Figure 6.12 characterizes the winter and summer teleconnections between SPI in the NAM2 region and the winter (DJF) and summer (JJA) SST fields for the 56 years (1950–2005 C.E.) that are common to the observed SST dataset (Kaplan et al., 1998), the reconstruction, and the period of good coverage over the NAM2 region in an observed precipitation dataset from the GPCC (GPCC — Becker et al., 2013, herinafter observed). The observation-to-reconstruction and observed teleconnections are in good agreement throughout the tropical and extratropical Pacific, with the exception of an area of positive correlation off the coast of western NA in summer that is only present in the observations. Importantly, in both cases the teleconnection patterns are of opposite-sign in winter and summer and of similar magnitude. The teleconnection dynamics, however, are complicated by the fact that the strength and character of the observation-to-reconstruction summer teleconnection varies over the full period of overlap between the reconstruction and SST dataset (1856–2005 C.E — Figure 6.13).

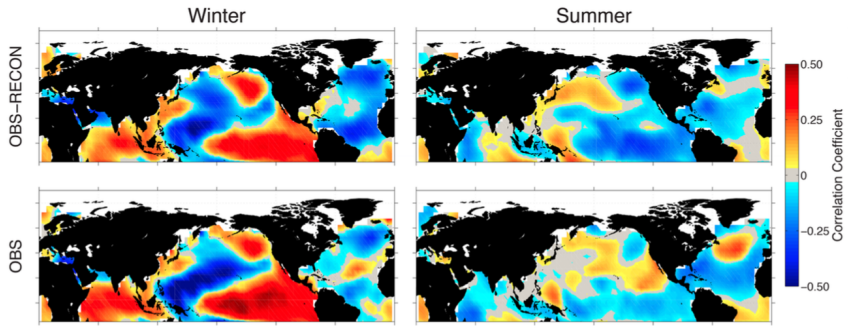

Figure 6.12: Maps of Pearson's correlation coefficients calculated between winter (DJF) or summer (JJA) SPI and SSTs. All results are shown for 1950-2005 C.E., the overlapping period of the reconstruction, the observed SST dataset (Kaplan et al., 1998) and the period of good coverage over the NAM2 region for the observed precipitation dataset (GPCC — Becker et al., 2013). The plotted domain is 180°W–180°E by 40°S–90°N.

Collectively, the seasonal evolution of tropical Pacific SSTs and the average teleconnections suggest a preference for out-of-phase seasonal precipitation (same-sign SST anomalies and opposite-sign teleconnections). Nevertheless, the summer teleconnection is potentially non-stationary (Figure 6.13) and the tropical Pacific Ocean exhibits only a weak tendency for same sign SST anomalies to persist from winter to summer (Figure 6.11). Together this makes a systematic out-of-phase seasonal precipitation relationship unlikely, which is consistent with the roughly equal probability of reconstructed seasonal precipitation anomalies being in- or out-of-phase in any given year (Griffin et al., 2013). Nevertheless, any nonstationarity of the summer teleconnection has the potential to produce shorter periods where the seasonal precipitation phasing relationship is more or less out-of-phase (e.g. more out-of-phase when the summer teleconnection to the tropical Pacific is particularly strong and negative as in the $< 5\%$ composite in Figure 6.13).

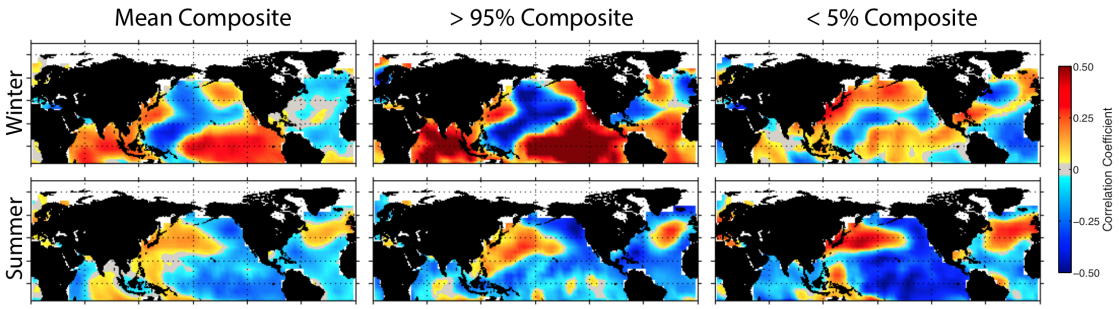

Figure 6.13: Mean Composite (left column) contains the average maps of Pearson's correlation coefficients calculated between winter (DJF) or summer (JJA) reconstructed SPI and observed SSTs (Kaplan et al., 1998) for random 30-year periods between 1856–2005 C.E. The $> 95\%$ Composite and $< 5\%$ Composite columns contain the 30-year segments with the greater than 95th percentile or less than 5th percentile of average correlation coefficients over the Niño3.4 region (170°W–120°W, 5°S–5°N). The plotted domain is 180°W–180°E by 40°S–90°N.

6.2.3 Do Models Have a NAM?

Before analyzing simulated seasonal precipitation phasing and the dynamics thereof, it is necessary to determine that the PMIP3 models simulate a NAM. To do so, the simulated precipitation climatologies and standard deviations over the NAM2 region are plotted

in Figure 6.14. Only the CCSM, MIROC, and MPI models simulate a realistic May–June climatological dry period followed by a substantial monsoon onset. The MPI and CCSM models have a particularly robust July–September precipitation peak with monsoon retreat by October. MIROC has a summer precipitation peak but the September maximum and wet October are not realistic. In contrast, BCC, IPSL, and GISS all lack any summer precipitation maximum. All of the model standard deviations are inflated relative to the observations.

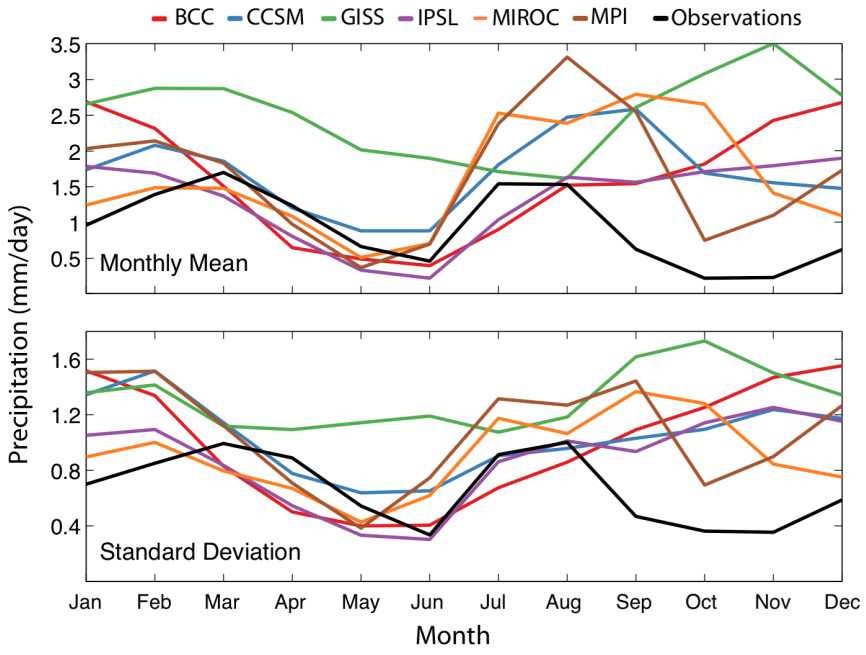

Figure 6.14: (top) The average monthly precipitation in the NAM2 region for the full simulations and observational data from the GPCC (1901–2010 C.E. — Becker et al., 2013). Bottom panel is the interannual standard deviation of monthly precipitation for all of the models and the observations.

For the purposes of analyzing winter-to-summer precipitation phasing relationships, only the CCSM and MPI simulations will be retained. While the MIROC model appears to have a NAM, the precipitation climatology is not as realistic as the CCSM and MPI models and the LM simulation has the aforementioned significant drift (Chapter 2 — Sueyoshi et al., 2013). CCSM and MPI are also the same models (of the LM simulation subset of CMIP5/PMIP3) that were determined to have a sufficiently realistic NAM for the projections of ASW monsoon rainfall in Cook & Seager (2013). Moreover, Langford et al. (2014)

provide a detailed analysis of the NAM dynamics in all of the CMIP5 models, and find a positive relationship between model resolution and the realism of NAM dynamics; CCSM and MPI are the two highest resolution simulations of the last millennium.

6.2.4 Seasonal Precipitation Phasing and the Model Dynamics

Here we analyze the seasonal precipitation phasing in the models (Part 1) and assess the consistency of this phasing with regard to the potential atmosphere-ocean dynamical influences on seasonal precipitation phasing outlined in Section 6.2.2 and the model specific dynamical characteristics (Parts 2 and 3). The limited model output prevents a full analysis of the presence of land-surface feedbacks (point 3 in Section 6.2.2), however, the potential biases in simulated snow physics (e.g. Foster et al., 1996), coarse model resolution preventing a realistic simulation of orographic features, and the non-dynamic land-surface and vegetation models in CCSM and MPI make a realistic role for simulated land-surface feedbacks unlikely.

Part 1: Seasonal Precipitation Phasing

Figure 6.15 presents scatter plots of winter and summer simulated SPI (1539–2005 C.E.) as a characterization of the winter-to-summer precipitation phasing relationships (Panel A). These indicate that similar to the reconstruction (Griffin et al., 2013) there is no systematic seasonal precipitation phasing relationship between winter and summer in the CCSM and MPI simulations (56% and 54% of years are in-phase, respectively).

Despite the fact that the models do not exhibit a systematic seasonal precipitation phasing relationship, the high occurrence of out-of-phase seasonal precipitation anomalies in the latter part of the instrumental record suggests that shorter periods may exhibit predominantly in- or out-of-phase seasonal precipitation anomalies. To evaluate this possibility in the models, the number of out-of-phase years was calculated for a sliding 30-year window in each dataset and plotted in Panel B of Figure 6.15 (following Griffin et al., 2013, hereinafter the count value). In contrast to both the instrumental data and the reconstruction,

the models do not simulate periods with seasonal precipitation anomalies that are predominantly out-of-phase. This is indicated by the fact that the number of out-of-phase years over the 30-year windows in Panel B of Figure 6.15 rarely, and never by a large margin, exceeds fifteen — the threshold that indicates a neutral relationship between winter and summer precipitation anomalies. The models do, however, have multiple periods with predominantly in-phase winter and summer SPI anomalies (e.g. the 30-year period beginning in 1690 in CCSM and 1680 in MPI).

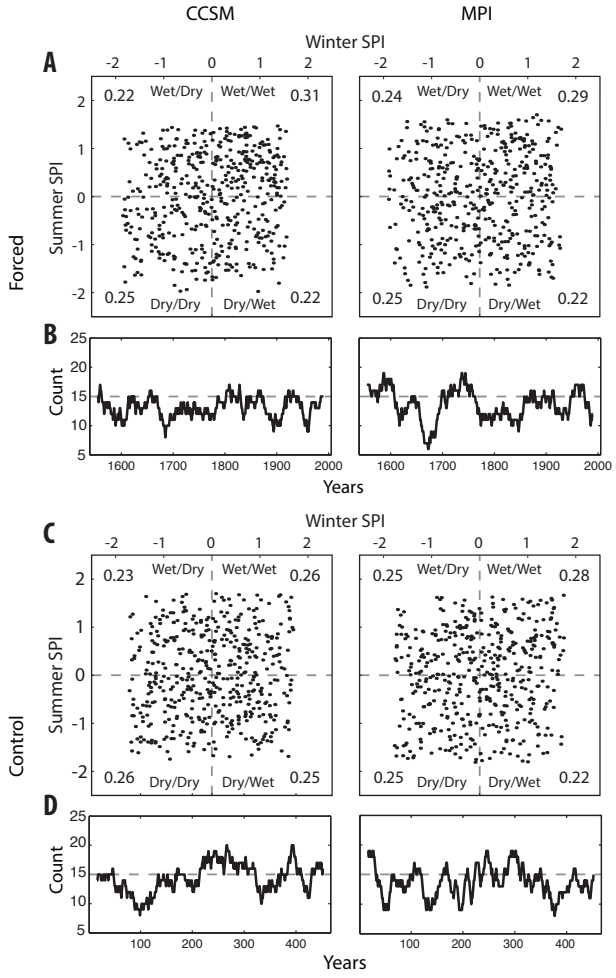

Figure 6.15: Scatter plots of simulated SPI for the winter (October to April) and summer (June to August) seasons over the period 1539–2005 C.E. (Panel A), with the fraction of values in each quadrant listed in each quadrant box. (Panel B) 30-year running count of opposing-sign winter and summer SPI anomalies. The dashed line is the threshold that indicates a neutral relationship between winter and summer precipitation anomalies. (Panels C and D) Same plots for control runs from these models.

To test the significance of the in-phase periods in the models against the null-hypothesis that this phasing can occur randomly, a 50,000-year autocorrelation- and distribution-preserving surrogate timeseries was created for both the winter and summer SPI from each dataset. The number of years with out-of-phase anomalies for each 30-year period in the surrogate timeseries was counted and the upper and lower 99th percentile of these values were chosen as the significance threshold. These bounds were 21 and 9 in each model, indicating out-of-phase significance against the null hypothesis for 30-year count values above 21 and in-phase significance for 30-year count values below 9. Multiple count values fall below the lower bound of the significance threshold, indicating that there are in-phase periods in both model simulations that would not be expected to occur by chance alone. Because these in-phase periods cannot be explained by random chance, there may instead be atmosphere-ocean dynamical associations in the models that underlie their origin.

Part 2: Simulated Seasonal ENSO Evolution

The impact of the tropical Pacific Ocean on seasonal precipitation phasing will depend on whether same-sign SST anomalies persist from winter to summer (e.g. Rasmusson & Carpenter, 1982, an evolution from El Niño to La Niña-like conditions going from winter to summer is also possible, for instance, in 1998). To assess the probability of same-sign SST anomalies occurring in winter and summer, Figure 6.16 shows a centered 30-year running count (with 30-years chosen to match the assessment of seasonal precipitation phasing in Griffin et al., 2013, and above) of same-sign winter-to-summer SST anomalies in the Niño3.4 region (170°W–120°W, 5°S–5°N). If the values in Figure 6.16 are at fifteen (the dashed line), the probability of SST anomalies persisting and changing sign between winter and summer are equal (greater than fifteen indicates a preference for SST anomalies to persist between winter and summer). The CCSM model exhibits a weak preference for the persistence of tropical Pacific SST anomalies from winter to summer (count values just above fifteen — Figure 6.16). In contrast, the MPI model has consistently high count values (Figure 6.16),

suggesting that the persistence of same-sign tropical Pacific SST anomalies from winter-to-summer will occur more frequently relative to CCSM or the observations (the average count for the observations is approximately 19 — see also Figure 6.11). The discrepancy between the two models is potentially related to their representation of ENSO. The CCSM model, for instance, has a stronger and more regular ENSO (Chapters 2, 4, 5 and Section 6.1), although both models, and these specific simulations, have well-validated and realistic ENSO (Chapters 2 and 4 and Section 6.1). In summary, both models exhibit tropical Pacific SST anomalies that tend to persist from winter to summer, although this behavior is stronger in MPI relative to both CCSM and the observations.

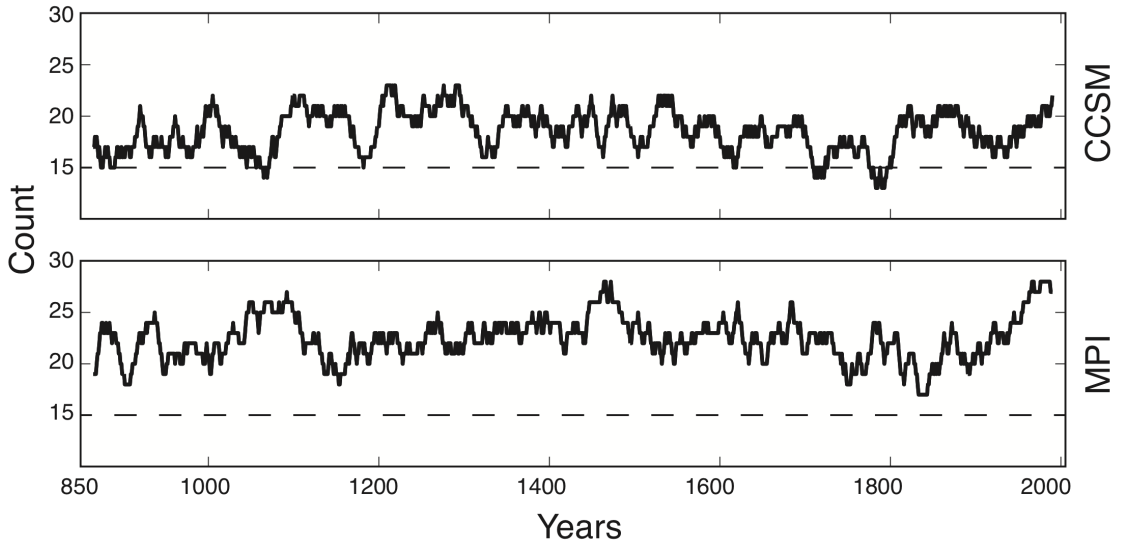

Figure 6.16: The time history of the winter-to-summer SST anomalies in the Niño3.4 region (170°W–120°W, 5°S–5°N). The black line represents a centered 30-year running count of same-sign winter and summer SPI anomalies. The dashed line is the threshold that indicates a neutral relationship between winter and summer SST anomalies.

Part 3: Simulated Teleconnections

While the winter teleconnection between the ASW and tropical Pacific for these models is characterized in Chapters 4 and 5 and Section 6.1.7, herein we additionally compare the winter teleconnection to that of summer specifically for the NAM2 subset of the full ASW. In both models, the winter teleconnection to the NAM2 region is positive and characteristic of

the observed teleconnection in sign, magnitude and spatial features (Figure 6.17). The MPI model exhibits a moderately negative summer teleconnection between NAM2 SPI and the tropical Pacific that is again largely characteristic of the observation-to-reconstruction and observed summer teleconnections (Figure 6.17 versus 6.11). In contrast to the observation-to-reconstruction and MPI dynamics, the CCSM model exhibits a weakly positive summer teleconnection (Figure 6.17). This is of the same sign as the winter teleconnection in the CCSM model, which exhibits winter precipitation variability that is tightly coupled to the tropical Pacific on both interannual and longer timescales (Chapters 4 and 5 and Section 6.1.7).

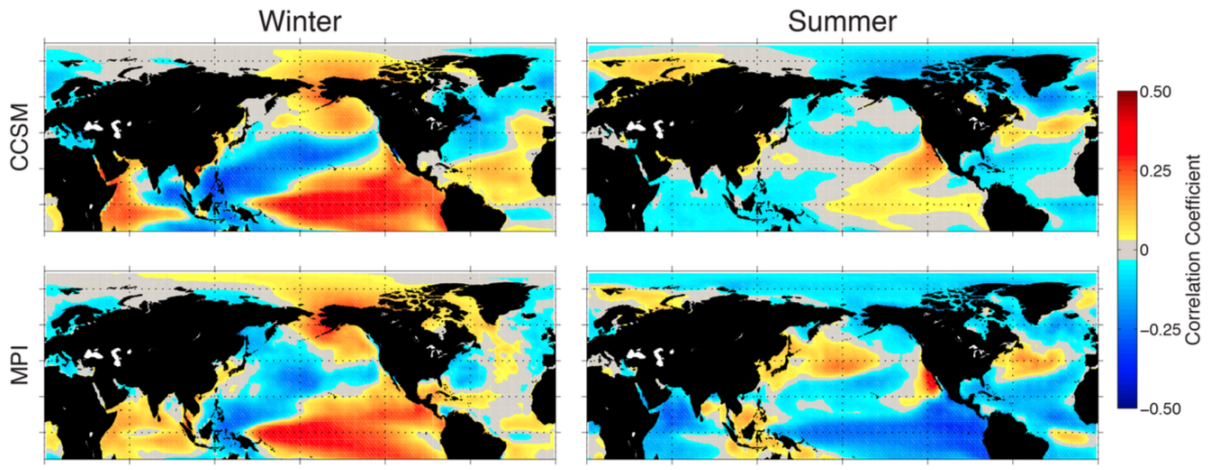

Figure 6.17: The same as Figure 6.12 but over the full length of the CCSM and MPI simulations. The plotted domain is 180°W–180°E by 40°S–90°N.

Figure 6.18 assesses the simulated teleconnection stationarity, defined as in Chapter 4, but again for both the winter and summer seasons. The analysis indicates that while the CCSM winter teleconnection is highly stationary (Chapter 4), the summer teleconnection is not. Neither the winter nor summer teleconnections are stationary through time in MPI, and more generally ASW hydroclimate is less tightly coupled to the tropical Pacific in MPI relative to the CCSM model (Chapter 5).

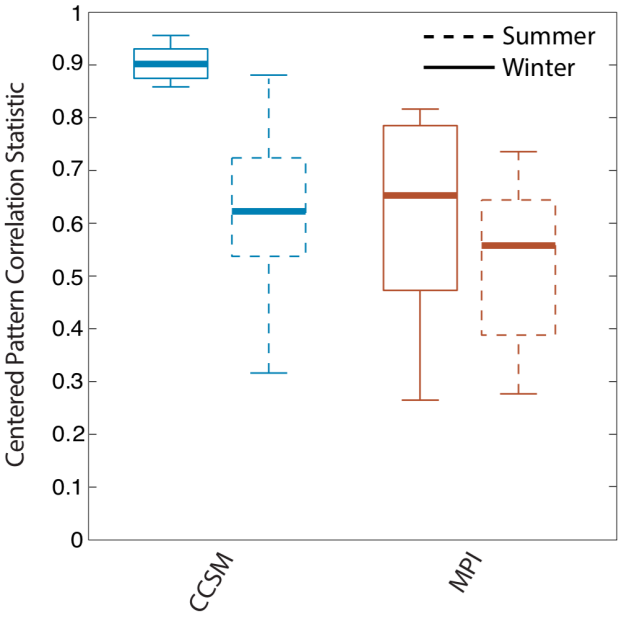

Figure 6.18: Winter (DJF) and summer (JJA) teleconnection stationarity defined as in Chapter 4. Box plots indicate the 75th and 25th percentile of the CPCS statistic across the segments in the respective coupled model runs with the median as the bolded line and the whiskers showing the full data excluding outliers.

Part 4: Dynamical Conclusions

We now summarize the dynamics for each model and how they relate to the lack of a systematic seasonal precipitation phasing relationship, while in the next paragraph we reconcile these dynamics with the shorter periods of significantly in-phase seasonal precipitation anomalies (Part 1). CCSM exhibits positive winter and summer teleconnections. These teleconnection characteristics suggest that in-phase seasonal precipitation anomalies are more likely to occur. The weak average magnitude and nonstationarity of the summer teleconnection in CCSM (Part 3), as well as the weak tendency for tropical Pacific SSTs to persist from winter to summer (Part 2), however, make seasonal precipitation phasing that is systematically in-phase unlikely. In MPI, the opposite-sign winter and summer teleconnections suggest that out-of-phase seasonal precipitation anomalies should occur with a higher probability. Such phasing is made less likely, however, due to the highly non-stationary teleconnections in MPI (Part 3), and generally weaker control of the tropical Pacific on NA hydroclimate in the model (Chapters 4 and 5 and Section 6.1.7).

The presence of shorter periods that are significantly in-phase in the MPI simulation (Part 1) is surprising given the winter and summer teleconnection characteristics outlined in Parts 2 and 3 of this section. The MPI model, nevertheless, has a high degree of non-stationarity in its dynamical relationships. The periods of predominantly in-phase seasonal precipitation anomalies may be indicative of the importance of this nonstationarity, with the tropical Pacific influence on the ASW either weakening enough to allow other atmosphere-ocean dynamics to dominate the precipitation phasing relationship (e.g. tropical or extra-tropical Atlantic SSTs), or changing such that the tropical Pacific actually makes in-phase seasonal precipitation anomalies more likely than out-of-phase. Analysis of the 5% of 30-year periods with the most in-phase seasonal precipitation suggests a robust weakening of the summer teleconnection, consistent with this interpretation (not shown). The periods of significantly in-phase seasonal precipitation in the CCSM model are consistent with the teleconnection and ENSO behavior outlined in Parts 2 and 3 of this section. Nevertheless, this phasing relationship might be expected to be stronger given a more stationary summer teleconnection or a greater frequency of same-sign tropical Pacific SST anomalies persisting from winter-to-summer simulated within CCSM. It is additionally worth noting that the model behavior outlined in this section does not appear to be dependent on the forcing — control simulations from the same models reproduce approximately the same phasing characteristics (Panels C and D of Figure 6.15).

6.2.5 Dual-Season Droughts and Megadroughts

The periods with a significant number of in-phase winter-to-summer precipitation anomalies in the models and reconstruction (Part 1 of Section 6.2.4 and Section 6.2.2, respectively) are suggestive of a potential for more frequent in-phase dry or dual-season drought years (defined as having winter and summer precipitation below the mean). This is only weakly true of the data analyzed herein, with in-phase dry years, or dual-season drought, occurring 28, 30 and 27 percent of the time (in CCSM, MPI and the reconstruction, respec-

tively) in the 30-year periods that fall above the 95th percentile for number of years with in-phase seasonal precipitation anomalies. These values are 25, 25 and 22 percent when all 30-year periods are considered.

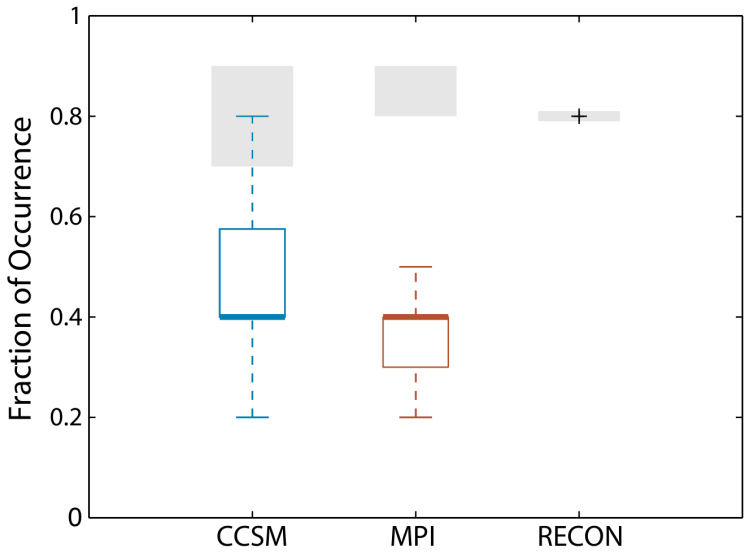

Figure 6.19: Fraction of the ten highest-ranking winter and summer droughts that are contemporaneous in time for the full reconstruction and for a sliding 467-year (length of reconstruction) window across the full 1156-year model record. The gray shaded region is the 99% confidence interval for these values as determined by an autocorrelation- and distribution-preserving bootstrapping method. Box plots indicate the 75th and 25th percentile of the fraction of overlapping winter and summer droughts across the segments in the model runs with the median as the bold line and the whiskers showing the full data excluding outliers.

A distinction can be made between these interannual dual-season droughts and the persistent droughts or megadroughts in Chapters 3 and 5. Given the multidecadal variability in the phasing of precipitation it is unclear if the models or the reconstruction will exhibit dual-season megadroughts in the NAM2 region. To test this, the drought identification metric was applied to the model and reconstructed SPI timeseries. Figure 6.19 plots the percentage of times that the ten highest-ranking winter and summer droughts overlap in time (defined by any number of overlapping drought years); results are shown for the full reconstruction and for a sliding 467-year (length of reconstruction) window across the full 1156-year model record (this produces a range in the temporal coincidence of the ten highest-ranking winter and summer droughts for each model, which are represented as boxplots in

Figure 6.19). To test the significance of these associations, 5000 pairs of independent surrogate timeseries with the same distribution and autocorrelation structure as the respective winter or summer SPI were produced for each dataset (using methods in outlined Chapter 2). For the reconstruction, the temporal coincidence between the ten highest-ranking winter and summer droughts for each surrogate pair was calculated, with the 99% level of these values being considered significant. For the CCSM and MPI models, 5000 pairs of surrogate timeseries were produced for each 467-year window. For each of these windows, temporal coincidence between the ten highest-ranking summer droughts and the ten highest-ranking winter droughts for each surrogate pair was again calculated, and the 99% level was recorded to produce a significance range (the grey shaded regions in Figure 6.19).

For the reconstruction, 80% percent of the ten highest-ranking winter and summer droughts are coincident in time, a value that is equal to the 99% level of the surrogate indices. This is a remarkable result and suggests that over the last five hundred years persistent drought in the NAM2 region has consistently been dual-season in character. It must be noted, however, that while the reconstruction methodology separates the winter and summer signals on interannual timescales (Griffin et al., 2013, e.g.), the low-frequency winter and summer signals are more challenging to parse given the short instrumental record. It is thus difficult to determine unequivocally that persistent dual-season drought does not result from low-frequency memory within the proxy itself (Bunde et al., 2013, e.g.). Nevertheless it is worth hypothesizing how persistent dual season drought occurs given the dynamics outlined in Section 6.2.2. Dual-season drought will require reduced precipitation in both winter and summer. This will involve less precipitation delivery from the winter Pacific storm track along with a weaker or less northward extended NAM — a combination that the average observation-to-reconstruction teleconnection characteristics suggests is relatively unlikely. Nonstationarity in the teleconnection dynamics is a potential source of this discrepancy and along these lines, persistent dual-season drought may occur in periods when the teleconnection or tropical Pacific variability changes such that in-phase precipitation

anomalies are more likely to occur. A second possibility is that winter drying is driven by a persistently cold tropical Pacific Ocean while summer drying is dominated by a persistently warm tropical Atlantic Ocean — as suggested in Figure 6.12 (see also Kushnir et al., 2010). The negative correlation in summer between the reconstruction and the tropical Atlantic Ocean, however, appears weaker than the summer connection to the tropical Pacific Ocean (Figure 6.12), although some nonstationarity of this relationship is suggested in Figure 6.13. Additionally, there may be land-surface or other feedbacks that become important during severe events or on long timescales. One potential example is the vegetation or dust aerosol feedback, both of which have been shown to be important in determining the spatial scale and magnitude of drought in the GP region (e.g. Cook et al., 2013).

For the models, only the CCSM simulation has 467-year periods with a significant association between the 10 highest-ranking winter and summer droughts, although the majority of the 467-year periods fall well below the significance range (97% of the periods are not individually significant at the 99% level). This indicates that the models, for the most part, do not simulate the persistent dual-season drought exhibited by the reconstruction (Bunde et al., 2013, note a similar discrepancy between paeloclimate reconstructions and model simulations). Nevertheless, the greater frequency (relative to MPI) of persistent dual-season drought in the CCSM model is a likely function of the model's specific dynamical characteristics. While both the MPI and CCSM models have been shown to exhibit large magnitude mean-state changes in the tropical Pacific, the CCSM model more consistently relates these changes to winter hydroclimate in the ASW (Chapter 5). Furthermore, the weak but positive summer teleconnection in the CCSM model, as compared to the moderately negative summer teleconnection in MPI, increases the likelihood that winter and summer SPI anomalies will be of the same sign. It is difficult to assess this model behavior in the context of the shorter reconstruction interval, which may be anomalous in its connection between persistent winter and summer drought (e.g similar to a significant period in the CCSM model). The MPI model, however, appears to underestimate the risk of persistent

dual-season drought, a characteristic that may or may not be shared by the CCSM model (Figure 6.19).

6.2.6 Conclusions

Multidecadal variability in the phasing of winter-to-summer precipitation anomalies in the ASW is a robust characteristic of models and a tree-ring based reconstruction of NAM variability (Griffin et al., 2013). While the latter part of the instrumental interval is marked by relatively frequent out-of-phase winter-to-summer precipitation anomalies, models do not reproduce periods with winter-to-summer precipitation anomalies that are predominantly out of phase, and the reconstruction indicates that such behavior is anomalous over a 500-year interval. While it is possible that this results from biases inherent to the models or the reconstruction methodology, it is likely necessary to expand the paradigm through which we view seasonal precipitation phasing in the ASW. One potential dynamical explanation for the simulated seasonal precipitation phasing behavior is nonstationarity of the ENSO teleconnection as demonstrated in Chapter 4 and Part 3 of Section 6.2.4. In the MPI model, for instance, there is no systematic seasonal precipitation phasing relationship, despite ENSO dynamics and an average teleconnection to the tropical Pacific Ocean that should produce out-of-phase seasonal precipitation anomalies. The highly nonstationary ENSO teleconnection to NA in both the winter and summer seasons (Part 3 of Section 6.2.4) may be the source of this discrepancy.

With regard to the seasonality of megadroughts, the reconstruction, CCSM and MPI models all exhibit multiple periods of predominantly in-phase winter-to-summer precipitation anomalies. Periods with an in-phase seasonal precipitation relationship create the possibility that dual-season drought will occur with a high probability. While this is true of interannual dual-season drought in both the models and the reconstruction, only the reconstruction and CCSM model (inconsistently) exhibit significant periods of persistent dual-season drought. While this result is derived from a short reconstruction and for a subset of the full ASW

region, it may clarify our understanding of the five highest-ranking droughts in the the NADA analyzed in Chapters 3 and 5 (all of which fall during the MCA and by consequence before the coverage of the Griffin et al., 2013, reconstruction). Principally, if the dual-season character of persistent drought over the NAM2 region for the period 1539–2005 C.E. can be used to infer the seasonality of MCA megadroughts, then during these features parts of the ASW with a dual-season precipitation signal had precipitation reductions in both seasons. This is surprising given the observed opposite-signed winter and summer teleconnections to the tropical Pacific for the NAM2 region (Section 6.2.2) and the hypothesized La Niña-like state during the MCA. Nevertheless, teleconnection nonstationarity and associated changes to the seasonal precipitation phasing relationship, like that described above for the MPI model, may explain this behavior. Another possibility is that MCA megadroughts are driven by multiple modes of atmosphere-ocean variability. This has been suggested elsewhere (e.g. Feng et al., 2008; Oglesby et al., 2012, indicate an important role for the Atlantic) and could explain both the dual-season and pancontinental (Section 6.1) character of megadroughts.

Chapter 7

Megadroughts in the Real World

7.1 Motivation and Questions

In Chapters 3 and 5 multiple modes of predominantly internal atmosphere-ocean variability were demonstrated to drive simulated megadroughts. The megadrought dynamics specific to each model were found to be a function of the decadal-to-multidecadal timescale dynamical characteristics of that model, with the strength and stationarity of teleconnections shown to play a particularly important role. Without better knowledge of the atmosphere-ocean state during past megadroughts, however, it is difficult to determine if any of these simulated megadrought dynamics are a reasonable representation of the real world. Toward such ends, Chapter 6 analyzes the seasonality of precipitation over the ASW and pancontinental drought over NA. Both the dual-season and pancontinental character of past persistent drought is suggestive of a role for multiple atmosphere-ocean dynamics in driving megadroughts and potentially of real-world teleconnection nonstationarity. One compelling possibility is that simultaneously warm conditions in the Atlantic and cool conditions in the Pacific underlie past megadroughts, particularly those during the MCA. Such an atmosphere-ocean state has been suggested previously for the MCA by Seager et al. (2007). Nevertheless, the specific characteristics of the MCA, principally the length of this atmosphere-ocean state (e.g., the

MCA-length tropical Pacific cold state of Mann et al., 2009) and whether it arose from an ocean dynamical response to increased forcing (e.g. Crowley, 2000) remains to be determined.

In this Chapter we use a newly available collection of tree-ring based hydroclimate reconstructions across the NH extratropics to answer two fundamental questions: 1) What is the most likely state of the dominant modes of NH atmosphere-ocean variability during megadroughts in the ASW? and 2) What is the likelihood that the MCA, the period with the greatest incidence of these features, was persistently La Niña-like? Specifically, we employ the NADA, MADA and the new OWDA, which in aggregate provide annual estimates of hydroclimate variability for an unprecedented 58% of NH land grid points back to 1250 C.E and 22% of NH land grid points back to 1000 C.E. with at least 2.5° resolution. Importantly, this work is the first to leverage this unprecedented collection of hydroclimate reconstructions in an aggregate analysis

7.2 Methods

The collective set of drought atlases (NADA, MADA and OWDA — hereinafter the NH tree-ring record) are used to reproduce the positive or negative state of the four dominant modes of atmosphere-ocean variability that impact hydroclimate in the ASW: the ENSO (Niño3.4 index), AMO, PDO and North Atlantic Oscillation (NAO). Targeting simply the positive or negative state of these modes of variability differs from paleoclimate reconstructions, which seek to provide more detailed information about past states of the atmosphere-ocean system. We employ a climate analogues framework in which the instrumental interval (1870-2005 C.E. — training interval) is used to define the spatial patterns of NH hydroclimate associated with the targeted modes of variability (hereinafter impact maps). These impact maps are then compared to the pattern of hydroclimate across the collection of drought atlases to determine the most likely atmosphere-ocean state for each year of the pre-instrumental period. This analysis, however, was limited to the period after

1000 C.E. for which the NADA and OWDA provide coverage over a large percentage of their spatial domains. The full details of the method are outlined in the Section 7.2.2 and it is also validated using pseudoproxy experiments (e.g. Smerdon, 2012) in Section 7.2.3.

7.2.1 Modes of Variability

The ENSO (Niño3.4 index), PDO and AMO indices were calculated as outlined in Chapter 2 and specifically Section 2.6.1. The NAO was calculated from the 20th century reanalysis (Compo et al., 2011) as the sea-level pressure difference between the Subtropical (Azores) High (37.82°N, 25.75°W) and the Subpolar Low (65.08°N, 22.73°W) for the November–March (NDJFM) period. All composites based on the climate indices are calculated using the JJA grid point PDSI and either the preceding DJF average ENSO or PDO indices, the preceding NDJFM average NAO index, or the contemporaneous JJA average AMO index.

7.2.2 Climate Analogues Framework

The climate analogues framework consists of four steps:

1: Sorting the Dynamics

For each of the four modes of variability the instrumental record (1870–2005 C.E.) is segmented into years that are in the top (positive), middle (neutral) and bottom (negative) third of the full distribution of values.

2: Defining Impact Maps

Hydroclimate composites are produced from the collection of drought atlases where each grid point is assigned 1 for wet and 0 for dry. These composites are estimates of the impact of positive, negative and neutral states of the modes of variability on the tendency

towards wetting or drying (hereinafter impact maps). The composites are first calculated for all years that fall in the positive, neutral or negative state of each mode (12 in total — 3 for each of the 4 modes of variability). The positive ENSO impact map, for instance, is a composite of the NH tree-ring record over all years in the instrumental record with a positive ENSO state (top third). The impact maps are also calculated for all combinations of two-to-four modes. For instance, impact maps will be calculated for all years with a positive ENSO state and each of the 9 states of the other three modes (e.g. positive ENSO and positive AMO; two-mode combinations), as well as all combinations of three- and four-modes using the same logic. Only impact maps with at least four events over the training interval are employed, the motivation for which is provided in the following section, giving a total of 154 impact maps (of 255 possible). The impact maps corresponding to the positive and negative state of each mode in isolation are plotted in Figure 7.1.

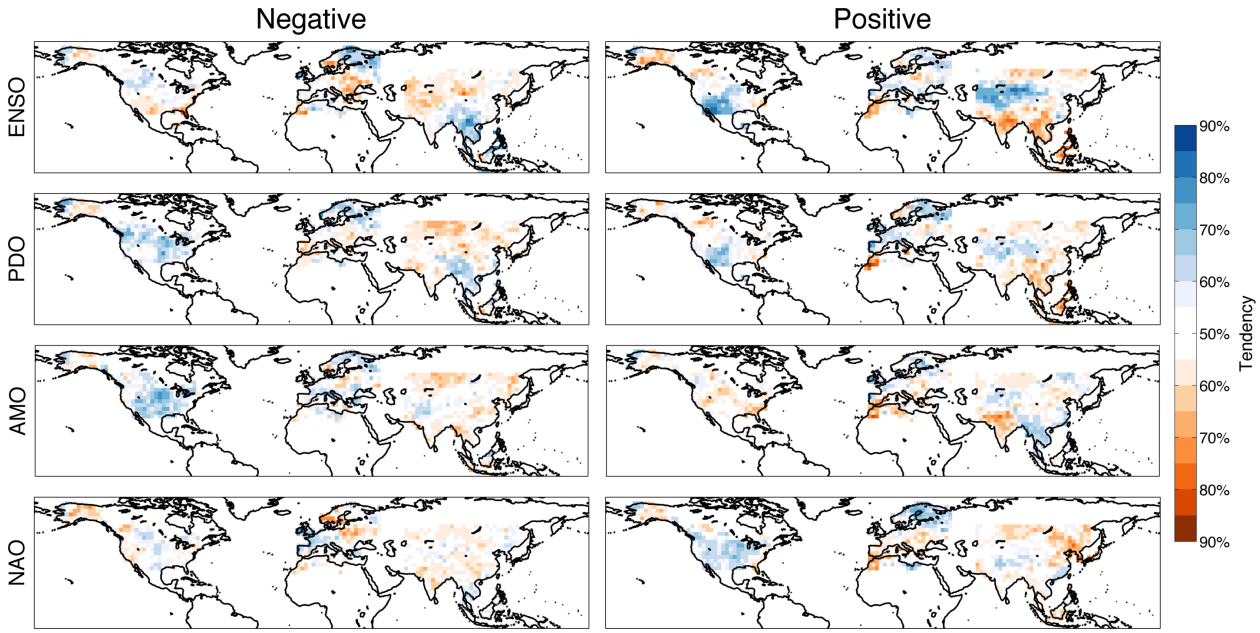

Figure 7.1: Impact maps corresponding to the positive and negative state (one mode combinations) of each mode of variability. Tendency is defined as the percentage of years in the composite that were wet or dry at each grid point. As an example, a tendency of 90% dry for positive ENSO would indicate that 90% of years in the top third of ENSO values were dry at that grid point.

3: Dynamical Timeseries

For each year back to 1000 C.E. the pattern of hydroclimate is compared to each of the 154 impact maps using a CPCS. The CPCS, however, is not a good measure of pattern similarity when the input patterns lack spatial heterogeneity. This is problematic because impact maps defined over few events have little spatial heterogeneity. This issue is circumvented by requiring that the impact maps have at least four events over the training interval (previous section), with impact maps corresponding to fewer than four events not included in the climate analogues framework. For the period after 1250 C.E., the impact map that best matches the spatial pattern of reconstructed hydroclimate across all three drought atlases in a given year (highest CPCS) defines the atmosphere-ocean state for that year. For 1000 C.E.-1249 C.E., however, the spatial pattern of reconstructed hydroclimate is compared to the impact maps over just the NADA and OWDA regions (as the MADA begins in 1250 C.E.).

Not all of the 154 impact maps provide a value for the state of all four modes. The impact map that corresponds to just a positive ENSO state, for instance, doesn't provide a value for the state of the PDO, AMO and NAO. By consequence, for years in which the chosen impact map (highest CPCS) corresponds to a one, two or three-mode combination, secondary impact maps also need to be chosen. These secondary impact maps provide values for the modes that were not a part of the original (highest CPCS) combination, while remaining dynamically consistent with that combination. Specifically, in each year where a one, two or three mode combination is chosen, the impact map with the next highest CPCS and a value for at least one of the missing modes is chosen as the secondary impact map. This process continues until a value for all four modes is determined in a given year. In each case the secondary impact maps have to be dynamically consistent with the first impact map, and each other (for instance if the primary impact map were for a positive ENSO state the secondary impact maps cannot have a neutral or negative ENSO state). For the climate analogues framework completed herein the 5th, 50th and 95th percentile of the

highest CPCS (corresponding to the impact map that defines the atmosphere-ocean state in each year) are 0.20, 0.30 and 0.49, respectively.

4: Timeseries Filtering

The dynamical timeseries are ten-year low pass-filtered using a ten-point Butterworth filter to elucidate the decadal-to-multidecadal variability of the four modes of variability.

7.2.3 Methodological Validations

Pseudoproxy Experiments

Four 500-year control simulations are used in a pseudoproxy context to test the climate analogues framework (CCSM, GISS, IPSL and MPI). The use of multiple models is important given research that suggests skill in pseudoproxy experiments is model dependent (e.g. Smerdon et al., 2015a) and the four models were chosen to sample a range in the characteristics of decadal-to-multidecadal atmosphere-ocean dynamics (Chapters 5 and 6).

The climate analogues framework is computed using the same grid points as the NADA, MADA and OWDA but with noise added to the PDSI fields from each model to produce a signal-to-noise ratio of 0.5, which approximates the level of noise within the NADA (Cook et al., 2004). To best mimic the characteristics of the actual climate analogues framework, the impact maps are calculated eight times, each corresponding to a different 135-year (length of the instrumental interval) training interval.

Pseudoproxy Timeseries

Figures 7.2 and 7.3 provide a visual representation of the dynamical timeseries produced by the climate analogues framework within the pseudoproxy experiments. In both figures the model ground truth is plotted for comparison. Skill is measured herein as the fraction of years outside of the training interval in which the dynamical timeseries from the

climate analogues framework is the correct sign relative to the model ground truth. Using this metric for each model and mode, Figure 7.2 plots the dynamical timeseries corresponding to the best (highest skill) and worst instrumental-length (135-year) training interval. For comparison, Figure 7.3 plots the dynamical timeseries corresponding to impact maps calculated over the full temporal extent of the model simulations.

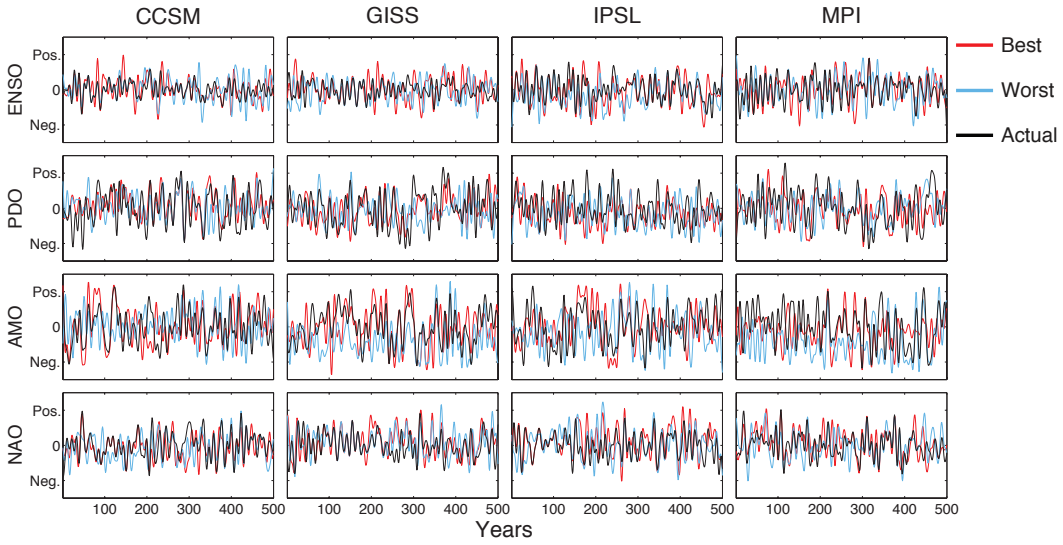

Figure 7.2: Example dynamical timeseries for each model and mode. The actual time history of the mode is plotted (black) with the time history corresponding to the training interval that produced the worst (blue) and best (red) dynamical timeseries.

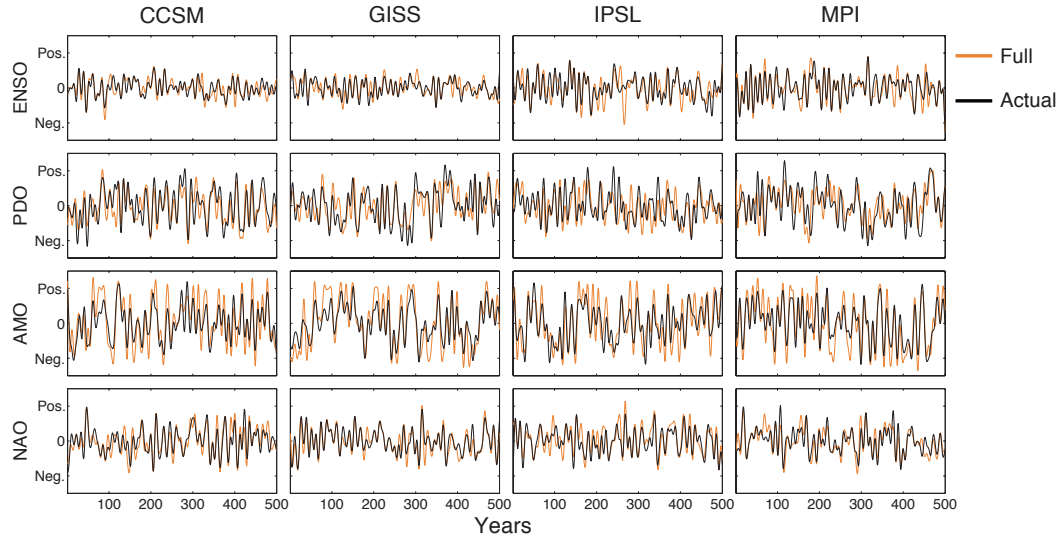

Figure 7.3: Example dynamical timeseries for each model and mode. The actual time history of the mode is plotted (black) with the dynamical timeseries corresponding to the impact maps calculated over the full temporal extent of the model simulations plotted (orange).

The visual representations in Figure 7.2 indicate that for all models and modes the best timeseries (red lines in Figure 7.2) reproduce much of the time history of the model ground truth. Even for the worst ENSO and NAO timeseries (blue lines in Figure 7.2), the dominant features of the time history of the ground truth is still reproduced. This provides confidence that the climate analogues framework will provide useful information for defining the state of the ENSO and NAO during megadroughts. The worst timeseries of the PDO and AMO, however, struggle to reproduce the time history of these modes, but this result is somewhat model and period dependent.

The dynamical timeseries associated with impact maps calculated over the full temporal extent of the model simulations are nearly perfect representations of the model ground truth (Figure 7.3). Therefore, any inability to reproduce these modes of variability appears to be related to the short 135-year training intervals providing too few degrees of freedom to properly constrain their impact on hydroclimate over the NH. This is particularly true of the PDO and AMO because of the longer timescales of variability inherent to these modes. Importantly, this will be a fundamental limitation of any method that calibrates on the instrumental interval, including any indirect (i.e. not based on local proxies that directly sample the variable of interest, in this case SSTs) reconstructions of these modes and particularly those using land-based proxies. Nevertheless, model representation of the PDO and AMO, and their hydroclimate impacts, is poor (Chapters 2 and Section 6.1). In particular, the teleconnections between these modes and NH land areas appear weaker than those observed over the instrumental interval. This presents a serious caveat for the pseudoproxy experiments performed herein and given this, the pseudoproxy-derived skill for these modes may be a pessimistic (or potentially conservative) representation of potential real-world skill.

Skill Scores

To explicitly define the skill of the climate analogues framework, Figure 7.4 plots the fraction of years during the non-training interval in which the dynamical timeseries is

the correct sign relative to the real ENSO, PDO, AMO and NAO from the model output. The boxplots demonstrate the range in skill for the eight instrumental-length training intervals and the asterisks indicate the skill value if the impact maps are calculated over the full temporal extent of the model simulations. We calculate a significant skill threshold by randomly generating the positive, negative or neutral state of each mode in each year 1,000 times and assessing the 95th percentile of skill for these randomly generated timeseries (skill below the threshold are plotted as the grey shaded regions in Figure 7.4). Additionally, to test the benefit provided by using the collection of drought atlases, the pseudoproxy skill is calculated for a climate analogues framework using just the individual regions covered by the NADA, MADA and OWDA (and combinations — boxplot colors in Figure 7.4).

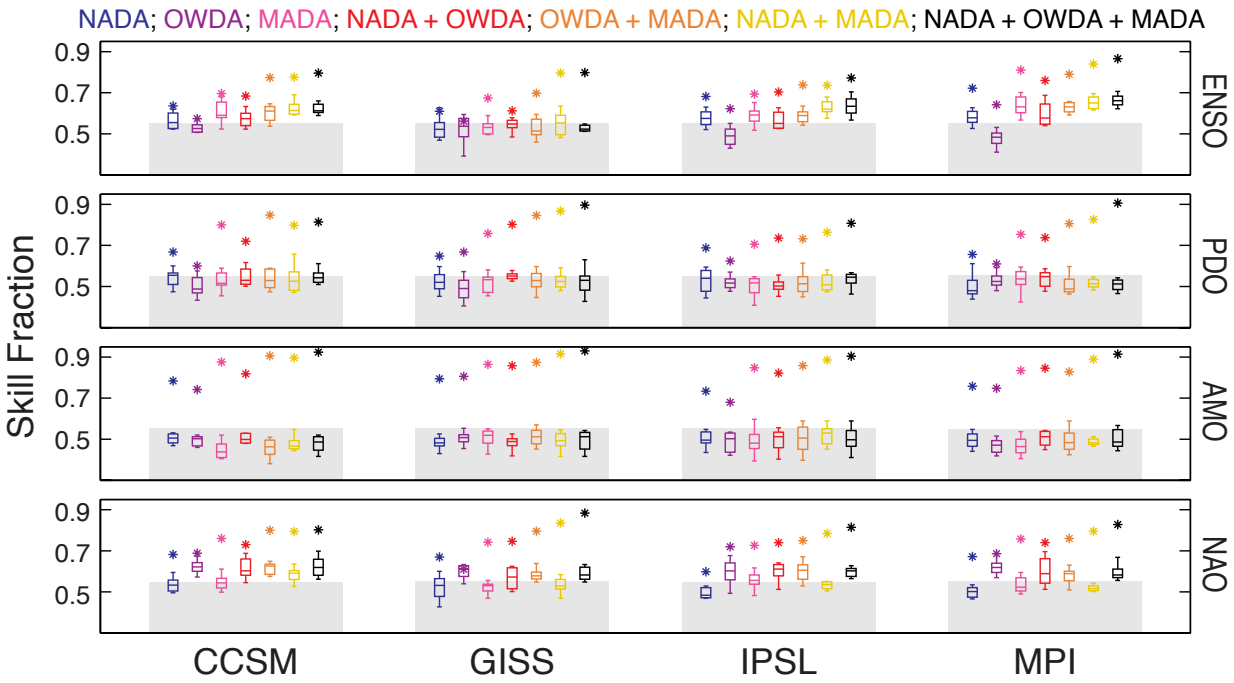

Figure 7.4: Skill calculated as the percentage of years in which the dynamical timeseries calculated using the climate analogues framework is the correct sign relative to the model ground truth. The asterisk is the skill when using the full temporal extent of the model simulation to compute the impact maps. The boxplots are the range in skill for impact maps calculated using 135-year (length of the instrumental interval) training intervals. Each color corresponds to a climate analogues framework computed using a subset of the full NH spatial range. Skill below the 95th percentile for randomly generated dynamical timeseries is denoted by the gray shaded region. All pseudoproxies have been calculated using a 0.5 signal-to-noise ratio.

As was suggested by the visual representations in Figure 7.2 and 7.3, given enough degrees of freedom, the climate analogues framework will be highly skillful (asterisks in Figure 7.4). For instrumental length training intervals, however, the climate analogues framework is only significantly skillful for the ENSO and NAO and this behavior is not highly model dependent. Finally, using the NADA, MADA and OWDA regions together provides additional skill relative to a climate analogues framework calculated using only individual regions.

7.3 Results

The right hand panels of Figure 7.5 plot five published ENSO reconstructions, which are not fully independent but are calculated using different reconstruction methods and proxy networks. These provide a point of comparison to our own analyses and a survey of whether currently available ENSO reconstructions support the hypothesis that La Niña-like states underlie megadroughts (e.g. Herweijer et al., 2007). As might be expected given the research outlined in Chapter 1, there is only weak agreement between the overall time history of the five reconstructions and large differences in the magnitudes and variability structures (only three of the ten possible correlations between reconstructions are significant at the 99% level). To focus specifically on the dynamics underlying megadroughts, the left hand panel of Figure 7.5 indicates the percentage of megadrought years that have positive or negative values in each of the ENSO reconstructions. To maintain consistency with Chapters 3 and 5, focus is limited to the five highest-ranking droughts over the ASW in the NADA using the drought identification metric. In aggregate, the reconstructions suggest that ENSO tends to be negative during megadroughts. Nevertheless, of the 16 times that the five highest-ranking droughts overlap with the timing of the ENSO reconstructions only five are individually significant at the 95% level using a distribution and autocorrelation preserving bootstrapping significance test (Chapters 2 and 5). Given the heterogeneity in these reconstructions and the general ambiguity of the suggested relationships between

reconstructed ENSO and megadroughts, additional research is clearly needed to constrain megadrought dynamics. Along these lines, we use the new set of drought atlases to determine the dynamics that underlie megadroughts, allowing for the possibility that multiple modes of atmosphere-ocean variability are needed to produce these features.

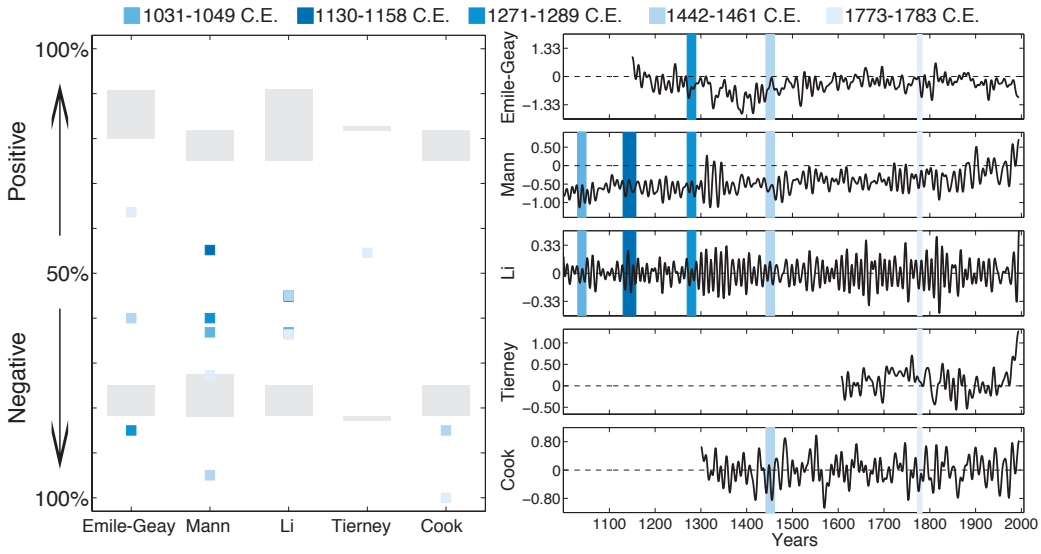

Figure 7.5: (right) Reconstructions of ENSO using different methods and proxy networks (Emile-Geay et al., 2013; Mann et al., 2009; Li et al., 2013; Tierney et al., 2015; Cook et al., 2009). In each case the data has been ten-year low-pass filtered. For Emile-Geay et al. (2013), Li et al. (2013), and Cook et al. (2009) the reconstructed index is for the Niño3.4 region, while for Mann et al. (2009) it is the Niño3 region and for Tierney et al. (2015) it is the eastern Pacific (10°N–10°S, 175°E–85°W). The timing of the five highest-ranking droughts is denoted by the colored regions. (left) Associations between the identified megadroughts and ENSO for the period 1000-2005 C.E. using linearly detrended timeseries as some reconstructions are standardized against a warm instrumental interval (e.g. Mann et al., 2009, and by consequence are always anomalously negative outside of that interval). For associations at 100% "Positive", every year of the identified drought has a reconsrtucted ENSO value that is positive (and vice-versa for 100% "Negative").The colored squares are for the five individual highest-ranking droughts (less than five of these features, however, overlap with the reconstructed record in Emile-Geay et al., 2013; Tierney et al., 2015; Cook et al., 2009). The shaded regions are the range in 95% significance level for the five identified droughts using a distribution and autocorellation preserving bootstrapping method to test statistical significance (Chapters 2 and 5).

Figure 7.6 shows the output of the climate analogues framework outlined in Section 7.2.2 and validated in Section 7.2.3. For each of the five highest-ranking droughts over the ASW (bottom panel of Figure 7.6), we assess the underlying dynamics by calculating the

percentage of drought years that have implied positive or negative values in each of the ENSO, PDO, AMO and NAO indices (Panel A of Figure 7.7). Megadroughts over the ASW are consistently and significantly tied to an implied negative (or cold) ENSO state, with 97% of megadrought years having negative ENSO values. The association between ENSO and megadroughts is found to be present regardless of the underlying regions employed in the climate analogues framework (with the exception of just the OWDA — Panel B of Figure 7.7), providing confidence that the association is robust and not solely dependent on the NADA, in which the megadroughts were identified. Instead, a hemispheric hydroclimate pattern is present during megadroughts that is characteristic of a negative ENSO state. This pattern involves a north (wet)-south (dry) dipole of hydroclimate over western NA with an opposite signed north-south dipole over Asia and dry conditions over the Iberian peninsula and central Europe. Importantly, we hypothesize that such a pattern is unlikely to have resulted from stochastic internal atmospheric variability, which tends to have more regional, as opposed to hemispheric, impacts.

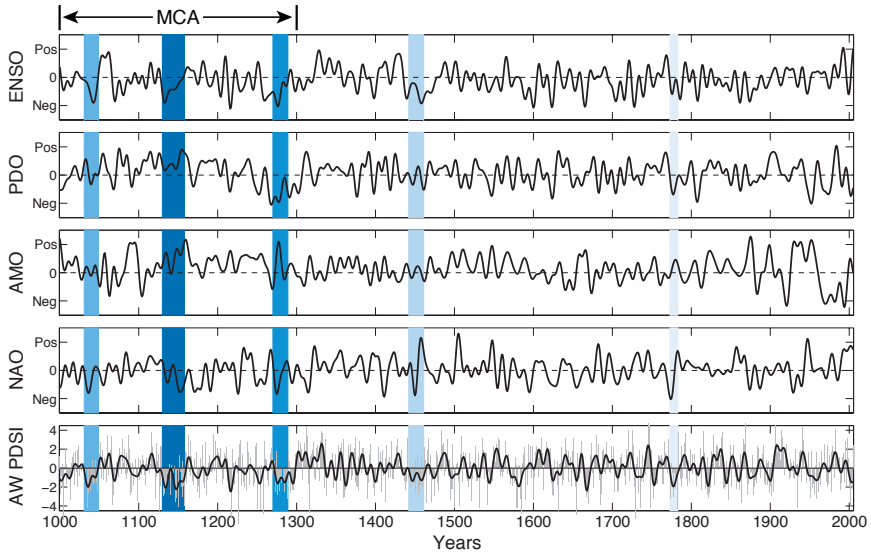

Figure 7.6: Timeseries of ENSO, PDO, AMO and NAO states with the five highest-ranking droughts denoted by the colored regions. The timeseries show the 10-year low-pass filtered (with a ten-point Butterworth filter) the results from the climate analogues framework. If the timeseries is at "positive" on the vertical axis then all of the individual years contributing to the 10-year low pass filtered value would be positive. The MCA (1000–1300 C.E.) is marked at the top of the figure. The bottom panel shows the ASW PDSI timeseries.

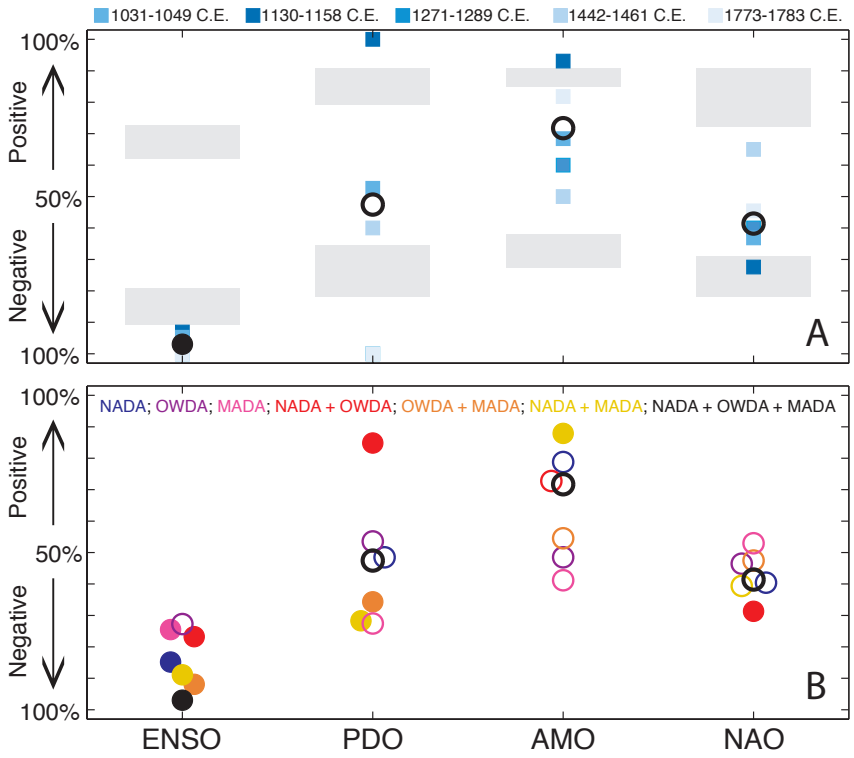

Figure 7.7: Panel A shows the association between the five highest-ranking droughts and the atmosphere-ocean dynamics. For associations at 100% "Positive", every year of the identified drought has a dynamical timeseries value that is positive (and vice-versa for 100% "Negative"). The colored squares are the results for the five individual highest-ranking droughts. The shaded regions in Panel A are the range in 95% significance level for these five highest-ranking droughts using a distribution and autocorellation preserving bootstrapping method to test statistical significance (Chapters 2 and 5). The circles show values for all five identified droughts considered collectively, with the filled circles being those associations that are significant at the 95% level. Panel B shows the same values but calculated using subsets of the full NH dendroclimatic reconstructions.

The three highest-ranking droughts in the ASW over the last millennium occurred during the MCA (bottom panel of Figure 7.6), defined herein as 1000-1300 C.E. While the limitations of the NH tree-ring record constrain our analyses to the period after 1000 C.E., all five of the highest-ranking droughts would fall within the more traditional MCA definition of 850-1300 C.E. (e.g. Chapter 5). MCA megadrought severity and clustering, along with strong coupling of ASW hydroclimate to tropical Pacific SSTs and a hypothesized La Niña-like response of the tropical Pacific to positive external forcing, has led to speculation that the tropical Pacific was persistently La Niña-like over the extent of the MCA. The ENSO timeseries in Figure 7.6, however, does not appear to be persistently La Niña-

like during any MCA-length (300-year) period. The NH tree-ring record, therefore, does not support the hypothesis that the MCA was La Niña-like throughout, nor does it suggest that a forced response in the tropical Pacific is dominant on centennial and longer timescales.

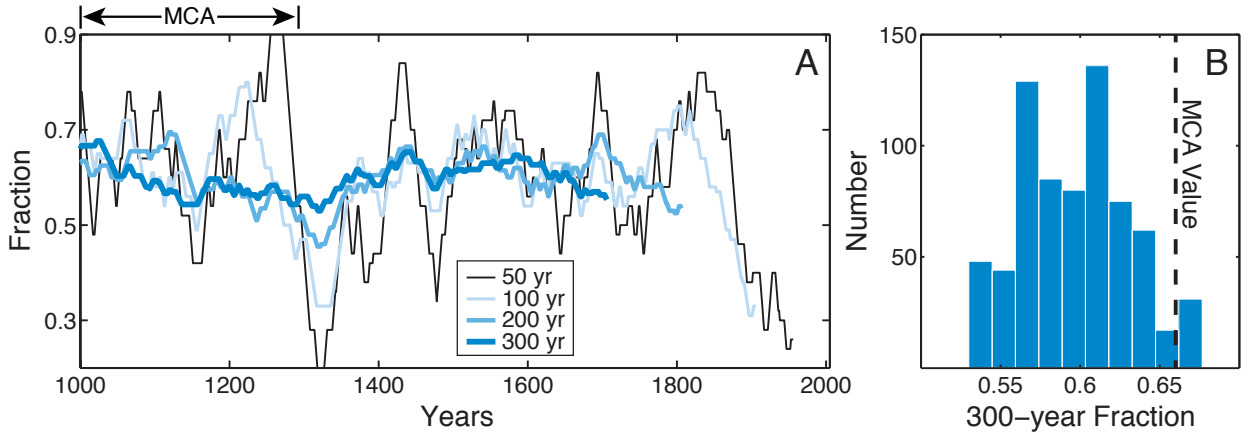

Figure 7.8: Panel A is the fraction of years with a negative ENSO value for sliding windows of 50, 100, 200 and 300-years length. The horizontal axis shows the first year of each window. Panel B is a histogram of the fraction of years in each 300-year segment (length of the MCA) with a negative ENSO value. The value corresponding to the MCA (1000-1300 C.E.) is plotted as the vertical line.

Shorter ten-to-thirty year cold states in the tropical Pacific, however, are a relatively consistent feature of the last millennium of ENSO variability (Figure 7.6). It is these features that predominantly underlie megadroughts (Panel A of Figure 7.7). While the MCA has a high incidence of ten-to-thirty year cold states in the tropical Pacific, the temporal clustering is not singular when compared to other 300-year periods. The 300-year period beginning in the late 16th century, for instance, also has a high incidence of ten-to-thirty year cold states in the tropical Pacific (Figure 7.6 and Panel A of Figure 7.8). Likewise, the percentage of negative ENSO years during the MCA is not singular when compared to other 300-year periods (95th percentile in fraction of negative ENSO years — Panel B of Figure 7.8). Finally, the three tropical Pacific cold states that underlie the MCA megadroughts are not the most exceptional of the last millennium when ranked by the number of consecutive negative ENSO years (they are the 4th, 5th and 14th ranked — not shown). Because tropical Pacific cold states during the MCA are neither more prevalent nor exceptional in character,

it may be necessary to invoke other atmosphere-ocean dynamics to explain the severity and clustering of megadroughts during the MCA.

While there are no significant connections between the other three modes of atmosphere-ocean variability and the five-highest ranking droughts in the ASW (when considered together — Panel A of Figure 7.7), these may have played a secondary role in determining the severity and clustering of megadroughts during the MCA. Forcing from warm tropical North Atlantic SSTs, for instance, is an atmosphere-ocean state that produces drying over the ASW (e.g. Feng et al., 2008; Oglesby et al., 2012; Schubert et al., 2009; Kushnir et al., 2010; McCabe et al., 2004). The timeseries in Figure 7.6 suggests that there were warm conditions in the Atlantic during the MCA, as the AMO is persistently positive in Figure 7.6 from approximately 1100-1300 C.E. The shift to a positive AMO is coincident with a period of protracted drying in the CP region of NA (e.g. Cook et al., 2010b, 2013), where hydroclimate variability is reasonably tightly coupled to Atlantic SSTs (e.g. Kushnir et al., 2010; McCabe et al., 2004). Importantly, the MCA is the highest-ranked 300-year period when ranked by fraction of years with both a negative ENSO state and positive state of the AMO (not shown). A potential mechanism would involve tropical North Atlantic SSTs driving background drying during the MCA upon which ten-to-thirty year cold states in the tropical Pacific produced particularly severe megadroughts. Nevertheless, the AMO was not positive during the early part of the MCA (Figure 7.6) and pseudoproxy experiments (Section 7.2.3) provide less confidence in the ability of the climate analogues framework to reproduce the state of the AMO because of poor sampling of such low-frequency modes over the 135-year training interval.

Figure 7.6 additionally suggests that the PDO was positive during much of the MCA. A positive PDO does not produce drying over the ASW (e.g. McCabe et al., 2004). It is worth noting, however, that a positive PDO during the MCA is inconsistent with the results of MacDonald & Case (2005), in which western NA tree-ring chronologies were used to reconstruct a negative PDO for the first half of the last millennium. The full NH tree-ring record

used herein, therefore, contradicts the MCA PDO signal within the western NA tree-ring chronologies employed by MacDonald & Case (2005). While the pseudoproxy experiments used for methodological validation provide less confidence in this result (Section 7.2.3), a recent reconstruction of bi-hemispheric interdecadal Pacific variability also suggests that the PDO was positive during the MCA (Vance et al., 2015). With regard to MCA megadroughts, these might have been even more severe if not for the the implied positive conditions in the PDO during this period.

7.3.1 Conclusions

The new hemispheric record of hydroclimate variability provided by the NADA, MADA and OWDA has been used herein to provide a best estimate of the state of the four dominant modes of NH atmosphere-ocean variability during megadroughts. Over the last millennium, megadroughts are consistently and significantly associated with decadal-to-multidecadal cold states in the tropical Pacific. Nevertheless, a prominent hypothesis that the MCA, the period with the greatest incidence of these features, was persistently La Niña-like is incongruous with the results of our analysis. Instead, warm conditions in the Atlantic may have played a necessary role in driving drying during the MCA. Importantly, these dynamics are in accordance with both the dual-season character of persistent drought and the increase in the frequency of pancontinental drought during the MCA (and specifically during MCA megadroughts — Chapter 6). To produce dual-season megadroughts with this atmosphere-ocean state would involve a cold tropical Pacific driving winter drying while warm Atlantic conditions produce summer drying. Cold tropical Pacific and warm Atlantic conditions are also associated with an increase in the frequency of pancontinental drought occurrence during the instrumental interval (Figure 6.7 of Chapter 6).

With regard to the forced versus internal origins of tropical Pacific cold states, the MCA was not La Niña-like over its full extent, nor were the individual cold states more persistent during this period, which is inconsistent with a strong thermostat response (Clement

et al., 1996) to increased forcing (e.g. Crowley, 2000) and potentially suggestive of an important role for internal variability. Such a scenario in the tropical Pacific is consistent with that of CCSM in Chapter 5, which exhibits similar ten-to-thirty year cold states in the tropical Pacific that result from internal variability.

Chapter 8

Conclusions

8.1 Summary, Discussions and Future Work

Both ECHO-G and an ensemble of models from the CMIP5/PMIP3 are capable of simulating megadroughts in the ASW that are similar in duration and magnitude to those observed in the paleoclimate record. The droughts are not, however, temporally synchronous with those in the proxy record. Furthermore, there is very little overlap between drought features in the PMIP3 runs, despite the use of similar forcing series to drive these simulations. Similarly, in the ECHO-G model, megadroughts do not appear to have a preferred forcing state. Together this suggests that model-simulated megadroughts can result from internal variability of the modeled climate system, rather than as a response to changes in exogenous forcings, or from compensating feedback mechanisms that mask a forced hydroclimate response. In support of the former possibility, the statistics of persistent drought in unforced control runs are largely consistent with those in the corresponding forced simulations.

While stochastic atmospheric variability is able to drive persistent drought in CGCMs (e.g., ECHO-G — Chapter 3), it is not a robust feature. In particular, models with strong and stationary teleconnections (e.g., CCSM — Chapters 4 and 5), and large multi-decadal variability in the tropical Pacific (Chapters 2, 5 and 6), simulate megadroughts driven by

internal variability of the tropical Pacific mean state. Analysis of the NH tree-ring record over the last millennium suggests that models like CCSM are perhaps best representing real-world megadrought dynamics. Principally, real-world megadroughts are consistently driven by ten-to-thirty year cold states in the tropical Pacific Ocean (Chapter 7). It is important to note, however, that CCSM may be getting the right answer — megadroughts driven by the tropical Pacific boundary conditions — for the wrong reasons. Along these lines, the analyses in Chapter 7 suggest a necessary role for Atlantic SSTs in driving megadroughts, particularly the clustering and severity of these features during the MCA. Further evidence for a relationship between Atlantic SSTs and megadroughts is provided by both the dual-season character of persistent drought and the increase in the frequency of pancontinental drought during the MCA (and specifically during MCA megadroughts — Chapter 6). CCSM, however, does not exhibit a relationship between the AMO or equatorial Atlantic and megadroughts (Figure 5.6 of Chapter 5) and more generally the characteristics of non-ENSO modes of atmosphere-ocean variability are much less realistic in state-of-the-art CGCMs. In the case of CCSM, for instance, the association between megadroughts and the tropical Pacific may not result from the efficacy of the model's dynamics but rather because ENSO unrealistically dominates overall climate variability (e.g. the unrealistically large tropical Pacific variability in Figure 2.9).

With regard to future projections, this discussion speaks to the importance of analyzing specific models and ensemble behavior from a dynamical perspective. Specifically, the work presented herein complements approaches that employ a statistical rescaling of model output using information about real-world hydroclimate persistence from the observed and paleoclimate record to assess the risk of future hydroclimate change (e.g. Ault et al., 2013, 2014). A model can both succeed and fail at reproducing observed persistence characteristics for a variety of dynamical reasons; understanding what drives the simulated hydroclimate dynamics on these timescales will help provide reliable information on the risk of future drought in the ASW. Along these lines, whether or not it is dynamically realistic, low-

frequency hydroclimate variability driven by the atmosphere and SST variability outside the tropical Pacific Ocean are common model features. Given that these same models are used to produce future projections, it is critical to better understand this model behavior in the context of the actual climate system. A stark example would be the model response to a greenhouse gas induced change to either the ENSO (e.g. Clement et al., 1996) or AMO (e.g. Ting et al., 2009). If these responses are large in magnitude, the simulated hydroclimate change over NA will be different for each model. In CCSM, for instance, a large forced response in the tropical Pacific Ocean would be expected to drive large hydroclimate impacts over NA, including pancontinental megadroughts. The same change in BCC, however, would yield smaller impacts.

Despite the efforts herein, it is difficult to determine which of these model responses is realistic, and by consequence, which model projection should be considered the most accurate, because even in models that are successful at simulating the observed and paleoclimate atmosphere-ocean dynamics, the dynamical relationships are often nonstationary and their connections to radiative forcings are not well constrained. This issue is compounded by the fact that the observed dynamics themselves have been inferred from a 152-year instrumental interval that cannot provide a full assessment of the stationarity of real-world dynamics. In lieu of a more complete understanding of past and future climate variability, it will be important to consider projections of hydroclimate beyond a "one model, one vote" approach, in which the CGCM ensemble average projection is taken as the best guess at the future state of the climate system. Such an approach has statistical merit (Weigel et al., 2010), particularly in situations, such as this, with incomplete information on the error and bias structures of CGCMs (Knutti et al., 2010). Given the conclusions presented herein, however, it is clear that ensemble averaging CGCM projections will mask differences in the model response to increasing greenhouse gases that have important (even if unrealistic) dynamical underpinnings.

The discussion of future hydroclimate projections up to this point has only invoked

forced variability. Any CGCM projected response to increased greenhouse gas forcing (e.g., Chapter 1 and Cook et al., 2015) will nevertheless couple with multidecadal internal variability in the atmosphere and the oceanic boundary conditions to determine the actual hydroclimate state in the near-term future. In Chapter 7 multidecadal hydroclimate variability and megadroughts appear to be lower-frequency analogs of the more familiar annual events, both driven by the tropical Pacific Ocean. If indeed true, this characteristic might provide some predictability based on long timescale characteristics of the state of the tropical Pacific Ocean, although operational prediction has yet to exceed the seasonal timescale (e.g. Barnston et al., 2012; Zhu et al., 2012). Likewise, in Chapters 6 and 7 the AMO is demonstrated to provide an important control on the character of multidecadal hydroclimate variability, particularly its severity, seasonality and spatial features. The slowly varying nature of this mode, and its connections to the wider atmosphere-ocean system, suggests that it is a potential target for predictability on decadal and longer timescales (e.g. Smith et al., 2012; McCarthy et al., 2015). Multidecadal projections that take into account the most likely future trajectory of the ENSO and potentially of the AMO therefore appear possible and stand as critical efforts for projecting the risk probabilities associated with drought over the near-term future.

While this study presents a critical baseline by which to inform future research on the climate of the C.E. and projections of hydroclimate over the ASW, more needs to be done to improve our understanding of hydroclimate dynamics on these timescales. Of principle importance will be understanding the origin of decadal variability in the tropical Pacific Ocean and whether it is a low-frequency expression of the internally generated ENSO, results from interplay of multiple modes of internal atmosphere-ocean variability or has a forced component. Along these lines, that the MCA was not La Niña-like throughout, nor were the cold states more persistent during this period, suggests a role for internal dynamics in generating decadal variability in the tropical Pacific Ocean (Chapter 7). This is of societal importance because it would indicate that megadroughts driven by the tropical Pacific boundary condi-

tions can occur today, regardless of any anthropogenic greenhouse gas forcing. Importantly, subsequent research on the origin of decadal variability in the tropical Pacific and other facets of decadal-to-multidecadal hydroclimate dynamics will benefit from the techniques developed in this dissertation. With the advent of further regional paleoclimate datasets of hydroclimate variability (e.g., the new OWDA — Cook, in review), for instance, these methods for characterizing past and simulated hydroclimate can be expanded to inform our understanding of global drought risk. Additionally, high resolution reconstructions of climate variables from such diverse sources as speleothems, leaf waxes, and corals represent another important source of information on low-frequency climate variability that can be analyzed in a paleoclimate model-data comparison framework. An intriguing possibility would be to combine this range of available proxy data to produce a comprehensive global multi-model drought attribution study based on direct estimates of both past hydroclimate and atmosophere-ocean states. This will further inform our understanding of the varying mechanisms of drought generation in the CMIP5 models. To do this with certainty will require, in particular, longer independent and direct (or in situ) records of proxy estimated ocean conditions (e.g. Tierney et al., 2015) in addition to continued efforts to improve the sampling, analysis and reconstruction methods of the paleoclimate record of the C.E. Combining such paleoclimate products with continued model work promises to both improve our understanding of past hydroclimate variability and the way in which we represent important climatic processes in climate models, the latter of which is essential for accurately constraining projected hydroclimate risks in the 21st century.

Bibliography

Anchukaitis, K. J., Breitenmoser, P., Briffa, K. R., Buchwal, A., Büntgen, U., Cook, E. R., D'Arrigo, R. D., Esper, J., Evans, M. N., Frank, D., et al. (2012). Tree rings and volcanic cooling. *Nature Geoscience*, *5*(12), 836–837.

Ault, T. R., Cole, J. E., Overpeck, J. T., Pederson, G. T., & Meko, D. M. (2014). Assessing the risk of persistent drought using climate model simulations and paleoclimate data. *Journal of Climate*, *27*(20), 7529–7549.

Ault, T. R., Cole, J. E., Overpeck, J. T., Pederson, G. T., St. George, S., Otto-Bliesner, B., Woodhouse, C. A., & Deser, C. (2013). The continuum of hydroclimate variability in western north america during the last millennium. *Journal of Climate*, *26*(16), 5863–5878.

Barnston, A. G., Li, S., Mason, S. J., DeWitt, D. G., Goddard, L., & Gong, X. (2010). Verification of the first 11 years of iri's seasonal climate forecasts. *Journal of Applied Meteorology and Climatology*, *49*(3), 493–520.

Barnston, A. G., Tippett, M. K., L'Heureux, M. L., Li, S., & DeWitt, D. G. (2012). Skill of real-time seasonal enso model predictions during 2002-11: Is our capability increasing? *Bulletin of the American Meteorological Society*, *93*(5), 631–651.

Becker, A., Finger, P., Meyer-Christoffer, A., Rudolf, B., Schamm, K., Schneider, U., & Ziese, M. (2013). A description of the global land-surface precipitation data products of the global precipitation climatology centre with sample applications including centennial (trend) analysis from 1901-present. *Earth System Science Data*, *5*, 71–99.

Bothe, O., Jungclaus, J. H., & Zanchettin, D. (2013). Consistency of the multi-model cmip5/pmip3-past1000 ensemble. *Climate of the Past*, *9*(6), 2471–2487.

Bunde, A., Büntgen, U., Ludescher, J., Luterbacher, J., & von Storch, H. (2013). Is there memory in precipitation? *Nature Climate Change*, *3*(3), 174–175.

Burgman, R., Seager, R., Clement, A., & Herweijer, C. (2010). Role of tropical pacific ssts in global medieval hydroclimate: A modeling study. *Geophysical Research Letters*, *37*(6).

Burke, E. J., & Brown, S. J. (2008). Evaluating uncertainties in the projection of future drought. *Journal of Hydrometeorology*, *9*(2), 292–299.

Cane, M. A., Clement, A. C., Kaplan, A., Kushnir, Y., Pozdnyakov, D., Seager, R., Zebiak, S. E., & Murtugudde, R. (1997). Twentieth-century sea surface temperature trends. *Science*, *275*(5302), 957–960.

Castro, C. L., McKee, T. B., & Pielke Sr, R. A. (2001). The relationship of the north american monsoon to tropical and north pacific sea surface temperatures as revealed by observational analyses. *Journal of Climate*, *14*(24), 4449–4473.

Clement, A. C., Seager, R., Cane, M. A., & Zebiak, S. E. (1996). An ocean dynamical thermostat. *Journal of Climate*, *9*(9), 2190–2196.

Cobb, K. M., Charles, C. D., Cheng, H., & Edwards, R. L. (2003). El nino/southern oscillation and tropical pacific climate during the last millennium. *Nature*, *424*(6946), 271–276.

Cole, J. E., & Cook, E. R. (1998). The changing relationship between enso variability and moisture balance in the continental united states. *Geophysical Research Letters*, *25*(24), 4529–4532.

Compo, G. P., Whitaker, J. S., Sardeshmukh, P. D., Matsui, N., Allan, R. J., Yin, X., Glea-

son, B. E., Vose, R., Rutledge, G., Bessemoulin, P., et al. (2011). The twentieth century reanalysis project. *Quarterly Journal of the Royal Meteorological Society*, *137*(654), 1–28.

Cook, B. I., Ault, T. R., & Smerdon, J. E. (2015). Unprecedented 21st century drought risk in the american southwest and central plains. *Science Advances*, *1*(1), e1400082.

Cook, B. I., & Seager, R. (2013). The response of the north american monsoon to increased greenhouse gas forcing. *Journal of Geophysical Research: Atmospheres*, *118*(4), 1690–1699.

Cook, B. I., Seager, R., Miller, R. L., & Mason, J. A. (2013). Intensification of north american megadroughts through surface and dust aerosol forcing*. *Journal of Climate*, *26*(13), 4414–4430.

Cook, B. I., Smerdon, J. E., Seager, R., & Coats, S. (2014a). Global warming and 21st century drying. *Climate Dynamics*, *43*(9-10), 2607–2627.

Cook, B. I., Smerdon, J. E., Seager, R., & Cook, E. R. (2014b). Pan-continental droughts in north america over the last millennium*. *Journal of Climate*, *27*(1), 383–397.

Cook, E. R. (in review). *Old World Megadroughts and Pluvials During the Common Era*. Science Advances.

Cook, E. R., Anchukaitis, K. J., Buckley, B. M., D'Arrigo, R. D., Jacoby, G. C., & Wright, W. E. (2010a). Asian monsoon failure and megadrought during the last millennium. *Science*, *328*(5977), 486–489.

Cook, E. R., D'Arrigo, R. D., & Anchukaitis, K. J. (2009). *Tree Ring 500 Year ENSO Index Reconstructions*. NOAA/NCDC Paleoclimatology Program.

Cook, E. R., Seager, R., Cane, M. A., & Stahle, D. W. (2007). North american drought: reconstructions, causes, and consequences. *Earth-Science Reviews*, *81*(1), 93–134.

Cook, E. R., Seager, R., Heim, R. R., Vose, R. S., Herweijer, C., & Woodhouse, C. (2010b). Megadroughts in north america: Placing ipcc projections of hydroclimatic change in a long-term palaeoclimate context. *Journal of Quaternary Science*, *25*(1), 48–61.

Cook, E. R., Woodhouse, C. A., Eakin, C. M., Meko, D. M., & Stahle, D. W. (2004). Long-term aridity changes in the western united states. *Science*, *306*(5698), 1015–1018.

Crowley, T. J. (2000). Causes of climate change over the past 1000 years. *Science*, *289*(5477), 270–277.

Dai, A. (2013). Increasing drought under global warming in observations and models. *Nature Climate Change*, *3*(1), 52–58.

Dai, A., Trenberth, K. E., & Karl, T. R. (1998). Global variations in droughts and wet spells: 1900–1995. *Geophysical Research Letters*, *25*(17), 3367–3370.

Dai, A., Trenberth, K. E., & Qian, T. (2004). A global dataset of palmer drought severity index for 1870-2002: Relationship with soil moisture and effects of surface warming. *Journal of Hydrometeorology*, *5*(6), 1117–1130.

D'Arrigo, R., Cook, E. R., Wilson, R. J., Allan, R., & Mann, M. E. (2005). On the variability of enso over the past six centuries. *Geophysical Research Letters*, *32*(3).

Douglass, A. E. (1935). *Dating Pueblo Bonito and other ruins of the Southwest*. 1. National Geographic Society.

Dumenil, L. (1992). A rainfall-runoff scheme for use in the hamburg climate model. *Advances in Theoretical Hydrology, A Tribune to James Dooge*, (pp. 129–157).

Emile-Geay, J., Cobb, K. M., Mann, M. E., & Wittenberg, A. T. (2013). Estimating central equatorial pacific sst variability over the past millennium. part ii: Reconstructions and implications. *Journal of Climate*, *26*(7), 2329–2352.

Enfield, D. B., Mestas-Nuñez, A. M., & Trimble, P. J. (2001). The atlantic multidecadal oscillation and its relation to rainfall and river flows in the continental us. *Geophysical Research Letters*, *28*(10), 2077–2080.

Feng, S., Oglesby, R. J., Rowe, C. M., Loope, D. B., & Hu, Q. (2008). Atlantic and pacific sst influences on medieval drought in north america simulated by the community atmospheric model. *Journal of Geophysical Research: Atmospheres (1984–2012)*, *113*(D11).

Fernández-Donado, L., González-Rouco, J., Raible, C., Ammann, C., Barriopedro, D., García-Bustamante, E., Jungclaus, J. H., Lorenz, S., Luterbacher, J., Phipps, S., et al. (2013). Large-scale temperature response to external forcing in simulations and reconstructions of the last millennium. *Climate of the Past*, *9*, 393–421.

Forman, S. L., Oglesby, R., & Webb, R. S. (2001). Temporal and spatial patterns of holocene dune activity on the great plains of north america: megadroughts and climate links. *Global and Planetary Change*, *29*(1), 1–29.

Foster, J., Liston, G., Koster, R., Essery, R., Behr, H., Dumenil, L., Verseghy, D., Thompson, S., Pollard, D., & Cohen, J. (1996). Snow cover and snow mass intercomparisons of general circulation models and remotely sensed datasets. *Journal of Climate*, *9*(2), 409–426.

Gershunov, A., & Barnett, T. P. (1998). Enso influence on intraseasonal extreme rainfall and temperature frequencies in the contiguous united states: Observations and model results. *Journal of Climate*, *11*(7), 1575–1586.

Giese, B. S., & Ray, S. (2011). El niño variability in simple ocean data assimilation (soda), 1871–2008. *Journal of Geophysical Research: Oceans (1978–2012)*, *116*(C2).

Gochis, D., Schemm, J., Shi, W., Long, L., Higgins, W., & Douglas, A. (2009). A forum for evaluating forecasts of the north american monsoon. *Eos, Transactions American Geophysical Union*, *90*(29), 249–251.

Goddard, L., & Graham, N. E. (1999). Importance of the indian ocean for simulating rainfall anomalies over eastern and southern africa. *Journal of Geophysical Research: Atmospheres (1984–2012)*, *104*(D16), 19099–19116.

González-Rouco, J., Beltrami, H., Zorita, E., & Stevens, M. (2009). Borehole climatology: a discussion based on contributions from climate modeling. *Climate of the Past*, *5*(1), 97–127.

González-Rouco, J., Beltrami, H., Zorita, E., & Von Storch, H. (2006). Simulation and inversion of borehole temperature profiles in surrogate climates: Spatial distribution and surface coupling. *Geophysical Research Letters*, *33*(1).

Gonzalez-Rouco, J., Fernández-Donado, L., Raible, C., Barriopedro, D., Lutherbacher, J., Jungclaus, J., Swingedouw, D., Servonnat, J., Zorita, E., Wagner, S., et al. (2011). Medieval climate anomaly to little ice age transition as simulated by current climate models.

Goosse, H., Crespin, E., Dubinkina, S., Loutre, M.-F., Mann, M. E., Renssen, H., Sallaz-Damaz, Y., & Shindell, D. (2012). The role of forcing and internal dynamics in explaining the "medieval climate anomaly". *Climate dynamics*, *39*(12), 2847–2866.

Graham, N. E., Hughes, M. K., Ammann, C. M., Cobb, K. M., Hoerling, M. P., Kennett, D. J., Kennett, J. P., Rein, B., Stott, L., Wigand, P. E., et al. (2007). Tropical pacific–mid-latitude teleconnections in medieval times. *Climatic Change*, *83*(1-2), 241–285.

Griffin, D., Meko, D. M., Touchan, R., Leavitt, S. W., & Woodhouse, C. A. (2011). Latewood chronology development for summer-moisture reconstruction in the us southwest. *Tree-Ring Research*, *67*(2), 87–101.

Griffin, D., Woodhouse, C. A., Meko, D. M., Stahle, D. W., Faulstich, H. L., Carrillo, C., Touchan, R., Castro, C. L., & Leavitt, S. W. (2013). North american monsoon precipitation reconstructed from tree-ring latewood. *Geophysical Research Letters*, *40*(5), 954–958.

Gupta, A. S., Jourdain, N. C., Brown, J. N., & Monselesan, D. (2013). Climate drift in the cmip5 models*. *Journal of Climate*, *26*(21), 8597–8615.

Gutzler, D. S. (2000). Covariability of spring snowpack and summer rainfall across the southwest united states. *Journal of Climate*, *13*(22), 4018–4027.

Hanson, P., Arbogast, A., Johnson, W., Joeckel, R., & Young, A. (2010). Megadroughts and late holocene dune activation at the eastern margin of the great plains, north-central kansas, usa. *Aeolian Research*, *1*(3), 101–110.

Harnik, N., Seager, R., Naik, N., Cane, M., & Ting, M. (2010). The role of linear wave refraction in the transient eddy–mean flow response to tropical pacific sst anomalies. *Quarterly Journal of the Royal Meteorological Society*, *136*(653), 2132–2146.

Held, I. M., & Soden, B. J. (2006). Robust responses of the hydrological cycle to global warming. *Journal of Climate*, *19*(21), 5686–5699.

Herweijer, C., Seager, R., & Cook, E. R. (2006). North american droughts of the mid to late nineteenth century: a history, simulation and implication for mediaeval drought. *The Holocene*, *16*(2), 159–171.

Herweijer, C., Seager, R., Cook, E. R., & Emile-Geay, J. (2007). North american droughts of the last millennium from a gridded network of tree-ring data. *Journal of Climate*, *20*(7), 1353–1376.

Higgins, R., & Shi, W. (2000). Dominant factors responsible for interannual variability of the summer monsoon in the southwestern united states. *Journal of Climate*, *13*(4), 759–776.

Hoerling, M., Eischeid, J., Kumar, A., Leung, R., Mariotti, A., Mo, K., Schubert, S., & Seager, R. (2014). Causes and predictability of the 2012 great plains drought. *Bulletin of the American Meteorological Society*, *95*(2), 269–282.

Hoerling, M., & Kumar, A. (2003). The perfect ocean for drought. *Science*, *299*(5607), 691–694.

Hoerling, M. P., & Ting, M. (1994). Organization of extratropical transients during el nino. *Journal of climate*, *7*(5), 745–766.

Hu, Q., & Feng, S. (2001). Variations of teleconnection of enso and interannual variation in summer rainfall in the central united states. *Journal of climate*, *14*(11), 2469–2480.

Hunt, B. G. (2011). Global characteristics of pluvial and dry multi-year episodes, with emphasis on megadroughts. *International Journal of Climatology*, *31*(10), 1425–1439.

Jansen, E., et al. (2007). Paleoclimate. climate change 2007: The physical science basis. contributionof working group i to the fourth assessment report of the intergovernmental panel on climate change, eds s solomon et al.

Joseph, R., & Nigam, S. (2006). Enso evolution and teleconnections in ipcc's twentieth-century climate simulations: Realistic representation? *Journal of Climate*, *19*(17), 4360–4377.

Kalnay, E., Kanamitsu, M., Kistler, R., Collins, W., Deaven, D., Gandin, L., Iredell, M., Saha, S., White, G., Woollen, J., et al. (1996). The ncep/ncar 40-year reanalysis project. *Bulletin of the American meteorological Society*, *77*(3), 437–471.

Kam, J., Sheffield, J., & Wood, E. F. (2014). Changes in drought risk over the contiguous united states (1901–2012): The influence of the pacific and atlantic oceans. *Geophysical Research Letters*, *41*(16), 5897–5903.

Kaplan, A., Cane, M. A., Kushnir, Y., Clement, A. C., Blumenthal, M. B., & Rajagopalan, B. (1998). Analyses of global sea surface temperature 1856–1991. *Journal of Geophysical Research: Oceans (1978–2012)*, *103*(C9), 18567–18589.

Karnauskas, K. B., Seager, R., Kaplan, A., Kushnir, Y., & Cane, M. A. (2009). Observed strengthening of the zonal sea surface temperature gradient across the equatorial pacific ocean*. *Journal of Climate*, *22*(16), 4316–4321.

Karnauskas, K. B., Smerdon, J. E., Seager, R., & González-Rouco, J. F. (2012). A pacific centennial oscillation predicted by coupled gcms*. *Journal of Climate*, *25*(17), 5943–5961.

Knutti, R., Furrer, R., Tebaldi, C., Cermak, J., & Meehl, G. A. (2010). Challenges in combining projections from multiple climate models. *Journal of Climate*, *23*(10), 2739–2758.

Kushnir, Y., Seager, R., Ting, M., Naik, N., & Nakamura, J. (2010). Mechanisms of tropical atlantic sst influence on north american precipitation variability*. *Journal of Climate*, *23*(21), 5610–5628.

Langenbrunner, B., & Neelin, J. D. (2013). Analyzing enso teleconnections in cmip models as a measure of model fidelity in simulating precipitation. *Journal of Climate*, *26*(13), 4431–4446.

Langford, S., Stevenson, S., & Noone, D. (2014). Analysis of low-frequency precipitation variability in cmip5 historical simulations for southwestern north america. *Journal of Climate*, *27*(7), 2735–2756.

Legutke, S., Voss, R., Klimarechenzentrum, D., & Betreuungsgruppe, M. (1999). *The Hamburg atmosphere-ocean coupled circulation model ECHO-G*, vol. 18. DKRZ.

Li, J., Xie, S.-P., Cook, E. R., Morales, M. S., Christie, D. A., Johnson, N. C., Chen, F., D'Arrigo, R., Fowler, A. M., Gou, X., et al. (2013). El niño modulations over the past seven centuries. *Nature Climate Change*, *3*(9), 822–826.

MacDonald, G. M., & Case, R. A. (2005). Variations in the pacific decadal oscillation over the past millennium. *Geophysical Research Letters*, *32*(8).

Maloney, E. D., Camargo, S. J., Chang, E., Colle, B., Fu, R., Geil, K. L., Hu, Q., Jiang, X., Johnson, N., Karnauskas, K. B., et al. (2014). North american climate in cmip5 experiments: Part iii: Assessment of twenty-first-century projections*. *Journal of Climate*, *27*(6), 2230–2270.

Mann, M. E., & Lees, J. M. (1996). Robust estimation of background noise and signal detection in climatic time series. *Climatic change*, *33*(3), 409–445.

Mann, M. E., Zhang, Z., Rutherford, S., Bradley, R. S., Hughes, M. K., Shindell, D., Ammann, C., Faluvegi, G., & Ni, F. (2009). Global signatures and dynamical origins of the little ice age and medieval climate anomaly. *Science*, *326*(5957), 1256–1260.

Mantua, N. J., & Hare, S. R. (2002). The pacific decadal oscillation. *Journal of Oceanography*, *58*(1), 35–44.

Mantua, N. J., Hare, S. R., Zhang, Y., Wallace, J. M., & Francis, R. C. (1997). A pacific interdecadal climate oscillation with impacts on salmon production. *Bulletin of the american Meteorological Society*, *78*(6), 1069–1079.

McCabe, G. J., Betancourt, J. L., Gray, S. T., Palecki, M. A., & Hidalgo, H. G. (2008). Associations of multi-decadal sea-surface temperature variability with us drought. *Quaternary International*, *188*(1), 31–40.

McCabe, G. J., Palecki, M. A., & Betancourt, J. L. (2004). Pacific and atlantic ocean influences on multidecadal drought frequency in the united states. *Proceedings of the National Academy of Sciences*, *101*(12), 4136–4141.

McCarthy, G. D., Haigh, I. D., Hirschi, J. J.-M., Grist, J. P., & Smeed, D. A. (2015). Ocean impact on decadal atlantic climate variability revealed by sea-level observations. *Nature*, *521*(7553), 508–510.

McKee, T. B., Doesken, N. J., Kleist, J., et al. (1993). The relationship of drought frequency

and duration to time scales. In *Proceedings of the 8th Conference on Applied Climatology*, vol. 17, (pp. 179–183). American Meteorological Society Boston, MA.

Meehl, G. A., & Hu, A. (2006). Megadroughts in the indian monsoon region and southwest north america and a mechanism for associated multidecadal pacific sea surface temperature anomalies. *Journal of Climate*, *19*(9), 1605–1623.

Milly, P., Betancourt, J., Falkenmark, M., Hirsch, R., Kundzewicz, Z., & Lettenmair, D. (2008). Stouffer. rj 2008. stationarity is dead: wither water management. *Science*, *319*, 73–574.

Milly, P., & Dunne, K. A. (2011). On the hydrologic adjustment of climate-model projections: The potential pitfall of potential evapotranspiration. *Earth Interactions*, *15*(1), 1–14.

Min, S.-K., Legutke, S., Hense, A., & Kwon, W.-T. (2005a). Internal variability in a 1000-yr control simulation with the coupled climate model echo-g–i. near-surface temperature, precipitation and mean sea level pressure. *Tellus A*, *57*(4), 605–621.

Min, S.-K., Legutke, S., Hense, A., & Kwon, W.-T. (2005b). Internal variability in a 1000-yr control simulation with the coupled climate model echo-g–ii. el niño southern oscillation and north atlantic oscillation. *Tellus A*, *57*(4), 622–640.

Nigam, S., Guan, B., & Ruiz-Barradas, A. (2011). Key role of the atlantic multidecadal oscillation in 20th century drought and wet periods over the great plains. *Geophysical Research Letters*, *38*(16).

Notaro, M., & Zarrin, A. (2011). Sensitivity of the north american monsoon to antecedent rocky mountain snowpack. *Geophysical Research Letters*, *38*(17).

Ogata, T., Xie, S.-P., Wittenberg, A., & Sun, D.-Z. (2013). Interdecadal amplitude modulation of el niño–southern oscillation and its impact on tropical pacific decadal variability*. *Journal of Climate*, *26*(18), 7280–7297.

Oglesby, R., Feng, S., Hu, Q., & Rowe, C. (2012). The role of the atlantic multidecadal oscillation on medieval drought in north america: Synthesizing results from proxy data and climate models. *Global and Planetary Change*, *84*, 56–65.

Pahl-Wostl, C., Sendzimir, J., Jeffrey, P., Aerts, J., Berkamp, G., & Cross, K. (2007). Managing change toward adaptive water management through social learning. *Ecology and Society*, *12*(2), 30.

Palmer, T. (1993). Extended-range atmospheric prediction and the lorenz model. *Bulletin of the American Meteorological Society*, *74*(1), 49–65.

Palmer, W. C. (1965). *Meteorological drought*, vol. 30. US Department of Commerce, Weather Bureau Washington, DC, USA.

Polade, S. D., Gershunov, A., Cayan, D. R., Dettinger, M. D., & Pierce, D. W. (2013). Natural climate variability and teleconnections to precipitation over the pacific-north american region in cmip3 and cmip5 models. *Geophysical Research Letters*, *40*(10), 2296–2301.

Rajagopalan, B., Cook, E., Lall, U., & Ray, B. K. (2000). Spatiotemporal variability of enso and sst teleconnections to summer drought over the united states during the twentieth century. *Journal of Climate*, *13*(24), 4244–4255.

Rasmusson, E. M., & Carpenter, T. H. (1982). Variations in tropical sea surface temperature and surface wind fields associated with the southern oscillation/el niño. *Monthly Weather Review*, *110*(5), 354–384.

Santer, B. D., Taylor, K. E., Wigley, T. M., Penner, J. E., Jones, P. D., & Cubasch, U. (1995). Towards the detection and attribution of an anthropogenic effect on climate. *Climate Dynamics*, *12*(2), 77–100.

Sarachick, E. S., & Cane, M. A. (2010). *The El Niño-Southern Oscillation Phenomenon*. Cambridge University Press Cambridge, UK, and New York.

Schlesinger, M. E., & Ramankutty, N. (1994). An oscillation in the global climate system of period 65-70 years. *Nature*, (367), 723–726.

Schmidt, G., Annan, J. D., Bartlein, P., Cook, B., Guilyardi, E., Hargreaves, J., Harrison, S., Kageyama, M., LeGrande, A., Konecky, B., et al. (2013). Using paleo-climate comparisons to constrain future projections in cmip5. *Climate of the Past*, *9*(775–835).

Schmidt, G. A., Jungclaus, J., Ammann, C., Bard, E., Braconnot, P., Crowley, T., Delaygue, G., Joos, F., Krivova, N., Muscheler, R., et al. (2011). Climate forcing reconstructions for use in pmip simulations of the last millennium (v1. 0). *Geoscientific Model Development*, *4*(1), pp33–45.

Schreiber, T., & Schmitz, A. (2000). Surrogate time series. *Physica D: Nonlinear Phenomena*, *142*(3), 346–382.

Schubert, S., Gutzler, D., Wang, H., Dai, A., Delworth, T., Deser, C., Findell, K., Fu, R., Higgins, W., Hoerling, M., et al. (2009). A us clivar project to assess and compare the responses of global climate models to drought-related sst forcing patterns: overview and results. *Journal of Climate*, *22*(19), 5251–5272.

Schubert, S. D., Suarez, M. J., Pegion, P. J., Koster, R. D., & Bacmeister, J. T. (2004a). Causes of long-term drought in the us great plains. *Journal of Climate*, *17*(3), 485–503.

Schubert, S. D., Suarez, M. J., Pegion, P. J., Koster, R. D., & Bacmeister, J. T. (2004b). On the cause of the 1930s dust bowl. *Science*, *303*(5665), 1855–1859.

Seager, R., Burgman, R., Kushnir, Y., Clement, A., Cook, E., Naik, N., & Miller, J. (2008a). Tropical pacific forcing of north american medieval megadroughts: Testing the concept with an atmosphere model forced by coral-reconstructed ssts*. *Journal of Climate*, *21*(23), 6175–6190.

Seager, R., Goddard, L., Nakamura, J., Henderson, N., & Lee, D. E. (2014a). Dynamical

causes of the 2010/11 texas–northern mexico drought*. *Journal of Hydrometeorology*, *15*(1), 39–68.

Seager, R., Graham, N., Herweijer, C., Gordon, A. L., Kushnir, Y., & Cook, E. (2007). Blueprints for medieval hydroclimate. *Quaternary Science Reviews*, *26*(19), 2322–2336.

Seager, R., Harnik, N., Kushnir, Y., Robinson, W., & Miller, J. (2003). Mechanisms of hemispherically symmetric climate variability*. *Journal of Climate*, *16*(18), 2960–2978.

Seager, R., Harnik, N., Robinson, W., Kushnir, Y., Ting, M., Huang, H.-P., & Velez, J. (2005a). Mechanisms of enso-forcing of hemispherically symmetric precipitation variability. *Quarterly Journal of the Royal Meteorological Society*, *131*(608), 1501–1527.

Seager, R., Kushnir, Y., Herweijer, C., Naik, N., & Velez, J. (2005b). Modeling of tropical forcing of persistent droughts and pluvials over western north america: 1856-2000*. *Journal of Climate*, *18*(19), 4065–4088.

Seager, R., Kushnir, Y., Ting, M., Cane, M., Naik, N., & Miller, J. (2008b). Would advance knowledge of 1930s ssts have allowed prediction of the dust bowl drought?*. *Journal of Climate*, *21*(13), 3261–3281.

Seager, R., Kushnir, Y., Ting, M., Naik, N., & Nakamura, J. (2015). Decadal hydroclimate variability across the americas. *Climate Change, Multidecadal and Beyond*.

Seager, R., Naik, N., Ting, M., Cane, M., Harnik, N., & Kushnir, Y. (2010). Adjustment of the atmospheric circulation to tropical pacific sst anomalies: Variability of transient eddy propagation in the pacific–north america sector. *Quarterly Journal of the Royal Meteorological Society*, *136*(647), 277–296.

Seager, R., Neelin, D., Simpson, I., Liu, H., Henderson, N., Shaw, T., Kushnir, Y., Ting, M., & Cook, B. (2014b). Dynamical and thermodynamical causes of large-scale changes in the hydrological cycle over north america in response to global warming*. *Journal of Climate*, *27*(20), 7921–7948.

Seager, R., Ting, M., Davis, M., Cane, M., Naik, N., Nakamura, J., Li, C., Cook, E., & Stahle, D. W. (2009). Mexican drought: an observational modeling and tree ring study of variability and climate change. *Atmósfera*, *22*(1), 1–31.

Seager, R., Ting, M., Li, C., Naik, N., Cook, B., Nakamura, J., & Liu, H. (2013). Projections of declining surface-water availability for the southwestern united states. *Nature Climate Change*, *3*(5), 482–486.

Seager, R., & Vecchi, G. A. (2010). Greenhouse warming and the 21st century hydroclimate of southwestern north america. *Proceedings of the National Academy of Sciences*, *107*(50), 21277–21282.

Sheffield, J., Barrett, A. P., Colle, B., Nelun Fernando, D., Fu, R., Geil, K. L., Hu, Q., Kinter, J., Kumar, S., Langenbrunner, B., et al. (2013a). North american climate in cmip5 experiments. part i: Evaluation of historical simulations of continental and regional climatology*. *Journal of Climate*, *26*(23), 9209–9245.

Sheffield, J., Camargo, S. J., Fu, R., Hu, Q., Jiang, X., Johnson, N., Karnauskas, K. B., Kim, S. T., Kinter, J., Kumar, S., et al. (2013b). North american climate in cmip5 experiments. part ii: Evaluation of historical simulations of intraseasonal to decadal variability. *Journal of Climate*, *26*(23), 9247–9290.

Sheffield, J., Wood, E. F., & Roderick, M. L. (2012). Little change in global drought over the past 60 years. *Nature*, *491*(7424), 435–438.

Smerdon, J. E. (2012). Climate models as a test bed for climate reconstruction methods: pseudoproxy experiments. *Wiley Interdisciplinary Reviews: Climate Change*, *3*(1), 63–77.

Smerdon, J. E., Coats, S., & Ault, T. R. (2015a). Model-dependent spatial skill in pseudoproxy experiments testing climate field reconstruction methods for the common era. *Climate Dynamics*.

Smerdon, J. E., Cook, B. I., Cook, E. R., & Seager, R. (2015b). Bridging past and future climate across paleoclimatic reconstructions, observations, and models: A hydroclimate case study. *Journal of Climate*.

Smerdon, J. E., Kaplan, A., Zorita, E., González-Rouco, J. F., & Evans, M. (2011). Spatial performance of four climate field reconstruction methods targeting the common era. *Geophysical Research Letters*, *38*(11).

Smith, D. M., Scaife, A. A., & Kirtman, B. P. (2012). What is the current state of scientific knowledge with regard to seasonal and decadal forecasting? *Environmental Research Letters*, *7*(1), 15602–15612.

Smith, I., & Chandler, E. (2010). Refining rainfall projections for the murray darling basin of south-east australia—the effect of sampling model results based on performance. *Climatic Change*, *102*(3-4), 377–393.

Smith, T. M., & Reynolds, R. W. (2003). Extended reconstruction of global sea surface temperatures based on coads data (1854-1997). *Journal of Climate*, *16*(10), 1495–1510.

St. George, S., Meko, D. M., & Cook, E. R. (2010). The seasonality of precipitation signals embedded within the north american drought atlas. *The Holocene*.

Stahle, D., Cleaveland, M., Grissino-Mayer, H., Griffin, R., Fye, F., Therrell, M., Burnette, D., Meko, D., & Villanueva Diaz, J. (2009). Cool-and warm-season precipitation reconstructions over western new mexico. *Journal of Climate*, *22*(13), 3729–3750.

Stahle, D. W., Fye, F. K., Cook, E. R., & Griffin, R. D. (2007). Tree-ring reconstructed megadroughts over north america since ad 1300. *Climatic Change*, *83*(1-2), 133–149.

Stevens, M. B., Smerdon, J. E., González-Rouco, J. F., Stieglitz, M., & Beltrami, H. (2007). Effects of bottom boundary placement on subsurface heat storage: Implications for climate model simulations. *Geophysical research letters*, *34*(2).

Stevenson, S., Fox-Kemper, B., Jochum, M., Neale, R., Deser, C., & Meehl, G. (2012). Will there be a significant change to el niño in the twenty-first century? *Journal of Climate*, *25*(6), 2129–2145.

Stine, S. (1994). Extreme and persistent drought in california and patagonia during mediaeval time. *Nature*, *369*(6481), 546–549.

Stocker, T., Qin, D., Plattner, G.-K., Tignor, M., Allen, S. K., Boschung, J., Nauels, A., Xia, Y., Bex, V., & Midgley, P. M. (2014). *Climate change 2013: The physical science basis*. Cambridge University Press Cambridge, UK, and New York.

Sueyoshi, T., Ohgaito, R., Yamamoto, A., Chikamoto, M., Hajima, T., Okajima, H., Yoshimori, M., Abe, M., O'ishi, R., Saito, F., et al. (2013). Set-up of the pmip3 paleoclimate experiments conducted using an earth system model, miroc-esm. *Geoscientific Model Development*, *6*(3), 819–836.

Sun, S., & Wang, G. (2014). Climate variability attributable to terrestrial and oceanic forcing in the ncar cam3-clm3 models. *Climate dynamics*, *42*(7-8), 2067–2078.

Sutton, R. T., & Hodson, D. L. (2005). Atlantic ocean forcing of north american and european summer climate. *Science*, *309*(5731), 115–118.

Tanaka, S. K., Zhu, T., Lund, J. R., Howitt, R. E., Jenkins, M. W., Pulido, M. A., Tauber, M., Ritzema, R. S., & Ferreira, I. C. (2006). Climate warming and water management adaptation for california. *Climatic Change*, *76*(3-4), 361–387.

Taylor, K. E., Stouffer, R. J., & Meehl, G. A. (2012). An overview of cmip5 and the experiment design. *Bulletin of the American Meteorological Society*, *93*(4), 485–498.

Thompson, D. W., & Wallace, J. M. (1998). The arctic oscillation signature in the wintertime geopotential height and temperature fields. *Geophysical Research Letters*, *25*(9), 1297–1300.

Thornthwaite, C. W. (1948). An approach toward a rational classification of climate. *Geographical review*, (pp. 55–94).

Tierney, J. E., Abram, N. J., Anchukaitis, K. J., Evans, M. N., Giry, C., Kilbourne, K. H., Saenger, C. P., Wu, H. C., & Zinke, J. (2015). Tropical sea surface temperatures for the past four centuries reconstructed from coral archives. *Paleoceanography*, *30*(3), 226–252.

Ting, M., Kushnir, Y., Seager, R., & Li, C. (2009). Forced and internal twentieth-century sst trends in the north atlantic*. *Journal of Climate*, *22*(6), 1469–1481.

Ting, M., Kushnir, Y., Seager, R., & Li, C. (2011). Robust features of atlantic multi-decadal variability and its climate impacts. *Geophysical Research Letters*, *38*(17).

Trenberth, K. E., Branstator, G. W., Karoly, D., Kumar, A., Lau, N.-C., & Ropelewski, C. (1998). Progress during toga in understanding and modeling global teleconnections associated with tropical sea surface temperatures. *Journal of Geophysical Research: Oceans (1978–2012)*, *103*(C7), 14291–14324.

van der Schrier, G., Jones, P., & Briffa, K. (2011). The sensitivity of the pdsi to the thornthwaite and penman-monteith parameterizations for potential evapotranspiration. *Journal of Geophysical Research: Atmospheres (1984–2012)*, *116*(D3).

Vance, T., Roberts, J., Plummer, C., Kiem, A., & van Ommen, T. (2015). Interdecadal pacific variability and eastern australian megadroughts over the last millennium. *Geophysical Research Letters*, *42*(1), 129–137.

Vecchi, G. A., Clement, A., & Soden, B. J. (2008). Examining the tropical pacific's response to global warming. *Eos, Transactions American Geophysical Union*, *89*(9), 81–83.

Vecchi, G. A., Soden, B. J., Wittenberg, A. T., Held, I. M., Leetmaa, A., & Harrison, M. J. (2006). Weakening of tropical pacific atmospheric circulation due to anthropogenic forcing. *Nature*, *441*(7089), 73–76.

Vicente-Serrano, S. M., Beguería, S., López-Moreno, J. I., Angulo, M., & El Kenawy, A. (2010). A new global 0.5 gridded dataset (1901-2006) of a multiscalar drought index: comparison with current drought index datasets based on the palmer drought severity index. *Journal of Hydrometeorology*, *11*(4), 1033–1043.

Von Storch, H., Zorita, E., Jones, J. M., Dimitriev, Y., González-Rouco, F., & Tett, S. F. (2004). Reconstructing past climate from noisy data. *Science*, *306*(5696), 679–682.

Weigel, A. P., Knutti, R., Liniger, M. A., & Appenzeller, C. (2010). Risks of model weighting in multimodel climate projections. *Journal of Climate*, *23*(15), 4175–4191.

Wild, M., Folini, D., Schär, C., Loeb, N., Dutton, E. G., & König-Langlo, G. (2013). The global energy balance from a surface perspective. *Climate dynamics*, *40*(11-12), 3107–3134.

Wittenberg, A. T. (2009). Are historical records sufficient to constrain enso simulations? *Geophysical Research Letters*, *36*(12).

Wohl, E., Barros, A., Brunsell, N., Chappell, N. A., Coe, M., Giambelluca, T., Goldsmith, S., Harmon, R., Hendrickx, J. M., Juvik, J., et al. (2012). The hydrology of the humid tropics. *Nature Climate Change*, *2*(9), 655–662.

Zhang, Y., Wallace, J. M., & Battisti, D. S. (1997). Enso-like interdecadal variability: 1900-93. *Journal of climate*, *10*(5), 1004–1020.

Zhu, C., Lettenmaier, D. P., & Cavazos, T. (2005). Role of antecedent land surface conditions on north american monsoon rainfall variability*. *Journal of Climate*, *18*(16), 3104–3121.

Zhu, J., Huang, B., Marx, L., Kinter, J. L., Balmaseda, M. A., Zhang, R.-H., & Hu, Z.-Z. (2012). Ensemble enso hindcasts initialized from multiple ocean analyses. *Geophysical Research Letters*, *39*(9).

Zorita, E., González-Rouco, F., & Legutke, S. (2003). Testing the mannetal.(1998) approach to paleoclimate reconstructions in the context of a 1000-yr control simulation with the echo-g coupled climate model. *Journal of Climate*, *16*(9), 1378–1390.

Zorita, E., González-Rouco, J., Von Storch, H., Montávez, J., & Valero, F. (2005). Natural and anthropogenic modes of surface temperature variations in the last thousand years. *Geophysical Research Letters*, *32*(8).